SYNTHESIS, CHARACTERIZATION AND OPTICAL APPLICATIONS OF NANOMATERIALS

by

FEN XU

A dissertation submitted to the Graduate Faculty
in Chemistry in partial fulfillment of the requirements
for the degree of Doctor of Philosophy,

The City University of New York

2010

This manuscript has been read and accepted for the Graduate
Faculty in Chemistry in satisfaction of the dissertation
requirements for the degree of Doctor of Philosophy.

10/31/2008	Hiroshi Matsui
Date	Chair of Examining Committee
09/03/2010	Makesh Lakshman
Date	Executive Officer

Professor Lynn Francesconi

Professor Zhonghua Yu

Suppervisory Committee

THE CITY UNIVERSITY OF NEW YORK

ABSTRACT

SYNTHESIS, CHARACTERIZATION AND OPTICAL APPLICATIONS OF NANOMATERIALS

By

Fen Xu

Adviser: Professor Hiroshi Matsui

Nanomaterials have been studied extensively due to their potential application in electronics, photonics and nanodevices. There are a wide variety of methods developed to create the nano-scale materials. Chemical colloidal synthesis is the way most used since it is reproducible and high efficiency.

Nanoparticles lie at the heart of nanoscience for their novel electronic, magnetic and optical properties. In this dissertation, there are two parts where researches have been performed based on the synthesis of metal and semiconductor nanoparticles.

In part I, Semiconductor type-II core-shell quantum dots (QDs) ZnO-CdS have been synthesized by chemical colloidal method which was carried out in a two-step process. We initially synthesized ZnO core nanoparticles and overcoat them with CdS shell. UV-Visible spectra, photoluminescence spectra (PL), high resolution TEM images and X-ray microanalysis for composition studies of the core-shell nanoparticles were characterized. PL lifetime measurements showed this type-II ZnO-CdS core-shell QDs presented extended exciton lifetime due to the spatial separation of electrons and holes between the core and the shell, which opens various useful applications in biosensors and photovoltaic devices.

In part II, normal Raman (NR) and surface enhanced Raman scattering (SERS) spectra of 3-hydroxyflavone (3-HF) have been measured. The SERS spectra were obtained both on a Ag electrode surface and on Ag colloidal nanoparticles. The experimental results support the DFT geometry calculations, which show that an adatom site at the vertex of Ag20 cluster binding with the 3-HF molecular plane tilted at an angle of about 53° to the surface is a low-energy structure. This is consistent with the enhancement of in-plane vibrational modes. Furthermore, the effect of fluence level on the discoloration of marble surfaces after the removal of the encrustation by 355 nm laser pulses was comparatively studied. Considering the thermochemical reaction possibly occurring in the encrustation during laser irradiation, the mechanism responsible for the discoloration of the cleaned marble surface was analyzed. The reduction of iron oxides by graphite plays a key role in determining the final color of the cleaned marble surface. The marble surfaces before and after laser irradiation were characterized in terms of the chemical components through surface enhanced Raman spectroscopy on Ag colloidal nanoparticles. To analyze the working mechanism of the liquid layer covering the marble encrustation, distilled water, ethanol and acetone were used in marble cleaning to compare the cleaning efficiency at different fluence levels. Surface-enhanced Raman spectroscopy (SERS) on silver colloidal nanoparticles was also used to identify the chemical constituents of the cleaned marble with these three different liquids.

ACKNOWLEDGMENTS

This work could not have been successfully completed without generous assistance from many sources, including several people and funding sources.

The research in Chapter 1 was performed under my current adviser, Professor Hiroshi Matsui, and outcomes in Chapters 2 - 4 were done at the laboratory of Professor John Lombardi, my former adviser.

I would like to thank adviser Professor Hiroshi Matsui for his guidance and support. His suggestion and encouragement help me to overcome many difficulties. I learn how to be a scientist and educator from him.

I would like to thank Professor John Lombardi, who kindly agreed to put my results obtained in his lab in my Ph.D. thesis. Also I would like to thank him for teaching me knowledge and give me chance to grow along scientific path.

I also own thanks to my research committees Professor Lynn Francesconi and Professor Zhonghua Yu for taking time to serve on my Ph.D. committee. Their advice and guidance help me to succeed in this project.

I would especially like to acknowledge the assistance from the members of the Professor Klaus Grohmann’s group and Professor C. M. Drain’s group. Also I own thanks to Professor Glen Kowach from City College for his kind help and useful advice and his student Chunmin Feng for his assistance. Thanks Professor Igor Kuskovsky from Queens College for his guidance and useful discussion (Figure1.6 in chapter 1 was measured in his lab). I would like to thank Jorge Morale from City College and

Vyacheslav Volkov from Brookhaven National Lab for assisting TEM images (Figure 1.2 (c) and Figure 1.3 in chapter 1 were measured in his lab).

I would like to acknowledge previous postdoctoral Dr. Xueyun Gao, Dr. Anita Swami and Dr. Linglu Yang for their help. Also thanks all the colleagues in Matsui group for their assistances including Mr. Nurxat Nueraji, Mr. Hanying Bai, Mr. Christophe Pejoux, Mr. Wei Su, Ms. Anjia Luona, Ms. Prerna Kaur, Dr. Roberto de la Rice, and Ms. Kristina Fabijanic.

I also acknowledge the financial supports from DOE and NSF.

Finally, I want to express my deepest thanks and love to my husband, my parents, my sisters and my brother for their endless support and encouragement.

This dissertation is dedicated to
my husband Samer and my son William.

TABLE OF CONTENTS

LIST OF FIGURES

Chapter 1 figures

Chapter 2 figures

Chapter 3 figures

Chapter 4 figures

LIST OF EQUATIONS

LIST OF TABLES

Chapter 1

Long Electron-Hole Separation of ZnO-CdS Core-Shell Quantum Dots

1.1 Introduction

The tunability of electronic and optical properties of semiconductor nanocrystal quantum dots (QDs) has been an important subjects in nanotechnology because of their promising applications in solar cells,[1] light emitters,[2] biotags,[3] and biosensing.[4] To further control these properties precisely, heterostructured or core-shell QDs have been developed. For example, coatings on CdSe QDs with CdS [5] or ZnS [6] shells resulted in greatly enhanced fluorescence quantum yield and photochemical stability due to the electron and hole confinement to the core. While the control of the emission property of QDs in wavelength has been studied extensively, the control of emission lifetime of QDs has not been explored in depth. While the emission lifetime controls is difficult for most core-shell QDs, one can slow the recombination between the two carriers if the band structure between the core and the shell materials is staggered and one photogenerated carrier is predominantly confined to the core and the other is located in the shell (**Figure 1. 1**). In this so-called type-II QD system, the longer exciton lifetime arises from the decreased wave function overlaps between holes and electrons, and the emission lifetime becomes extremely sensitive to the thickness of the shell. Here we demonstrated that indeed the increase of the shell thickness of a ZnO-CdS core-shell QD could increase its exciton lifetime. The longer excitonic lifetime of type-II QDs could be beneficial in fluorescence-based sensors, medical imaging, solar cells photovoltaics, and lasers.[7, 8] Furthermore, the type-II heterostructure QDs suppress the Auger recombination,[9-11] which is highly desirable for nanoparticle-based optoelectronic devices.[12, 13]

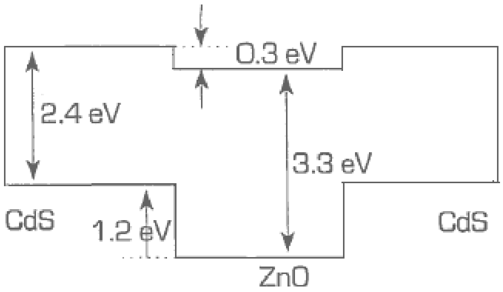

Figure 1.1 Band diagram of the ZnO-CdS interface.[22]

In addition, the number of reports for type-II core-shell QD systems with visible absorption and emission is relatively small, [14-19] and it is very usful to increase the lineups of core-shell type-II QDs, which will enable one to choose desired physical properties such as absorption, emission, and excitonic lifetime in a wide range, so that the type-II QDs could be applied more broadly to improve energy storage, photovoltaic devices, and catalysis. To meet this thirst for QD development, we explored the type-II QDs with ZnO cores for visible absorption. The exciton lifetime of the core-shell ZnO-CdS QDs was at least 100 times greater than the typical type-I QDs, and the exciton lifetime further increased as the coating thickness of the CdS shell on a ZnO core increased.

1.2 Experimental Section

Synthesis of ZnO-CdS Core-Shell QDs. Trioctylphosphine oxide (TOPO, 90% pure), trioctylphosphine (TOP, 95% pure), and hexadecylamine (HDA, 99% pure) were obtained from Sigma Aldrich and Fluka, respectively. Dimethylcadmium ($CdMe_2$) and diethylzinc ($ZnEt_2$) were purchased from Strem and Fluka, respectively, and both chemicals were filtered separately through a 0.2 µm filter in a glovebox. Hexamethyldisilathiane ($(TMS)_2S$) was used as purchased from Fluka. Anhydrous hexane and methanol were purchased from Sigma Aldrich. The ZnO core nanoparticles (NP) from $Zn(Et)_2$ were synthesized according to the method previously reported by Guyot-Sionnest and co-workers.[20] The zinc precursor solution was prepared in a glovebox by dissolving 150 µL Zn $(Et)_2$ in 4 mL decane and then injected into 4 mL of octylamine degassed by bubbling with O_2 for about 1 hour. This mixture was bubbled with O_2 for another 5 minutes and injected into 6 g TOPO at 200 ºC under N_2 flow and left for 12 hours. The reaction mixture was allowed to cool to 160~180 ºC for the growth of the ZnO NPs. To grow larger size particles, larger amounts of Zn-O precursors can be added. Adjusting the growth time, controlled by the termination of the reaction upon cooling, was also employed to change the size of ZnO NPs. Then, ZnO NPs were precipitated from the growth solution by adding methanol, and the precipitated ZnO NPs (~100 mg) were dispersed in TOPO (7.5 g) and HDA (4 g) at 100 ºC. For the CdS growth around the ZnO core, 150 µL $(TMS)_2$ S and 35 µL Cd $(Me)_2$ were dissolved in 4 mL of TOP in a glove-box, and then this mixture was drop-wisely added into the reaction flask containing the ZnO core nanoparticles at 140 ºC. This drop-wise injection of precursors is very important to slow down the ion-exchange reaction between Zn-O ions and Cd-S ions through the surface of ZnO core NPs because the CdS exchange process is so fast that the ZnO core cannot survive without slowing the shell growth reaction. It should also be noted that due to this relatively fast CdS reaction the concentration of ZnO NPs was very sensitive to influencing the yield of the resulting ZnO-CdS core-shell QDs. Then, the resulting core-shell QDs were annealed at 110 ºC for 24 and 48 hours, while the annealing time between 24 and 48 hours did not make a significant difference in the emission properties of the resulting crystals. Obtained QDs were precipitated by adding methanol and dispersed in hexane for further optical measurements. This two-step coating approach was effective to avoid the formation of alloyed nanoparticles at 200-240 ºC.[21] The use of these organometallic precursors also assisted robust nucleations of the core and shell to decompose them at relatively low temperature.

Analysis of QDs. HRTEM images and SAED patterns were recorded with a JEOL3000F microscope operating at 300 keV, equipped with a field emission gun and installed at Brookhaven National Laboratory. Point resolution of JEOL3000F microscope is ~1.55 Å. Nanoarea EDX analysis was performed using a Thermo Noran EDX system attached to the JEOL3000F microscope. X-ray microanalysis for composition studies at nanoscale was carried out with a Si (Li) detector using a Vantage 2.4 digital pulse processor and Vista 2.3 microanalysis software. Optical absorption (OA) spectra were recorded by a Cary 50 Probe UV-Vis spectrophotometer in the wavelength range of 300 to 600 nm, and photoluminescence (PL) emission spectra were recorded by a Jobin Yvon-Spex Fluorolog spectrophotometer**.** Time-resolved PL studies were performed with a Jobin Yvon FluoroMax-3, using a time correlated single-photon counting system with a 310 nm nano-LED as an excitation source. This system allows time resolution of < 1 ns. All measurements were performed at room temperature.

1.3 Results and Discussion

To grow core-shell ZnO-CdS QDs, CdS shells were grown on the ZnO nanoparticles (NPs) by applying the step-wise reaction processes between $(TMS)_2S$ and $CdMe_2$. CdS shell growth on the ZnO core could be accomplished by the slow ion-exchange reaction between ZnO and CdS on the surface of ZnO NPs. Further stabilization of the CdS shell growth was accomplished by exchanging $(TMS)_2S$ with more stable capping agents, Hexadecylamine, TOPO and TOP. The thickness of the CdS shell was controlled by the amount of precursors and subsequent annealing process. The band alignment between the core of ZnO and the shell of CdS is summarized in **Figure 1.1**.[22] When the photogenerated electrons are confined within the ZnO core and holes are located in the CdS shell, their recombination will be significantly slowed by this band alignment.

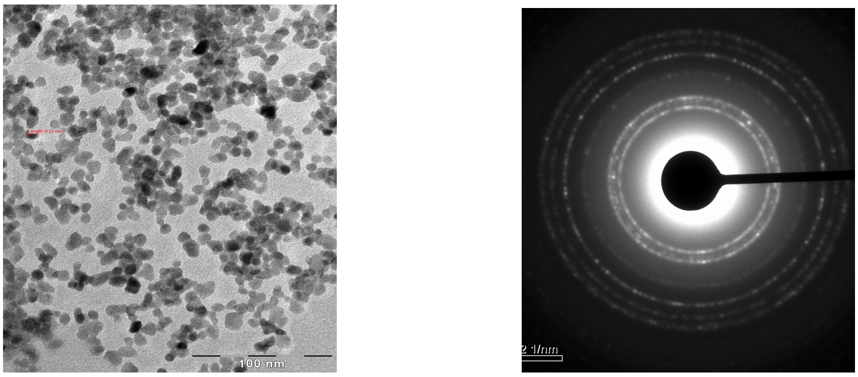

(a) (b)

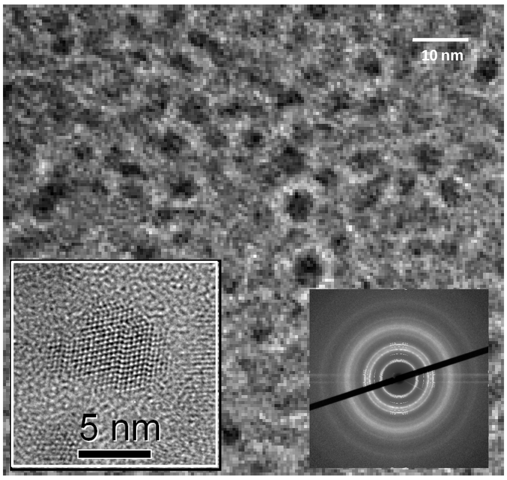

(c)

Figure 1.2 (a) TEM image of ZnO QDs. Scale bar =100 nm. (b) Electronic diffraction pattern of ZnO QDs. (c) TEM image of ZnO-CdS core-shell QDs. Scale bar = 10 nm. Inset (left): High resolution TEM image of ZnO-CdS core-shell QDs. scale bar = 5 nm. Inset (right): Electronic diffraction pattern of ZnO-CdS core-shell QDs.

Figure 1.2(a) presents the TEM image of ZnO NPs. The average diameter of NPs is 5.0 nm with standard deviation of 0.4 nm, as measured from calibrated high-magnification TEM images and directly from high-resolution (HR-TEM) lattice images for several dozens of NPs groups dispersed on 3 mm diameter Cu-grids for 20 samples. The electron diffraction pattern in **Figure 1.2(b)** reveals that ZnO NPs possess a hexagonal structure as all the diffraction rings could be indexed using a hexagonal lattice. The (hkl) indices of the diffraction rings, starting from internal ring to outside, are matching to (100), (002), (101), (102), (110), (103), and (112) planes of wurtzite ZnO structure. **Figure 1.2(c)** shows TEM images of ZnO-CdS core-shell QDs, and their average diameter is 5.0 nm. Here, it is interesting to observe that the size of ZnO-CdS core-shell QDs is similar to that of ZnO core NPs. This unchanged size between the core NPs and resulting core-shell QDs could indicate that Cd-S ions replace Zn-O ions by the kinetically controlled substitution ion-exchange reaction at the ZnO core surface to form CdS shells rather than building CdS coating layers over ZnO core. It should be noted that the similar replacement of atoms between Cd and Ag was observed in CdSe QDs.[23] The electronic diffraction pattern in the inset of **Figure 1.2 (c)** matches most of hexagonal CdS lattice d-spacings with a slight lattice shift toward ZnO. This observation supports our hypothesis, and it shows that the crystalline structure of core-shell ZnO-CdS QD matches the hexagonal CdS, which is not its native structure. Under this hypothesis, it is reasonable that the CdS shell inherits the hexagonal structure of ZnO core because Cd-S ions replace Zn-O ions of the core where the structure is hexagonal. In the inset of **Figure 1.2(c)**, lattice fringes are clearly observed in the high-resolution TEM images of the core-shell sample, and these fringes persist throughout the entire nanocrystal, indicating the dislocation-free epitaxial growth with full elastic crystalline-lattice matching between the core and shell compositions. Since the lattice mismatch between the core and shell is too small in ZnO-CdS QDs to resolve them clearly in HRTEM, in the next paragraphs these QDs are firmly verified to be neither homogeneous alloy of CdS and ZnO nor pure hexagonal CdS NPs by their energy disperse X-ray spectrum and photoluminescence lifetime study.

To confirm that these core-shell QDs consist of ZnO and CdS, these QDs were analyzed by local X-ray emission using an EDS Thermo-Noran system, equipped with a X-ray Si (Li) detector attached to a JEOL3000F microscope. Using the smallest condensor aperture, all X-ray data for NPs were acquired in special nano-area illumination (probe size ~20 nm) high-resolution imaging mode, which allowed for HR-

TEM imaging and parallel X-ray data recording in a random search for single NPs observed within the focused nano-probe image (**Figure 1.3**).

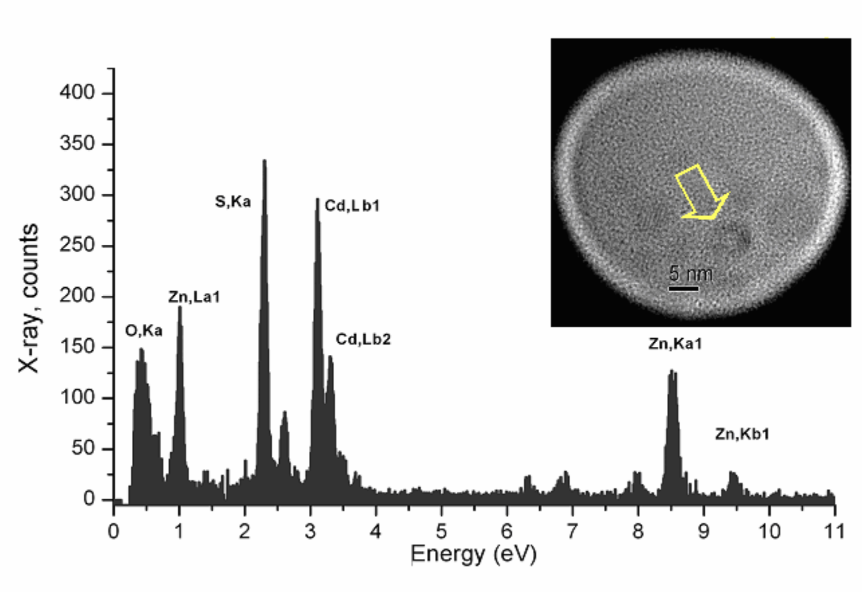

Figure 1.3 Elemental analysis of ZnO-CdS QD by energy-dispersive X-ray (EDX) spectroscopy. Inset shows TEM image of the single ZnO-CdS QD (arrow) for the EDX spectrum.

The X-ray spectrum shows $\text{ZnK}_{\alpha1}$, $\text{ZnK}_{\beta1}$, OK_{α}, SK_{α}, $\text{CdL}_{\beta1}$ and $\text{CdL}_{\beta2}$ lines, recorded by using the focused electron beam probe, which represents an accurate result for a single QD. It should be noted that this spectrum is reproducibly consistent among 50 different particles and even with larger QDs formed by aggregating 3 ~ 4 NPs. The ratio of peak intensities between Cd-S and Zn-O in this core-shell QD was 1: 0.4 on average, determined from relative X-ray peak intensities by using Vista 2.3 microanalysis software and thin correction. This ratio indicates that the CdS shell has a larger size and relative weight as compared to the ZnO core in the QD. The dominant weight of a CdS shell from the X-ray spectrum is consistent with the diffraction pattern for ZnO-CdS QD in **Figure 1.2 (c),** where diffraction is also dominated by the hexagonal CdS-like phase.

While all TEM and EDS results indicate that these QDs consist of a ZnO core and CdS shell, a distinct crystalline boundary between the core and shell is difficult to resolve because of the very small lattice mismatch in homomorphic epitaxial hetero-structures between wurtzite ZnO and CdS (< 7% in bulk). Therefore, whether the core-shell QDs produce *p-n* hetero-junctions for the type-II band structure offset or create a random alloy with no band structure offset, can be best addressed by direct optical measurements and exciton lifetime measurements for ZnO-CdS QDs. In **Figure 1.4 (a)**, ZnO NPs exhibit typical absorption spectra for type-I QDs with an excitonic peak at ~355 nm (3.49 eV), and a similar absorption band was observed by other groups.[24] When ZnO NPs were coated by CdS shells, the distinctive absorption edge for the type-I ZnO cores was replaced by a relatively smooth tail with a small shoulder observed at ~450 nm. This is a

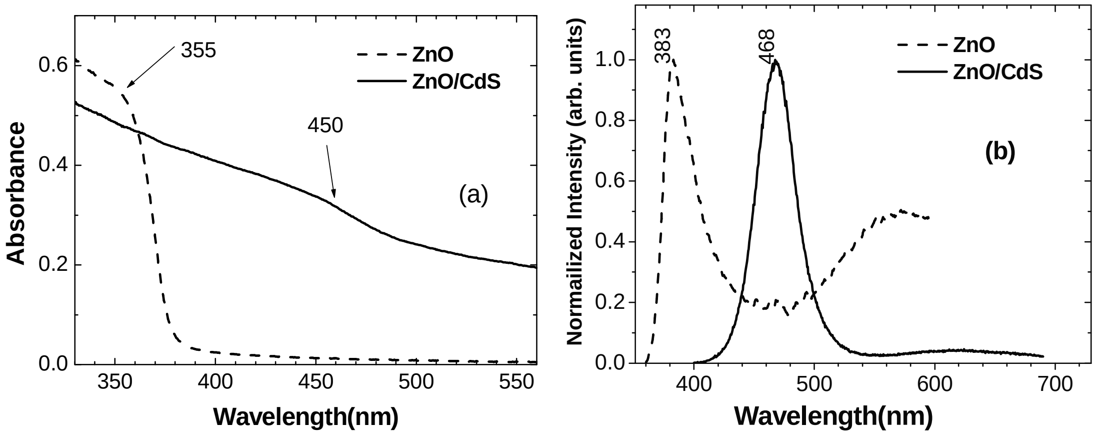

Figure 1.4 (a) Absorption spectra and **(b)** photoluminescence spectra of ZnO QDs (dotted line) and core-shell ZnO-CdS QDs (solid line).

characteristic spectral signature of the type II QDs because the absorption of type-II QDs is effectively suppressed with a peak broadening in their spectra as compared to the type-I QDs due to the weaker oscillator strength with a decrease in wavefunction overlap caused by the indirect spatial nature of long-lived exciton and larger variation of transition energies.[25] Therefore, the spectrum of QDs in **Figure 1.4 (a)** is consistent with the spectral feature for the characteristic type-II QD heterostructure.[17, 19, 20, 26] The photoluminescence (PL) peak of the core-shell QD appears at 468 nm in **Figure 1.4 (b)**, and the PL peak was red-shifted with the thickness of the CdS shell (see **Figure 1.5**).

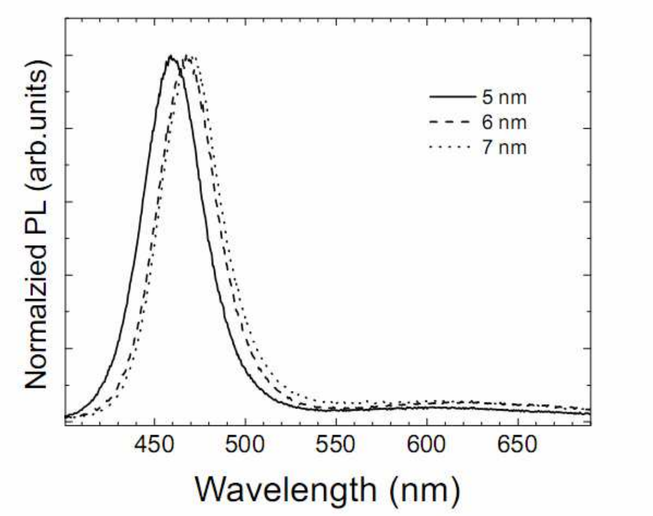

Figure 1.5 PL spectra of the core-shell QDs with different QD diameters. CdS shell thickness is proportional to the QD diameter as the core maintains the original size or less during the shell growth.

If these ZnO NPs were not coated by CdS shells, PL peaks and absorption edges of pure ZnO should have been observed in this spectrum. Therefore, the lack of these combination peaks in **Figure 1.4 (b)** also supports the formation of core-shell QDs. For the type-II core-shell QDs, the electron-hole recombination energy is significantly reduced due to the core-shell structure (see **Figure 1.1**), even though the influence of NP size confinement to the band gap energy is taken into account. Therefore, the red-shift of the PL peak from 383 nm to 468 nm is consistent with the core-shell formation. It should be noted that when the CdS precursors were not added to the solution of the core NPs in the drop-wise manner and the growth speed of the shell was increased, the PL peak and the absorption peak of resulting QDs was shifted back to the 485 nm and 470 nm respectively, corresponding to the spectral positions of neat CdS.[27] At this point, the ion-exchange reaction between Zn-O and Cd-S was completed under this fast growth condition, and the consumption of the core resulted in producing pure CdS NPs.

As discussed above, in general, for core-shell nanoparticles with a diameter less than 10 nm, the core is very difficult to distinguish from the shell by TEM and diffraction because the lattices of the core and the shell are matching very closely. To firmly verify the type-II characteristics of this core/shell QD, we compared the PL lifetimes of the ZnO-CdS core-shell QDs with different thicknesses of the CdS shell as shown in **Figure 1.6**. The diameter of each core-shell QD is labeled for the corresponding spectrum, and the shell thickness is assumed to proportionally increase with the diameter of the QD as long as the core maintains the original size or less during the shell growth on the core. Typically, the PL lifetime of type II QDs becomes slower as the shell thickness increases due to extended excitonic lifetimes with more discrete charge confinement.[18]

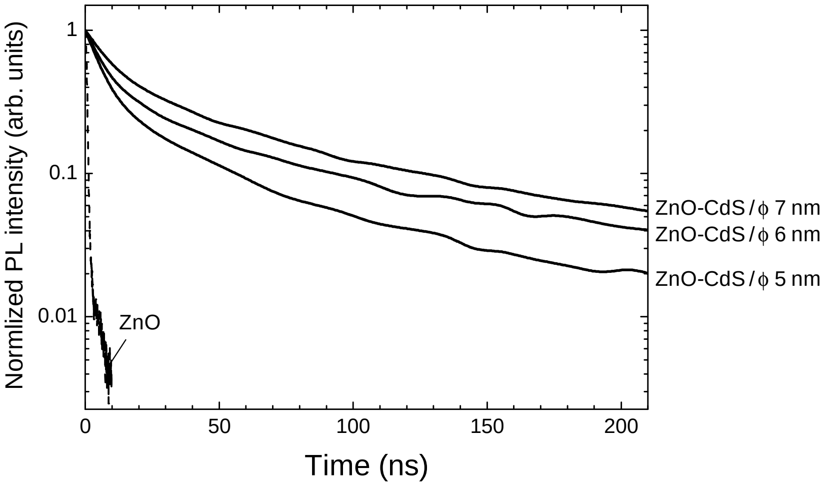

Figure 1.6 Time-resolved PL decays for pure ZnO and core-shell ZnO-CdS QDs with different QD diameters. CdS shell thickness is proportional to the QD diameter as the core maintains the original size or less during shell growth.

In **Figure 1.6**, PL-lifetimes of ZnO-CdS QDs increase as the CdS shell becomes thicker and the excitonic lifetime of core-shell QDs with the thickest shell is at least 100 times greater than the neat type-I ZnO QD with a lifetime of 1 ns. If the resulting QD is not the core-shell NP, the NP is the type-I QD, and its PL lifetime becomes short. However, the excitonic PL lifetime of our QD is on the order of 100 ns; this long lifetime strongly indicates that this NP is the type-II QD with a staggered band alignment between the core and the shell. Then, the only possible structure for the resulting NP to have the type-II characteristics is the hybrid one with ZnO as the core and CdS as the shell. This is also supported by the red-shift of PL peak with an increase in shell thickness as discussed above. It is unlikely that this slow PL lifetime is caused by a defect of the shell because the lifetime changes as a function of shell thickness. This observation of the much longer PL lifetimes of ZnO-CdS QDs also eliminates the possibility that these QDs are alloy of ZnO and CdS with the homogenous hexagonal crystalline structure because the alloy cannot have the type-II characteristics, and then the lifetime should have been as fast as the type-I QDs.

1.4 Conclusion

The ZnO-CdS type-II core-shell QDs were synthesized at relatively low temperature. All HRTEM images, ED patterns, and EDX spectrum suggest that these QDs have a heterogeneous ZnO core - CdS shell structure, and analysis from UV-Vis absorption spectra, PL spectra, and PL lifetime measurements firmly confirm that these core-shell ZnO-CdS QDs possess the type-II band structure offset. The spatial electron-hole separation between the core and the shell, greatly enhanced by the type-II band structure offset in the ZnO-CdS QD heterostructures, results in the extremely long exciton lifetime. These type-II ZnO-CdS QDs can be excited and detected in the visible range, and therefore, these QDs with such long exciton lifetimes could have an advantage to be applied in the fields of photo-luminescent markers, medical imaging, photonics, solar cells, nano-electronics, and biosensors.

Chapter 2

Raman and Surface Enhanced Raman Scattering of 3-Hydroxyflavone

2.1 Introduction

Over 4000 chemically unique flavonoids have been identified in plant sources.[1] These low-molecular-weight substances, found in all vascular plants, are phenyl-benzopyrones (phenylchromones) with an assortment of basic structures. One of these compounds is 3-hydroxyflavone (3-HF, **Scheme 1**). The flavonoids are involved in photosensitization and energy transfer. They display a remarkable array of biochemical and pharmacological actions, some of which suggest that certain members of this group of compounds may significantly affect the function of multiple mammalian cellular systems. [2-7]As a member of the flavonoid family, 3-HF has been extensively examined for many years for structural and chemical properties by means of IR, UV, PMR, and NMR. [1,2,8,9] Specifically, it has been used since 1979 as a prototype molecule for studies of the mechanism of excited-state intramolecular proton transfer and photoisomerization by means of electronic spectroscopy and nanosecond to picosecond time-resolved fluorescence measurements.[10-13]The structures of several flavone derivatives of interest are shown in **Scheme 1**.

SCHEME 1: Flavone Derivatives

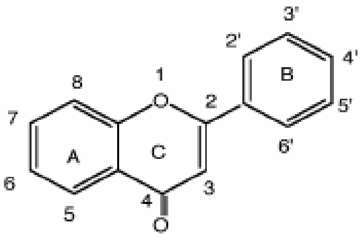

flavone

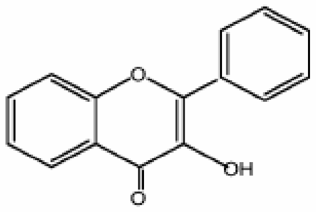

3-hydroxyflavone

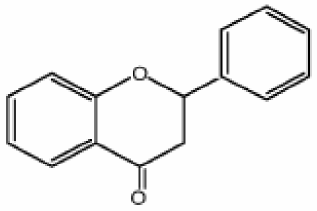

flavanone

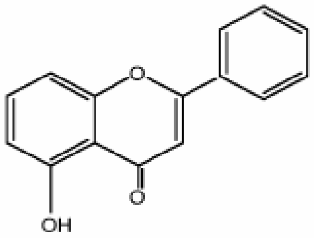

5-hydroxyflavone

Much information on the molecular vibrations of 3-HF has been provided by infrared spectroscopy.[14-19] The published IR data in the double bond and hydroxy stretching regions reveal certain unusual features in 3-HF and some substituted derivatives, which could not be rationalized by the usual frequency structure correlations. The carbonyl absorption in flavanone is observed at 1695 cm^{-1} but in flavone it is at 1649 cm^{-1}, showing the frequency decrease resulting from the increased conjugation of the carbonyl group with the pyrone ring through the C=C bond at the 2,3 position. Compared with 1649 $cm^{-1}$of flavone, the carbonyl frequency of 3-HF is further lowered to 1610 cm^{-1} and overlaps with the frequency of the C=C band. There is some controversy about what causes this shift to lower frequency. It has been suggested that there is strong chelation between the C=O and OH groups.[14-16] In the C-H and O-H stretching region (2000-4000 cm^{-1}), the IR spectrum of 5-hydroxyflavone does not contain an observable band readily assignable to O-H stretching, clearly establishing 5-HF as an intramolecular hydrogen-bonded compound. The IR spectra of 3-HF in the C-H and O-H stretching region, however, were reported differently by various researchers.[14-16] Thus, Jose et al.[15] concluded that there is no strong hydrogen bonding in 3-HF and that the low-frequency characteristics of the C=O and C=C bands arise from structural features. A more recent FTIR study [20] involves a study of several flavanols in Ar and methanol/Ar matrices at 10 K.

Despite the extensive body of infrared spectroscopy on 3-HF, there is almost no Raman work reported. The only one, which could be found after extensive searches, was a reference to an unpublished resonance Raman spectrum in 3-methyl pentane at room temperature by Collins.[20] Bands at 1650 and 1625 cm^{-1} were reported. The reason for the lack of extensive Raman work is most likely that the compound is quite insoluble in water. However, there is still considerable value in obtaining good Raman spectra. This is especially true since recent advances in surface enhanced Raman spectroscopy (SERS) have provided tools for detection of molecules at extremely low concentration.

Development of Raman probes have been made for purposes of biosensors, [21] application in forensics, [22, 23] as well as art preservation.[24] It is with these considerations in mind that we turned our attention to the Raman spectroscopy of 3-hydroxy flavone. Here we report the Raman spectrum of solid 3-HF as well as SERS spectra of the compound in solution on an electrochemically roughened Ag electrode surface as well as on Ag colloidal nanoparticles. Further verification of our results was obtained with a spectrum of the Al+ complex of 3-HF, and the spectral assignments are aided by DFT calculations.

2.2 Experimental Section

The experimental set up for normal Raman and electrochemical SERS studies has been described in previous papers.[26] A Spectra Physics model 2020 BeamLock argon ion laser line at 488 nm was used as a Raman excitation source. Spectra were recorded with a Spex model 1401 double monochromator with a resolution of 2 cm^{-1}. Photon-counting detection was used. The laser power was approximately 30 mW in the SERS experiment and only 5 mW in the NR experiment. 3-HF was purchased from the Aldrich Chemical Co. Inc., used as received. The NR spectrum of solid 3-HF has been obtained in the region of 100-4000 cm^{-1} directly from a pure powder sample. SERS spectra of 3-HF were obtained at different pH values and different applied potentials with an activated Ag electrode, which had 3-HF adsorbed on it. For acidic conditions, 3-HF was first dissolved in a small amount of CH_3OH and then diluted by a 0.1 M K_2SO_4 solution for which the pH value was adjusted with a 0.1 M H_2SO_4 solution. For basic conditions, a 0.1 M NaOH solution was used to adjust the pH of a 0.1 M K_2SO_4 sample solution. In SERS experiments, the sample cell consisted of a silver working electrode, a Pt counter electrode, and a saturated calomel electrode (SCE) as the reference. All potentials reported in this work are quoted vs. SCE. For activating an Ag electrode, the polished Ag electrode was roughened by an oxidation-reduction cycle (ORC) pretreatment, which was accomplished in the solution of 3-HF ($2 * 10^{-5}$ M) in 0.1 M K_2SO_4 aqueous solution by applying a potential pulse from -0.4 to +0.5 V for 2 second. 3-HF was adsorbed on the Ag electrode surface during the ORC. Nonadsorbed 3-HF molecules were then washed from the electrode by distilled water. After the ex situ ORC pretreatment, the activated Ag electrode was placed in a 0.1 M K_2SO_4 aqueous solution for carrying out SERS experiments at various potentials. The same spectra were obtained with in situ ORC and direct recording of SERS spectra in the flavone solutions. ORC pretreatment and potential control during the SERS experiments were carried out by using an EG&G PARC model 175 universal programmer and an EG&G PARC model 173 potentiostat. FTIR spectra of solid 3-HF were recorded with a Nicolet model Impact 400 FTIR spectrometer. Ag colloidal nanoparticles were prepared following the method of Lee and Meisel[27] by reduction of silver nitrate (Aldrich 209139 silver nitrate 99.9%) with sodium citrate (Aldrich W302600 Sodium Citrate Dihydrate). The colloid thus prepared shows an absorption maximum at 406 nm and fwhm of 106 nm, as measured with a Cary 50 UV-vis spectrophotometer (after a 1:4 dilution with ultrapure water to keep maximum absorbance within the instrumental range). To further concentrate the colloid for use, a volume of 10 mL of the original colloid was centrifuged at 5000 rpm for 2 min. The supernatant was discarded, and the settled portion was resuspended in 1 mL of ultrapure water. All glassware was cleaned with Pierce PC54 cleaning solution and rinsed with ultrapure water and finally in acetone and methanol. This method proved to be as effective as the use of aggressive cleaning agents such as aqua regia or piranha solution and was preferred for health and safety reasons. Only ultrapure water was used for the preparation of the various solutions. SERS measurement were made simply by adding 1μL of dye solution to a 2 μL drop of colloid deposited on a gold coated microscope slide, followed by addition of 2 μL of a 0.2 M KNO_3 solution. Raman measurements were taken directly from the drop using a 10X or 20X microscope objective and focusing on the microscope slide surface. SERS spectra could be obtained two or 3 min after addition of the KNO_3 and remained constant in quality until evaporation of the liquid. Raman spectroscopy for SERS on Ag colloidal nanoparticles was performed with a Renishaw Raman System 1000 in combination with a Leica DM LM microscope. A 1200 lines/mm grating was used in combination with a thermoelectrically cooled CCD detector to monitor the Raman spectra between 200 and 1800 cm^{-1} with an integration time of 20 s. Excitation light from a CW diode laser at 785 nm and maximum power of 8 mW was focused down onto the sample with 10X or 20X objective lenses. Density functional theory (DFT) frequency calculations were performed with Gaussian 0328 at the B3LYP level of theory employing the 6-31+G* basis set. The geometry optimization resulted in a planar geometry, and no imaginary frequencies were observed in the calculated spectrum. Calculations for adsorption geometry with 3-HF bound to a Ag20 cluster were also made with DFT at the B3LYP level using the NWChem electronic structure program package29 on the Rachel supercomputer at the Pittsburgh Supercomputer Center and results displayed with GaussView.

2.3 Results and Discussion

The flavone structure in **Scheme 1** shows the structure and atomic numbering of the phenylchromone ring, which will be used in the discussion of all of the flavone compounds studied. For convenience in analysis and discussion, we designate the benzo ring in the chromone system as ring A, the phenyl ring as ring B, and the pyrone ring as ring C. We have calculated geometry optimized surface structures of 3-HF on Ag with DFT (B3LYP/DZVP (Ag), 6-31G** (O), 6-31G (all other atoms) based on a model employed by Schatz and co-workers[30] for possible SERS active Ag sites. These surface sites are represented by a 20 atom tetrahedral Ag cluster, with the molecule bound in either the S-complex (surface) or the V-complex (vertex) sites. These two geometrical optimized structures (b), S-complex, and (c), V-complex, are shown in **Scheme 2** along with (a) the geometrical optimized 3-HF structure calculated with DFT (B3LYP/6-31G**).

SCHEME 2: Ball and Stick Model with Ag Cluster

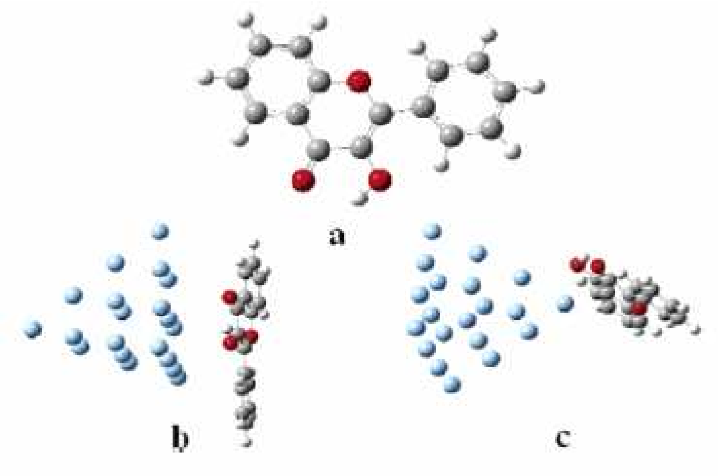

The surface structures were found to have nearly the same energy (S-complex < V-complex by only 0.01 eV) for bound 3-HF. In 3-HF bound in the on-top S-complex (b), which represents the Ag(111) face of fcc silver, the molecule is nearly parallel to the surface and interacts with two Ag atoms at least 3 Å from the surface, whereas in the V-complex (c), which represents an adatom site, the molecule is bound tilted at an angle of ca. 53° with respect to the Ag(111) surface plane and interacts with the silver apex adatom at its carbonyl group (i.e., with the Ag-O (O=C) distance of 2.37 Å, the Ag-C (O=C) distance of 2.38 Å, and the Ag-O (O-H) distance of 3.15 Å). The molecular structure of 3-HF is nearly the same in all three of the forms in Scheme 2 with the bond distances within 0.01 Å of each other except for those 3-HF atoms (the O=C-C-OH moiety of the pyrone ring) interacting with the Ag adatom of the Ag_{20} clusters. Since the SERS spectra to be presented show enhancement of in-plane vibrational modes, this fact is consistent with the V-complex as the SERS active form according to the dipolar plasmon surface electromagnetic, EM, selection rules of SERS. The V-complex structure shows that the entire molecule can be at an angle of 53° with respect to the plane of the surface and that the apex Ag adatom binds the O=C-C-OH moiety of the pyrone ring below the molecular plane with the surface bond Ag-O=C bent at an angle of 69.4°.

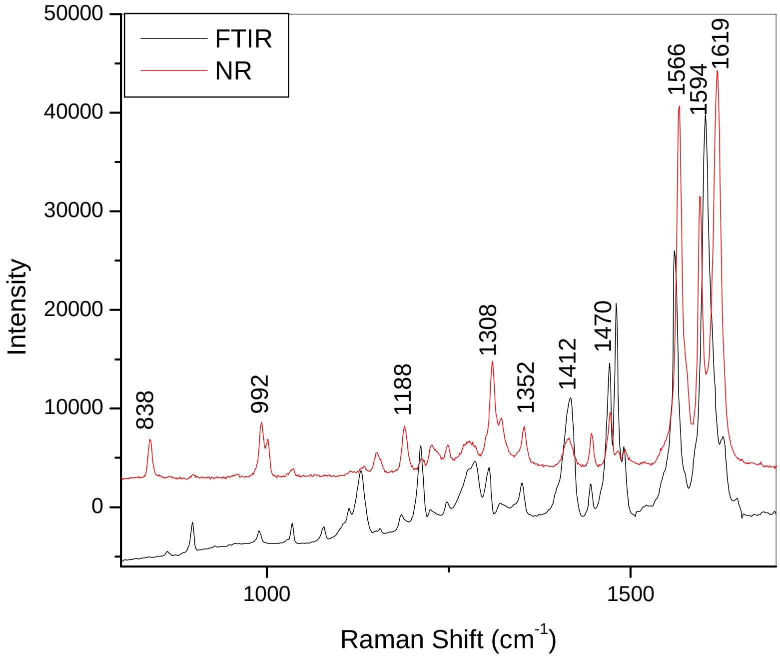

Figure 2.1 Comparison of the normal Raman (NR) and Fourier transform infrared (FTIR) spectra of solid 3-hydroxyflavone.

Figure 2.1 shows a comparison of the NR and FTIR spectra of solid 3-HF. In the figure in red, the NR spectrum of 3-HF in the 800 to 1700 cm^{-1} spectral region is displayed for a pure solid sample, whereas in black, the FTIR spectrum in the same region for a KBr pellet is shown. The FTIR spectrum of 3-HF obtained in our work is consistent with the IR results previously reported by Looker and Hanneman. [14] Since 3-HF possesses no symmetry the FTIR and NR spectra are quite similar in appearance, except for relative intensities. Thus, Raman bands should have assignments, which are not too different from the FTIR vibrations. According to previous IR results, [14-19] the presence of a hydroxy group in the 3-position lowers the frequencies of both the carbonyl and C2=C3 stretching mode, so that the band at 1610 cm^{-1} in FTIR (1594 cm^{-1} in NR and SERS) represents the decreased double bond character of the carbonyl group and the aromatic character of the pyrone ring (i.e., the overlapping of C=O with C=C). The band at 3070 cm^{-1} in NR can be attributed to an unsaturated C-H stretching vibration. The band at 1351 cm^{-1} in FTIR (1352 cm^{-1} in NR and 1354 cm^{-1} in SERS) is attributed to an O-H in-plane deformation. The bands in the region from 1400 to 1600 cm^{-1} are associated with aromatic in- plane skeletal vibrations, double bond character of the carbonyl group and the aromatic character of the pyrone ring (i.e., the overlapping of C=O with C=C). It is more difficult to assign the two benzene ring systems, and for accuracy in all of the assignments, we did a DFT calculation for comparison with the experimental results.

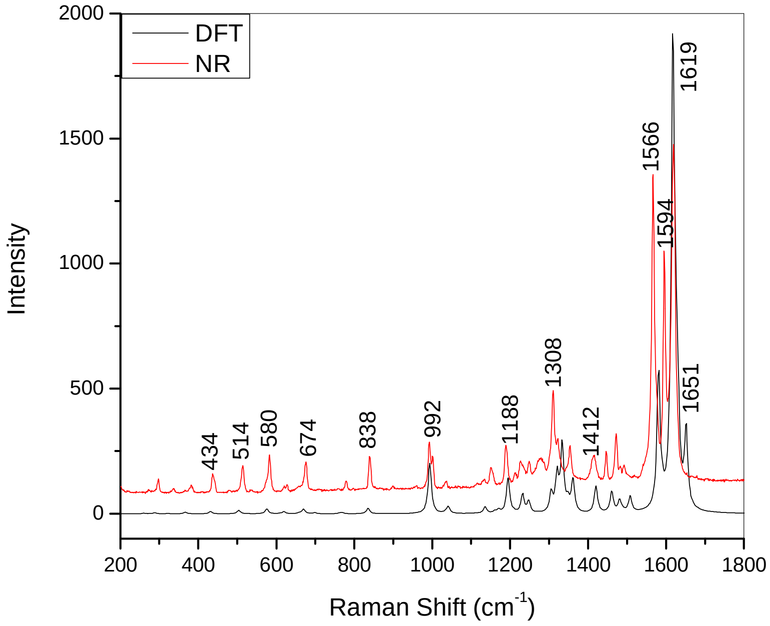

Figure 2.2 Comparison of the normal Raman (NR) spectrum of the powder sample with the spectrum calculated from the density functional (DFT) results. The latter have been scaled on the frequency axis by a factor of 0.98 from the calculated output.

In **Figure 2.2**, we compare the results of the normal Raman spectrum of the powder sample with the spectrum calculated from the DFT results. Detailed frequency measurements and calculated frequencies are listed in column 3 of **Table 2.1**. The raw frequencies from the calculation have been adjusted by a factor of 0.98. It can be seen that the calculated spectrum provides an excellent fit to the observed result. This indicates that the assignments given in the first two columns of the table are most likely correct.

TABLE 1: Density Functional Calculations and Spectral Assignments of 3-HF[a]

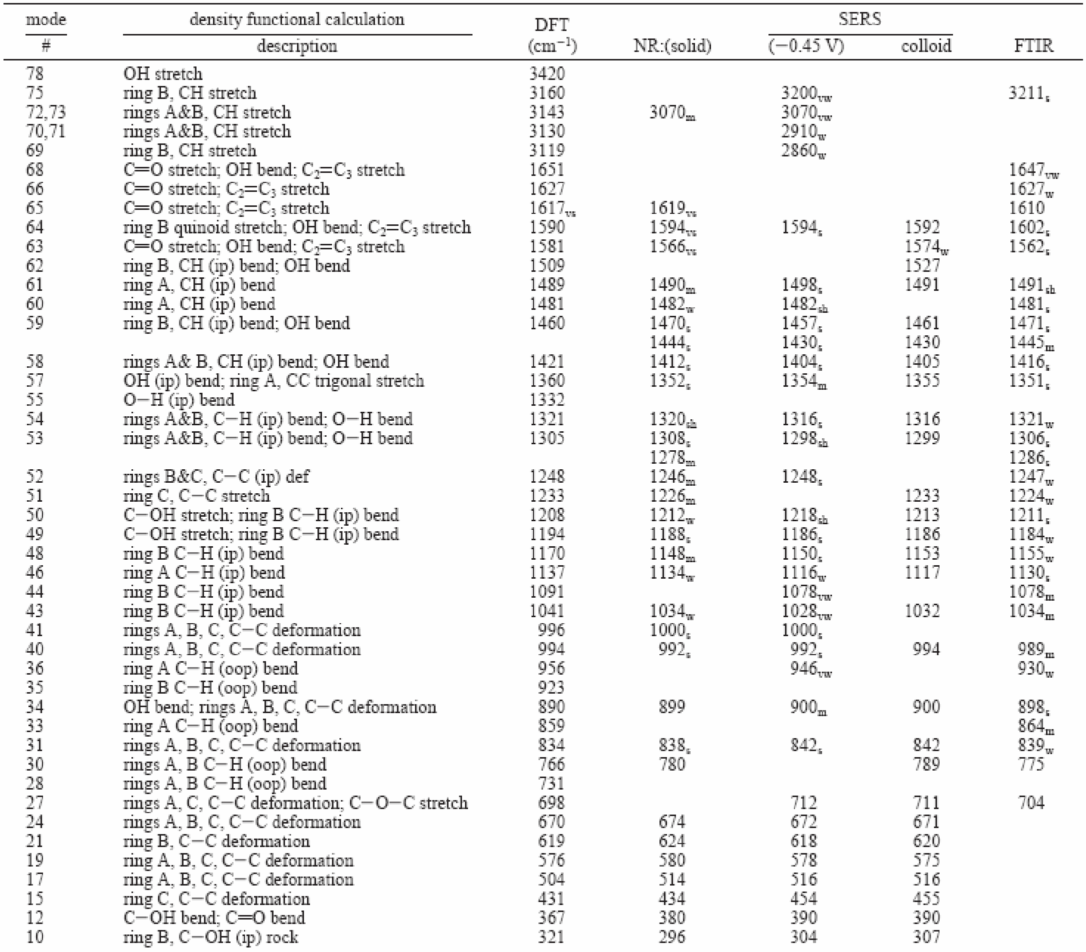

mode	density functional calculation	DFT		SERS		
#	description	(cm^{-1})	NR:(solid)	(−0.45 V)	colloid	FTIR
78	OH stretch	3420				
75	ring B, CH stretch	3160		3200_{vw}		3211_{s}
72,73	rings A&B, CH stretch	3143	3070_{m}	3070_{vw}		
70,71	rings A&B, CH stretch	3130		2910_{w}		
69	ring B, CH stretch	3119		2860_{w}		
68	C=O stretch; OH bend; $C_2=C_3$ stretch	1651				1647_{vw}
66	C=O stretch; $C_2=C_3$ stretch	1627				1627_{w}
65	C=O stretch; $C_2=C_3$ stretch	1617_{vs}	1619_{vs}			1610
64	ring B quinoid stretch; OH bend; $C_2=C_3$ stretch	1590	1594_{vs}	1594_{s}	1592	1602_{s}
63	C=O stretch; OH bend; $C_2=C_3$ stretch	1581	1566_{vs}		1574_{w}	1562_{s}
62	ring B, CH (ip) bend; OH bend	1509			1527	
61	ring A, CH (ip) bend	1489	1490_{m}	1498_{s}	1491	1491_{sh}
60	ring A, CH (ip) bend	1481	1482_{w}	1482_{sh}		1481_{s}
59	ring B, CH (ip) bend; OH bend	1460	1470_{s}	1457_{s}	1461	1471_{s}
			1444_{s}	1430_{s}	1430	1445_{m}
58	rings A& B, CH (ip) bend; OH bend	1421	1412_{s}	1404_{s}	1405	1416_{s}
57	OH (ip) bend; ring A, CC trigonal stretch	1360	1352_{s}	1354_{m}	1355	1351_{s}
55	O−H (ip) bend	1332				
54	rings A&B, C−H (ip) bend; O−H bend	1321	1320_{sh}	1316_{s}	1316	1321_{w}
53	rings A&B, C−H (ip) bend; O−H bend	1305	1308_{s}	1298_{sh}	1299	1306_{s}
			1278_{m}			1286_{s}
52	rings B&C, C−C (ip) def	1248	1246_{m}	1248_{s}		1247_{w}
51	ring C, C−C stretch	1233	1226_{m}		1233	1224_{w}
50	C−OH stretch; ring B C−H (ip) bend	1208	1212_{w}	1218_{sh}	1213	1211_{s}
49	C−OH stretch; ring B C−H (ip) bend	1194	1188_{s}	1186_{s}	1186	1184_{w}
48	ring B C−H (ip) bend	1170	1148_{m}	1150_{s}	1153	1155_{w}
46	ring A C−H (ip) bend	1137	1134_{w}	1116_{w}	1117	1130_{s}
44	ring B C−H (ip) bend	1091		1078_{vw}		1078_{m}
43	ring B C−H (ip) bend	1041	1034_{w}	1028_{vw}	1032	1034_{m}
41	rings A, B, C, C−C deformation	996	1000_{s}	1000_{s}		
40	rings A, B, C, C−C deformation	994	992_{s}	992_{s}	994	989_{m}
36	ring A C−H (oop) bend	956		946_{vw}		930_{w}
35	ring B C−H (oop) bend	923				
34	OH bend; rings A, B, C, C−C deformation	890	899	900_{m}	900	898_{s}
33	ring A C−H (oop) bend	859				864_{m}
31	rings A, B, C, C−C deformation	834	838_{s}	842_{s}	842	839_{w}
30	rings A, B C−H (oop) bend	766	780		789	775
28	rings A, B C−H (oop) bend	731				
27	rings A, C, C−C deformation; C−O−C stretch	698		712	711	704
24	rings A, B, C, C−C deformation	670	674	672	671	
21	ring B, C−C deformation	619	624	618	620	
19	ring A, B, C, C−C deformation	576	580	578	575	
17	ring A, B, C, C−C deformation	504	514	516	516	
15	ring C, C−C deformation	431	434	454	455	
12	C−OH bend; C=O bend	367	380	390	390	
10	ring B, C−OH (ip) rock	321	296	304	307	

In the first three columns, we present the mode numbers, a brief description of the major contributions to the normal mode, and the calculated vibrational frequencies from the density functional calculation. The frequencies have been scaled by a factor of 0.98 from the calculated frequencies. The fourth column gives the normal Raman spectrum of the powder, and the fifth and sixth columns give the SERS spectra on an electrode at -0.45 V and on the colloid. The last column presents the FTIR spectrum. In column 1, we provide the normal mode identification number from the DFT calculation, and in column 2, we provide a brief description of the largest vibrational contributions to the normal mode.

The major differences between the observed spectrum and a previously unpublished solution resonance Raman spectrum reported in a footnote (ref 20) is that in the latter the bands at 1650 and 1625 cm^{-1} were reported to be intense, whereas for the NR spectrum reported here, they are rather weak, especially compared with the very strong band at 1619 cm^{-1}. The difference is most likely due to the differing intensities in the resonance and nonresonance Raman effect, although the matrix may also have an important effect. Note also except for the band at 1594 cm^{-1} (υ64) all of the bands between 1566 and 1619 cm^{-1} involve the C=O stretch and the C2=C3 stretch, with some degree of O-H bend. Furthermore, the high-frequency region (above 2000 cm^{-1}) involves mostly C-H stretches, which are observed to be rather broad in the FTIR and SERS spectra, and the O-H stretch, which is quite weak, if seen at all, in all of the observed spectra. Our (scaled) calculation is somewhat higher than that reported in earlier calculations[20] but much closer to the value usually associated with O-H stretching vibrations. [31] Note also most of the lines between 1305 and 1509 cm^{-1} involve the in-plane CH bending vibration.

We have obtained SERS spectra of 3-HF on roughened silver electrodes at numerous applied potentials and for various pH values. The maximum intensity observed is at -0.45 V. In **Figure 2.3**, we display the SERS spectrum (in the range 200- 1700 cm^{-1}) of 3-HF at pH 10.5 on a roughened Ag electrode at two applied potentials: (a) -0.45 and (b) -0.75 V. The spectra are quite similar and do not vary much with potential, except in overall intensity. Cyclic voltammetry in the presence and absence of 3-HF on roughened silver electrodes indicates that there are no faradaic processes in the potential region from -0.3 to -0.9 V. **Figure 2.4** shows the SERS spectra of 3-HF at both potentials in the higher frequency region of 2200-3600 cm^{-1}. There, the spectra differ somewhat.

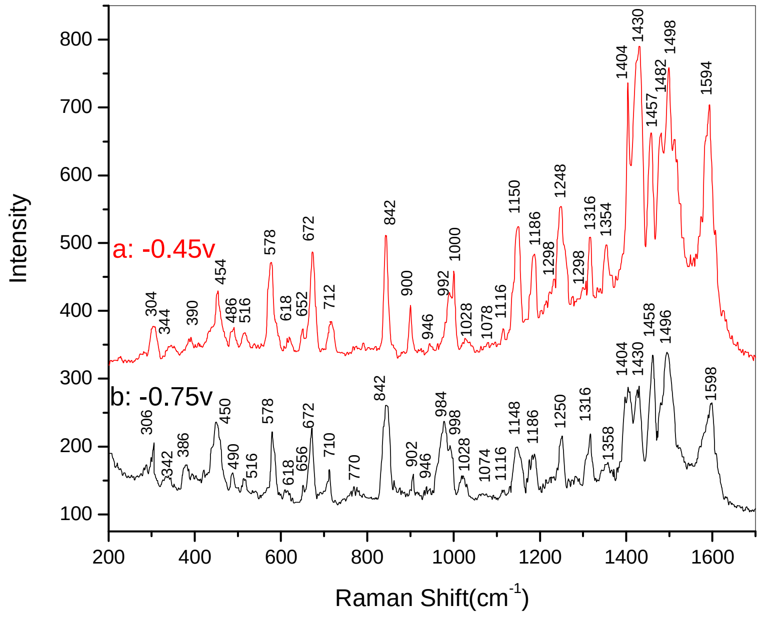

Figure 2.3 Surface enhanced Raman spectrum (SERS) of 3-hydroxyflavone (3-HF) at pH 10.5 on a roughened Ag electrode at two applied potentials: (a) -0.45 and (b) -0.75 V, in the range 200-1700 cm^{-1}.

The lines at 2860 and 2910 cm^{-1}, attributed to various ring C-H stretches are shifted somewhat at -0.75 V. The two weaker lines at 3070 and 3200 cm^{-1} disappear at -0.75 V, but a new line appears at 3010 cm^{-1}. It is difficult to interpret these changes, since there are numerous C-H vibrations in this region, all with similar frequencies. The quite broad band centered at 3366 cm^{-1} is observed only at -0.75 V and may be the elusive O-H stretch, which is predicted to be at 3420 cm^{-1} in the DFT calculations. It is too high to be any of the C-H stretches. The observed broadness as well as lower frequency may be induced by inhomogeneities due to proximity of the O-H to the electrode surface.

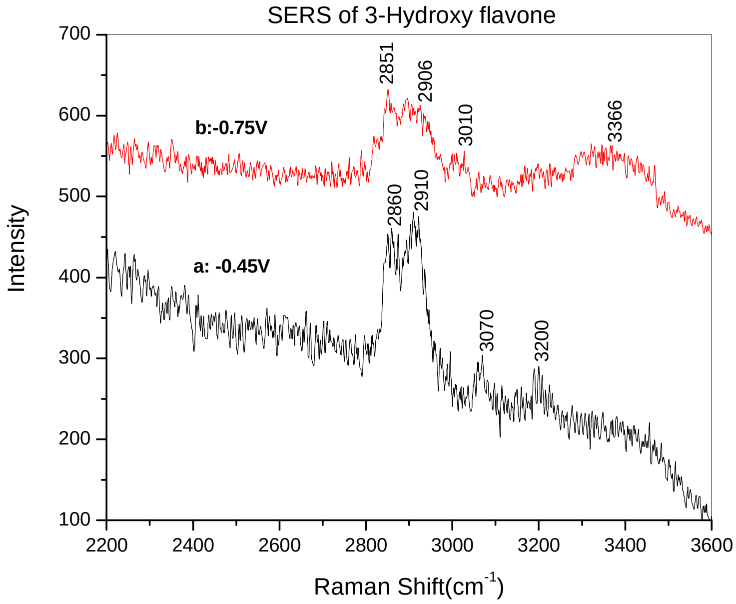

Figure 2.4 Surface enhanced Raman spectrum (SERS) of 3-hydroxyflavone (3-HF) at pH 10.5 on a roughened Ag electrode at two applied potentials: (a) -0.45 and (b) -0.75 V, in the range 2200-3600 cm^{-1}.

In order to examine the differences between the SERS spectrum on Ag colloidal nanoparticles and that on the electrode, we present both spectra in **Figure 2.5**. By and large the spectra are quite similar, except that the line at 1527 cm^{-1} (υ62) is very intense on the colloid and weak on the electrode. Furthermore the 1405 cm^{-1} (υ58) and 516 cm^{-1} (υ17) bands are similarly much stronger on the colloid. The latter vibration involves C-C in-plane deformation of the three rings, whereas the two at higher frequency are due to C-H in-plane bending motions. These higher frequency modes also involve C-O-H bending, and a much stronger interaction on the electrode of a positively charged Ag ad-ion with the oxygen atom of the C-O bond in ring C might damp the ring C motion. This observation is consistent with the rather broad band at 3420 cm^{-1} observed in the -0.75V SERS electrode spectrum, possibly the O-H stretch.

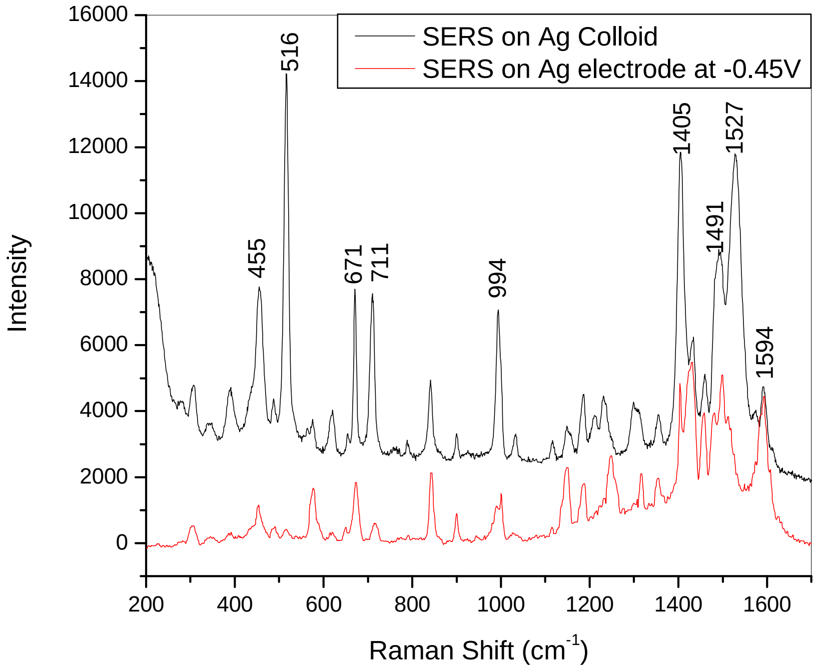

Figure 2.5 Comparison of surface enhanced Raman spectrum (SERS) of 3-hydroxyflavone on Ag colloidal nanoparticles with that on Ag electrode at -0.45V.

The most interesting result is illustrated in **Figure 2.6**, where we compare the NR spectrum of 3-hydroxy flavone with that of the SERS on the colloid in the spectral region between 1000 and 1800 cm^{-1}. We see immediately that the intense NR bands at 1566, 1594, and 1619 cm^{-1} (υ63-υ65) are suppressed on the surface, where the lines at 1405, 1491, and 1527 cm^{-1} (υ58, υ61, and υ62) become the most intense lines in the spectrum. The suppressed lines have either a strong C=O stretch coupled with a C2=C3 stretch or an O-H bend, whereas the surface enhanced lines all involve the C-H in-plane wag. These results (in addition to the concomitant results on the Ag electrode) indicate strongly that the molecule is attached to an Ag adatom on the metal surface, reducing the intensity of the modes involving C=O and C2=C3 stretch. The strong enhancement of the C-H in plane wags indicates that the planar rings involved are oriented perpendicularly to the metal surface as indicated by the adsorption geometry in molecular structure c in **Scheme 2**. This is also consistent with suppression of the 1627 cm^{-1} mode in the SERS on the Ag electrode where a Ag adion could be involved in the bonding of the O=C(4)-C(3)-OH part of the molecule to the surface.

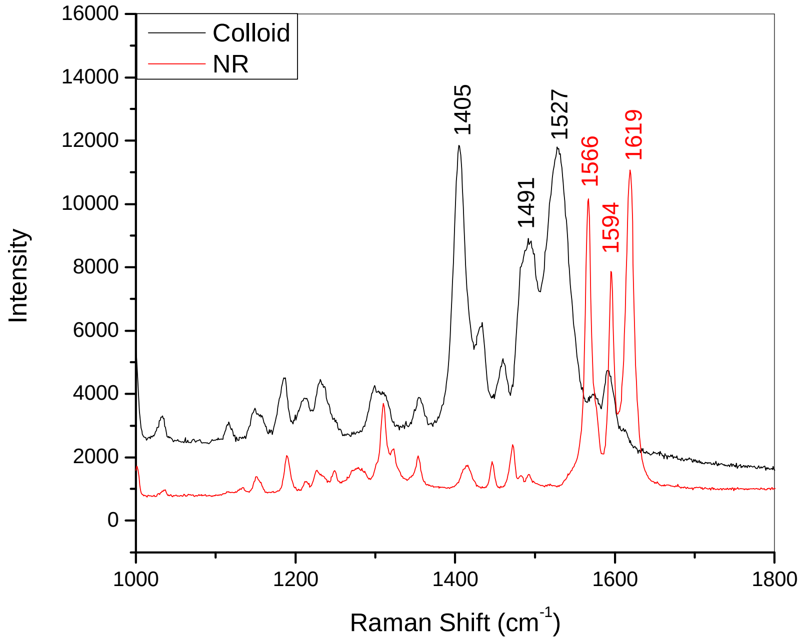

Figure 2.6 Comparison the NR spectrum of 3-hydroxyflavone with that of the SERS on the colloid in the spectral region between 1000 and 1800 cm^{-1}.

Analysis of the electronic structure for a simple Ag-3HF model (B3LYP/ LANL2DZ) of the surface complex, using the natural bond order (NBO) analysis programs, shows that the surface bonding interaction involves two effects. There is a backbonding effect of charge transfer out of the Ag α 5s singly occupied orbital into σ* and π* antibonding C=O NB orbitals (MLCT), and in addition, there is also charge transfer from the *π* C=O bonding NB orbital into the vacant Ag β 5s orbital which changes from 1.54 in 3-HF to 1.41 in Ag-3HF. This analysis gives a Wiberg bond order of 0.09 between the Ag and the O of the carbonyl. These charge-transfer delocalization effects can be used to explain why the 1594 cm^{-1} band which contains the C=O stretching vibration shifts to higher wavenumber, 1598 cm^{-1}, at the more negative potential in **Figure 2.3**. The two charge-transfer effects move in opposite directions as the electrode potential is made more negative. Presumably at -0.75 V, which is probably slightly negative to the point of zero charge in 0.1 M K$_2$SO$_4$ on polycrystalline Ag, the delocalization out of the *ð* CdO NB orbital is reduced more than the back-bonding effect is increased by the negative surface charge leading to a slight increase in the band wavenumber. A more extreme possibility for the loss of the 1627 cm^{-1} band is a polymerization reaction at Ag surfaces which was suggested very recently to explain changes found in the Raman spectra of, 7-hydroxyflavonoids. [32] However, this is unlikely for 3-HF which cannot undergo catechol-like polymerization.

2.4 Conclusions

We have obtained the normal Raman spectrum as well as the SERS spectra of 3-hydroxyflavone. The SERS spectra are obtained on the Ag electrode at various applied potentials as well as on Ag colloids. Spectral assignments are made with the assistance of a density functional calculation, which matches quite well the normal Raman spectrum, as well as the FTIR spectrum. Thus, we are confident of the correct normal mode assignments. The spectral intensities of the in-plane modes are also consistent with the DFT calculated adsorption geometry. The major difference between the SERS results and those of the normal Raman involve the intensities of the bands in the 1600 cm^{-1} region which mainly involve the carbonyl stretch in conjunction with the hydroxy stretch and a ring C2=C3 stretch. The stark lowering of the observed intensities of these modes is indicative of the interaction of the molecule with the surface. The DFT calculations presented show that an adatom site at the vertex of Ag20 cluster binding with 3-HF molecular plane titled 53° to surface is a likely surface structure. The shift to lower wavenumber for the carbonyl stretching vibration on the surface is most likely the result of a surface interaction of the Ag adatom with the C=O lowering its bond order. We also observe a rather broad band near 3366 cm^{-1} on the Ag electrode, which in all likelihood is the OH stretch.

Chapter 3

Effect of Fluence on the Discoloration of Marble Cleaned with UV Lasers

3.1 Introduction

Marble, a metamorphic limestone, primarily consists of calcite, a crystalline form of calcium carbonate ($CaCO_3$). Marble is widely used in statues and monuments, as well as a structural material. Its exposure to a sulphur dioxide (SO_2)-polluted atmosphere, particularly in an urban environment, results in a thin layer of black encrustation due to the formation of gypsum ($CaSO_4 \cdot 2H_2O$). Sulphur dioxide from the combustion of fossil fuels readily reacts with the $CaCO_3$ present in the marble to form gypsum. The softer and more water-soluble gypsum is easily contaminated by soot particles containing metal oxide and graphite, as well as numerous organic constituents, further contributing to the generation of the black encrustation[1].

This encrustation has a detrimental effect on the aesthetic value of both artistic and practical marble structures. Moreover, the encrustation facilitates the biodeterioration of the marble since it can host bacteria, lichen, mosses, higher plants and other microorganisms [2]. Chemical cleaning is the traditional means for removing the encrustation. However, there exists the possibility of chemical reactions between the chemical agents utilized and marble, as well as the environmental pollution. The encrustation is also mechanically removed through using a scalpel or the air-abrasive machine. The effectiveness of the scalpel is restricted by the restorative talents of the restorer and the brittleness of the material. The results of air-abrasive machine treatments are also largely dependent on the restorer’s skill levels, as the machine cannot distinguish the encrustation from the stone. Due to the non-uniformity of the encrustation, unavoidable surface damage of the marble results in the loss of fine details of the artworks [3].

Pulsed laser removal of the encrustation is a promising alternative due to the fast and non-contact operation and the high-precision spatial and temporal control. In addition, the laser pulses can not damage the marble surface after the removal of the encrustation due to the large difference in the absorptivity between the encrustation and the marble, which is termed self-limiting [3]. Laser cleaning nano-particles from semiconductor surfaces [4] and surface layer from metals or semiconductors [5] have been extensively studied. Since the pulsed laser cleaning of the encrustation from the marble was first implemented by John Asmus in 1971 [6], massive investigations related to the laser cleaning of stoneworks have been performed.

Laboure et al. [7] explored the effect of laser fluence, spot area, and water spraying on the cleaning rate of the stone. Siano et al. [8] studied how pulse duration affects the laser stone-cleaning process. Siano et al. [9] also experimentally determined the fluence thresholds corresponding to the various side effects in laser stone cleaning. LIBS (Laser-induced Breakdown Spectroscopy) was employed as an *in-situ* technique for monitoring the laser removal of the encrustation by Maravelaki et al. [10]. Rodriguez-Navarro et al. [11] found that the marble surface was roughened by the excessive laser pulses at supposedly safe fluence levels.

Both Maravelaki-Kalaitzaki et al. [12] and Marakis et al. [13] comparatively investigated the removal of different types of encrustation with different wavelengths. While the prominent self-limiting effect at 1064 nm is extremely beneficial in protecting the marble surface, the cleaned marble surface becomes severely yellowed. On the contrary, no severe yellowing occurs on the marble surface cleaned at 355 nm.

Klein et al. [14] and Potgieter-Vermaak et al. [15] both postulated that the yellowing at 1064 nm is due to residues of iron oxides on the marble surface detected by their experiments. However, they did not provide an explanation for the presence of these residues. Zafiropulos et al. [16] proposed that the discoloration is mainly an optical phenomenon. The dark particles are vaporized by the IR laser fluences below the cleaning threshold to generate voids in the encrustation. These voids make the light scattering different so that the color perception is altered towards yellow. Nevertheless, this argument lacks evidence.

In the present paper, the influence of the fluence levels on the surface color of marble cleaned with the 355nm laser pulses is examined. A mechanism leading to the discoloration of the marble surface is proposed based on an analysis of the thermochemical reactions possibly occurring in the encrustation during laser irradiation. A two-dimensional laser ablative cleaning model including the reaction heat of the thermochemical reactions is applied in simulating the temperature field generated by the laser irradiation. Then, the kinetics of the thermochemical reactions are used to verify their presence. The proposed mechanism is also used to explain the severe discoloration of marble cleaned with laser pulses at 1064nm.

3.2 Experiment conditions

A Q-switched Nd:YAG laser operating at 355 nm in TEM_{00} mode is used as the light source. The laser has a pulse duration of 50 ns, with a constant repetition rate at 1 kHz. The beam diameter is set at 100 μm and the pulse fluence is varied from 0.3 J/cm^2 to 3 J/cm^2 through adjusting the distance of the sample from the focusing lens. The sample is placed on the computer-controlled XYZ stage in open air, while the compressed air blows on the sample to prevent the ablation-formed plasma from touching the focusing lens during the experiment.

Italian white Carrara marble was selected as the investigated sample with dimensions 15mm×15mm×9mm. Its surface is honed to eliminate the obvious surface dents. The sample is thoroughly cleaned with methanol before making the encrustation. For numerical calculation of the laser produced temperature field, the encrustation is artificially made to better control the material property. The encrustation is a compound of 5% or 10% hematite (Fe_2O_3) powder, 20% graphite powder and 75% or 70% gypsum ($CaSO_4 \cdot 2H_2O$) (vol. %), mixed with distilled water, and smeared onto the marble with a brush [14]. The marble with the encrustation is then left for 72 hours in a storage box. On average, the encrustation thickness is approximately 120 microns.

3.3 Related thermochemical reactions

3.3.1 Thermal dehydration and decomposition of gypsum ($CaSO_4 \cdot 2H_2O$)

Gypsum ($CaSO_4 \cdot 2H_2O$, calcium sulfate dehydrate), the major ingredient in the encrustation, is a crystalline mineral that contains about 21% chemically combined water by weight. When gypsum is heated, two thermal dehydration reactions occur starting at

373 K and 573 K, respectively. These two reactions are described as:

$$CaSO_4 \cdot 2H_2O \rightarrow CaSO_4 \cdot \frac{1}{2} H_2O + \frac{3}{2} H_2O \text{ -17.2kJ/mol} \quad \textbf{(3.1)}$$

$$CaSO_4 \cdot \frac{1}{2} H_2O \rightarrow CaSO_4 + \frac{1}{2} H_2O \text{ -8.6 kJ/mol} \quad \textbf{(3.2)}$$

During these two reactions, water is released as steam with an absorbed energy of 81.7kJ/mol. Therefore, the total required energy in the dehydration of gypsum is 107.5 kJ/mol [17].

At temperatures above 1373K, $CaSO_4$ starts to decompose into calcium oxide (CaO) and sulfur dioxide (SO_2) according to the following equation [18]:

$$CaSO_4 \rightarrow CaO + SO_2 + \frac{1}{2} O_2 \text{ - 480 kJ/mol} \quad \textbf{(3.3)}$$

Calcite ($CaCO_3$) is dissociated into CaO and carbon dioxide (CO_2) starting at the temperature of 1173K to 1223K. The reaction is described as the follows [19]:

$$CaCO_3 \rightarrow CaO + CO_2 \text{ - 170 kJ/mol} \quad \textbf{(3.4)}$$

3.3.2 Hematite reduced by solid carbon

When a mixture of hematite (Fe_2O_3) and solid carbon is heated up to the certain temperature, the hematite is reduced into wustite (FeO) at an extremely high rate through two consecutive steps, namely hematite → magnetite (Fe_3O_4) → wustite, like $Fe_2O_3(s) + C(s) \rightarrow 2FeO(s) + CO$ [20]. Then, two coupled gas-solid reactions take place,

$$FeO + CO \rightarrow Fe + CO_2 \quad \textbf{(3.5)}$$

$$CO_2 + C \rightarrow 2CO \quad \textbf{(3.6)}$$

It is known that reaction **(3.5)** is catalyzed by the reduced metallic iron. More carbon monoxide (CO) produced in the vicinity of FeO increases the reduction rate of FeO.

If the molten hematite is reduced by solid carbon, the reduction rate rises rapidly. This is termed a smelting reduction. The possible reason is that the molten FeO can more easily contact carbon than solid FeO [21]. The weight volume of FeO is proportional to its reduction rate by solid carbon due to the increased interface area between FeO and carbon [22]. Also, CaO even at the low concentration can significantly expedite this reduction reaction [20]. The catalysis results from the enhanced formation rate of CO through the following redox process,

$$CaO + CO_2 \rightarrow CaO\cdot O + CO \quad \textbf{(3.7)}$$

$$CaO\cdot O + C \rightarrow CaO + CO \quad \textbf{(3.8)}$$

The thermochemical reactions introduced above are summarized in **Figure 3.1**. During the laser heating, these thermochemical reactions may occur in the encrustation when the encrustation temperature reaches the reaction-required temperature.

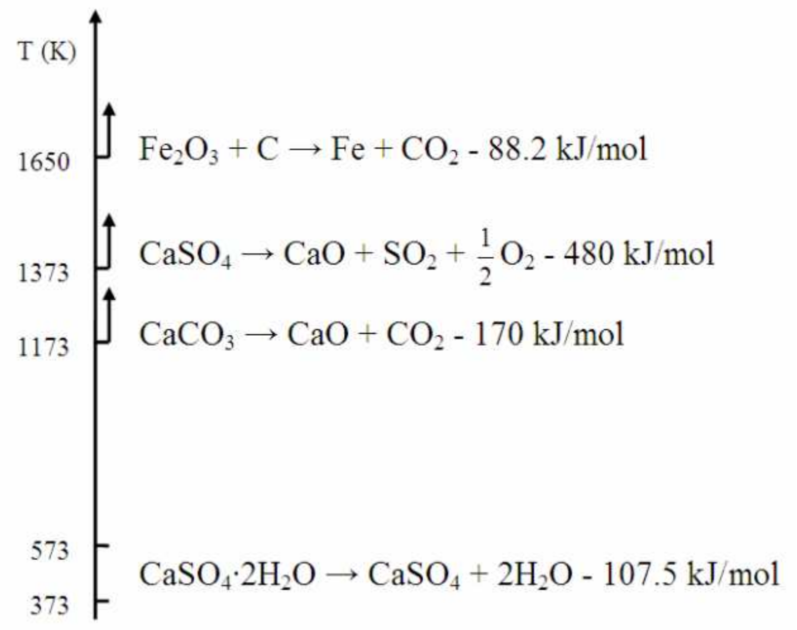

Figure 3.1 Schematic of thermochemical reactions taking place in the encrustation during laser heating.

3.4 Numerical simulation

Laser removal of the encrustation from the marble surface is based on laser ablation. Zhang and Yao [5] presented a two-dimensional laser ablative cleaning model, which considers the discontinuity across the Knudsen layer and Stephen Boundary at the interface. Through the enthalpy method, the temperature field can be simulated and the resulting phase interfaces identified. In the present paper, the heats of thermochemical reactions occurring in the encrustation are taken into account in the model. When the materials reach the required temperature for the thermochemical reaction, the corresponding reaction heat is integrated into the energy balance equation as:

$$\frac{\partial h}{\partial t}+\frac{\partial \Delta H}{\partial t}=\frac{\partial}{\partial x}(\alpha\frac{\partial h}{\partial x})+\frac{1}{r}\frac{\partial}{\partial r}(r\alpha\frac{\partial h}{\partial r}) \qquad \textbf{(3.9)}$$

where α is heat diffusivity, *x* and *r* are the coordinates along the thickness and radial direction. The enthalpy of the material (heat content of the material) *H* is expressed as $H = h + \Delta H$, where the sensible heat, $h = c_p T$ (c_p is specific heat, *T* is temperature), and ΔH is the latent heat of phase change ΔH_P or the reaction heat ΔH_T.

The reaction rate is assumed to follow the Arrhenius law, $k = k_0 \exp(-\frac{E}{RT})$, where k_0 is the frequency factor, *E* is the activation energy, *R* is the universal gas constant, *T* is the temperature. Concerning reactions **(3.1)** + **(3.2)** (dehydration), **(3.3)** and **(3.4)**, the corresponding incorporated reaction heats are calculated as $\Delta H_T = k\Delta H_{T0}$, where ΔH_{T0} is the reaction heat, k_0 is assumed to be 6.3×10^{24} [23], 1.32×10^{6} [18] and 6.45×10^{5} s^{-1} [19], and E is assumed to be 202, 212 and 187 kJ/mol, respectively. Since the mechanism of reaction **(3.5)** and **(3.6)** is complicated by the co-existence of Fe_2O_3, FeO and Fe, a volume-reaction model is applied in their kinetic analysis [24]. The FeO melting point of 1650 *K* is viewed as the separation point of the application ranges of two reaction rates. It is assumed that reaction rates follow the first-order kinetic equation,

$$\gamma_{Fe_2O_3} = -k_1[Fe_2O_3] \tag{3.10}$$

$$\gamma_{FeO(s)} = 2k_1[Fe_2O_3] - k_2[FeO(s)] \qquad (T_p \prec 1650K) \tag{3.11}$$

$$\gamma_{FeO(l)} = 2k_1[Fe_2O_3] - k_2[FeO(l)] \qquad (T_p \geq 1650K) \tag{3.12}$$

$$\gamma_{Fe(sorl)} = k_2[FeO(s)] + k_3[FeO(l)] \tag{3.13}$$

where k_{10}, k_{20}, and k_{30} are assumed to be 600, 1300 and 3400 s^{-1}, respectively. E_1, E_2, and E_3 are assumed to be 50.4, 75.6 and 88.2 kJ/mol, respectively [24].

Total reaction heat is computed in the following manner:

$$\Delta H_T = \Delta H_1 \cdot \gamma_{Fe_2O_3} + \Delta H_2 \cdot \gamma_{FeO(s)} + \Delta H_3 \cdot \gamma_{FeO(l)} \tag{3.14}$$

where ΔH_1, ΔH_2, ΔH_3 are the corresponding heats of reaction.

The material parameters of the encrustation are the mass-averaged value of every component. All of the material properties are from [25]. The calculation domain is chosen as three times the beam diameter in both the radial and depth direction. The absorptivities of the encrustation and marble at 355 nm are assumed to be 0.9 and 0.6, respectively [3].

3.5 Material characterization

The chromameter (Minolta CR-300) is employed to measure the surface color of the marble. In principle, light reflected from the measured surface is simultaneously collected by three photocells, each with spectral sensitivities equal to one of the color matching functions of a special CIE standard observer. The CR-300 has a measurement spot diameter of 8mm and use D56 standard xenon light to irradiate the surface. The color measurements are expressed in the perceptually uniform color space, CIE $L^*a^*b^*$ (CIELAB), shown in **Figure 3.2**. The L^* axis is known as the lightness ranging from 0 (black) to 100 (white). The a^* axis and b^* axis represent redness-greenness and yellowness-blueness, respectively. Total color difference ΔE_{ab}^* is defined as $\Delta E^*_{ab} = \sqrt{(\Delta L^*)^2 + (\Delta a^*)^2 + (\Delta b^*)^2}$, where $\Delta L^* = L^* - L^*_t$ describes the lightness change, $\Delta a^* = a^* - a^*_t$ and $\Delta b^* = b^* - b^*_t$ describe the chromaticity change, L^*_t , a^*_t , and b^*_t are values of reference white [26].

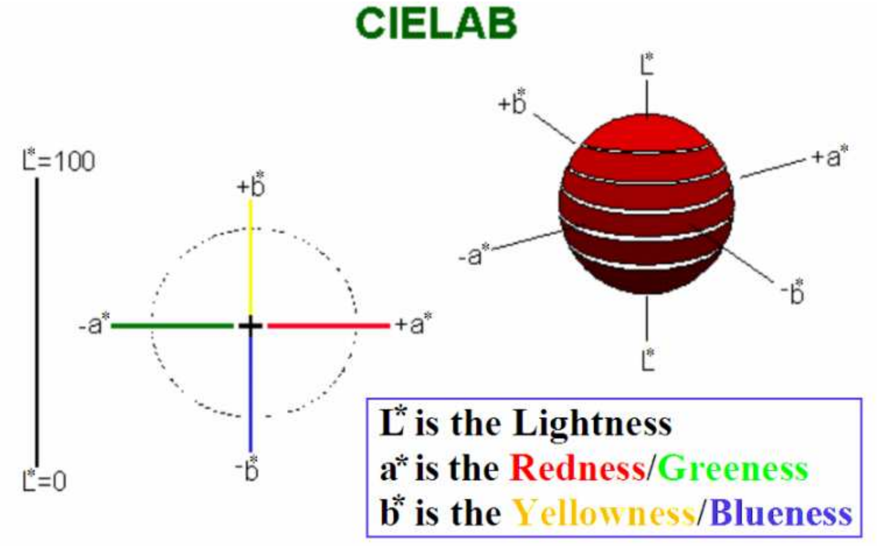

Figure 3.2 Schematic of a 1976 CIE-L*a*b* color system.

Surface enhanced Raman spectroscopy (SERS) is used to identify the chemical constituents of the marble surface [27]. When the surface is illuminated by a laser photon, a second photon is scattered. This photon differs in energy from the incipient photon by an energy difference in the levels of the surface constituents. The resulting Raman shift reveals structural information, as well as serving as an analytical tool to identify specific molecular adsorbents. The Raman signals from the surface may be greatly enhanced by application of silver colloidal nanoparticles on the surface. Silver colloidal nanoparticles were made as the same way in the chapter 2. Raman spectra are excited using a 514 nm CW Argon-ion laser (Spectra-Physics model 2020) at a power of approximately 20 mW. The scattered lines are collected at 90° with a Spex model 1401 double monochromator (resolution ca. 2 cm^{-1}) and detected by an ITT FW-130 photomultiplier (PM) tube with Raman 2005 (software package).

Scanning Electron Microscopy (JEOL) and Scanner (HP Scanjet 5100C) are employed to take the images of cleaned marble surface, respectively. In the case of SEM, the marble surface is coated with silver so that it is electrically conductive.

3.6 Results and discussions

3.6.1 Determination of fluence threshold

Successful cleaning is defined as the complete removal of the encrustastion without any change of the marble surface in the integrity, structure and color. To experimentally determine the fluence threshold, the sample is irradiated by a single pulse per location. The fluence is continuously increased. When the damage of the encrustation including 5% hematite or the marble is noticeable under the optical microscope, the corresponding fluence values are considered as the thresholds. The experimentally determined thresholds for the encrustation and the marble are 0.45 J/cm^2 and 2.5 J/cm^2, respectively.

In order to estimate the accuracy of the proposed numerical model, the fluence threshold is also determined with this model. At 50 ns, the fluence increasing the encrustation surface to the mass-averaged value of the graphite vaporization temperature, the decomposition temperature of hematite and gypsum, namely 2160 K, is considered as its threshold. Similarly, the fluence heating the marble surface to the decomposition temperature of calcite is the threshold for the marble. In **figure 3.3**, the Raman spectrum of the marble has four bands of $CaCO_3$ at 158, 285, 711 and 1084 cm^{-1} [28]. It is evident that the principal ingredient of the marble is $CaCO_3$.

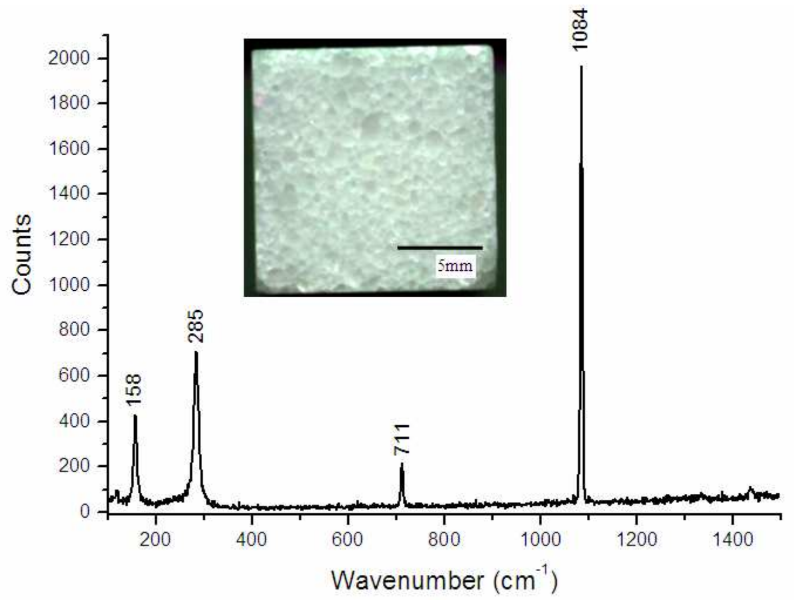

Figure 3.3 Raman spectrum and image of white carrara marble (Raman shifts are excited by the 514 nm laser).

The numerically determined thresholds are 0.3 J/cm^2 and 1.8 J/cm^2 for the encrustation and the marble, respectively. If the model does not include the thermochemical reaction heat, the determined threshold is 0.12 J/cm^2 and 0.42 J/cm^2 for the encrustation and the marble, respectively. The thresholds determined by the model with the reaction heat are more close to the experimental ones, which shows this model is accurate to some extent. The slight overestimate of the model in the ablation effect is possibly because that the heat taken away by the released gases produced in the thermochemical reactions is neglected in the model. Both the experimental and numerical results demonstrate that the threshold difference between the encrustation and the marble is large. This provides marble cleaning at 355 nm, which is self-limiting, thereby avoiding damage to the marble substrate.

3.6.2 Effect of fluence levels

3.6.2.1 Experiments

Under the multiple-pulse strategy, the applied laser fluence should be higher than the encrustation threshold of 0.45 J/cm^2 and lower than the marble threshold of 2.5 J/cm^2. Here, the laser fluence is chosen as 0.67 J/cm^2 and 1.3 J/cm^2, respectively. Considering the chromameter measurement spot diameter of 8 mm, a circular encrustation area with the diameter of 9 mm is removed. The laser pulses irradiate the encrustation along the circular orbits from the outside to the inside. The pulses have the overlapping rate of 50% to reduce the effect of the Gaussian beam on the irradiation results.

The samples with the encrustation containing 5% hematite are employed in the experiments. **Figure 3.4 (a)** and **(b)** are the scanned images of the marble cleaned by 8 pulses at 0.67 J/cm^2 and 5 pulses at 1.3 J/cm^2, respectively. The color measurements of the original and cleaned marble surface as well as the encrustation are listed in **Table 1**. In **Figure 3.4 (c)**, the color measurements are shown in the 1971 CIE L*a*b* color space. All of color data is the average of five independent measurements.

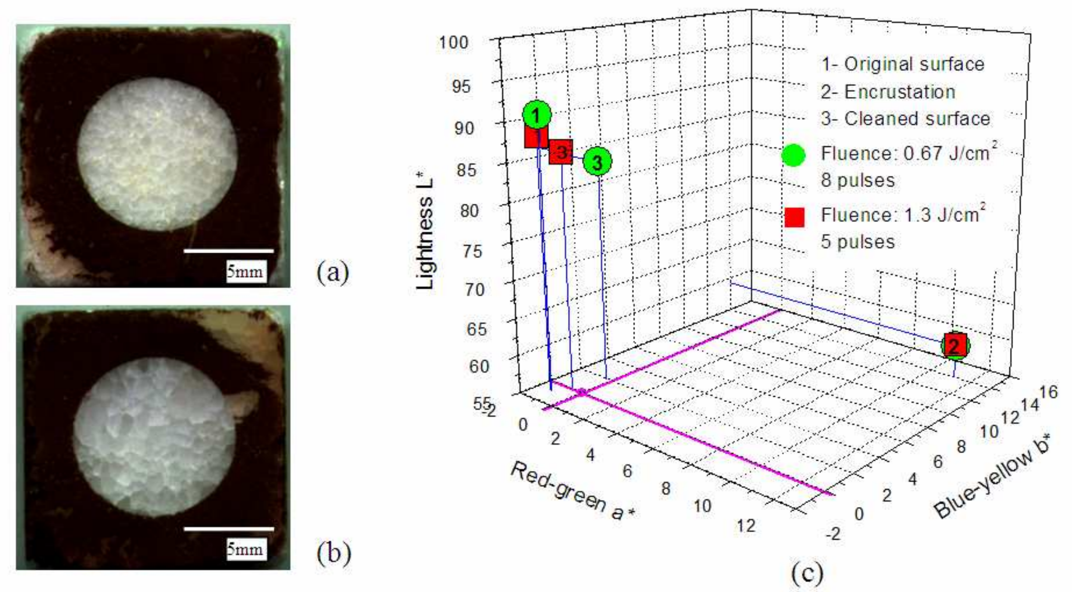

Figure 3.4 Images and color measurements of the marble surface before and after the removal of the encrustation with different fluence (beam radius: 50 μm, encrustation thickness: 120 μm, 5% hematite).

Table 3.1 Color measurements

	Original marble	Encrustation	Marble cleaned by 8 pulses at $F = 0.67$ J/cm^2	Original marble	Encrustation	Marble cleaned by 5 pulses at $F = 1.3$ J/cm^2
ΔL^*	90.8433	59.39	84.2767	88.2367	59.39	86.1133
Δa^*	−1.0333	11.2167	−0.20333	−1.19	11.2167	−0.58333
Δb^*	−0.94	13.9633	1.89333	−0.8967	13.9633	−0.0333

ΔL^*: Lightness; Δa^*: Red-Green; Δb^*: Blue-Yellow

Compared with the original marble surface, the lightness of the encrustation is much lower, which indicates the black appearance of the encrustation due to the graphite. The positive values of $\Delta a^*$and Δb^* denote the encrustation color is inclined to the redness and yellowness owing to the dark-brown hematite in the encrustation.

The lightnesses of both cleaned marble surfaces are very close to the original ones, which imply the removal of the encrustation. However, the lightness difference between the cleaned and the original surfaces is larger in the case of 0.67 J/cm^2. This reflects the encrustation may not be completely removed. At 1.3 J/cm^2, both of Δa^* and Δb^* are close to the original values and have the same sign. It can be concluded that there is no color variation. At 0.67 J/cm^2, Δa^* is close to the original one and has the same sign. However, Δb^* has a positive sign, which means the surface is becoming slightly yellowed. This phenomenon is referred to as the discoloration of the marble surface.

The Raman spectra of two cleaned surfaces are shown in **Figure 3.5**. The spectrum of the surface irradiated at 1.3 J/cm^2 only shows bands of $CaCO_3$ at 158, 285, 711, 1084 cm^{-1}. Yet, the spectrum of the surface irradiated at 0.67 J/cm^2 consists of bands of $CaCO_3$ as well as additional bands of Fe_2O_3 at 224 and 405 cm^{-1} [29]. The $CaCO_3$ bands in two spectra indicate the marble surfaces are exposed after the removal of the encrustation. The Fe_2O_3 bands reflect Fe_2O_3 still resides on the surface irradiated at 0.67 J/cm^2. Thus, it could be deduced that the presence of Fe_2O_3 is related to the surface discoloration. Very small amounts of Fe_2O_3 on the white calcite surface may result in a yellow shift [30]. The SEM pictures of these two cleaned marble surfaces are shown in **Figure 3.6**. Some particles are on the surface cleaned at 0.67 J/cm^2. The surface cleaned at 1.3 J/cm^2 is fairly clean.

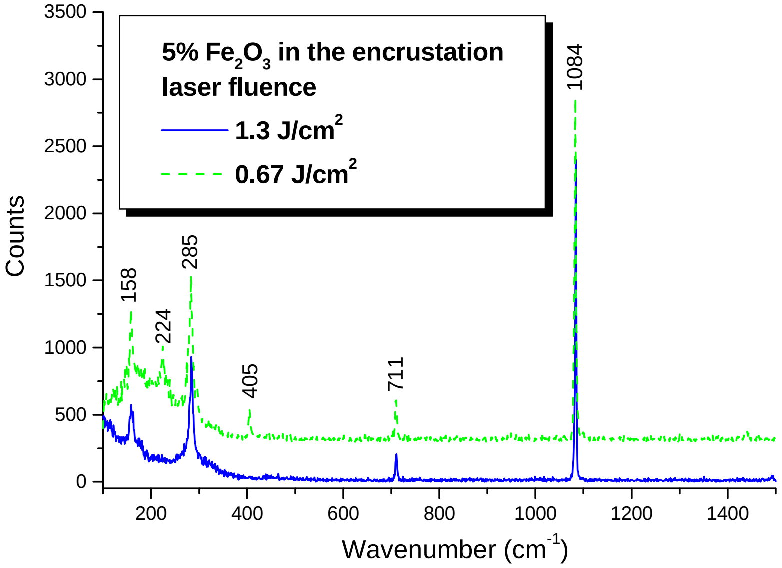

Figure 3.5 Raman spectrum of marble surface after the removal of the encrustation with different fluence levels (Raman shifts are excited by 514 nm laser at a power of 20 mW, the green dotted line has an upward shift of 300 for the clarity, beam radius: 50 µm, encrustation thickness: 120 µm, 5% hematite).

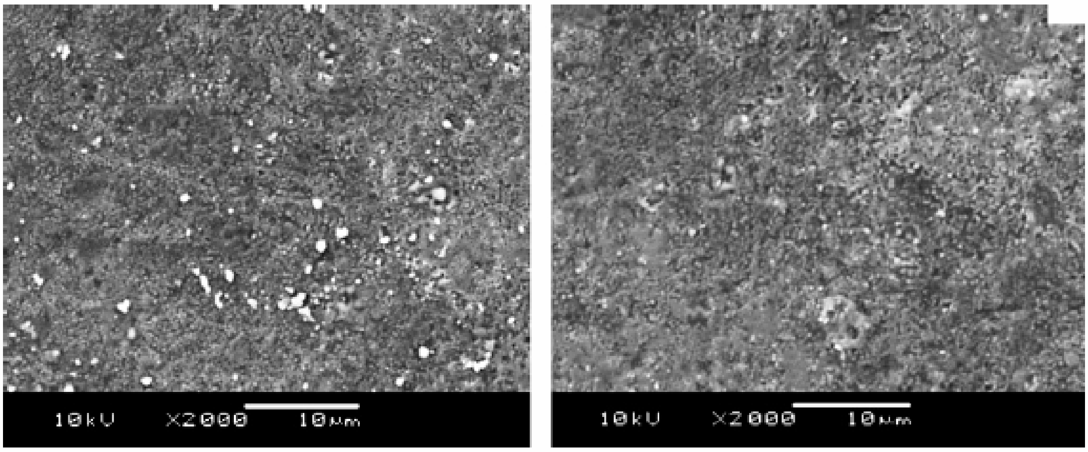

Figure 3.6 SEM images of marble surface after the removal of the encrustation with different fluence levels (a) 0.67 J/cm^2 (b) 1.3 J/cm^2 (beam radius: 50 µm, encrustation thickness: 120 µm, 5% hematite).

3.6.2.2 Analysis of the discoloration mechanism

3.6.2.2.1 The hematite reduced by the graphite

Figure 3.7 shows the simulated history of temperature distribution in the encrustation produced at 1.3 J/cm^2 and the temperature distribution at 50ns induced by the fluence of 0.67 J/cm^2. Fe_2O_3 and FeO in the grey area are in the molten state due to the temperature ranging between the melting point of Fe_2O_3 1818 K and the one of FeO 1650 K. Some graphite powders may contact the molten Fe_2O_3 and FeO because of their random distribution in the encrustation. Correspondingly, part of the molten iron oxides may be reduced by the graphite to produce iron at the very high reaction rate. As mentioned before, this reduction reaction can be considerably accelerated by CaO from the thermal dissociation of $CaSO_4$. In the case of 1.3 J/cm^2, the grey area emerges starting from 10 ns, and is enlarged with the time, which means the smelting reduction of iron oxides may take place during the entire 50 ns. At 0.67 J/cm^2, the grey area at 50 ns suggests the availability of the temperature required by this reaction.

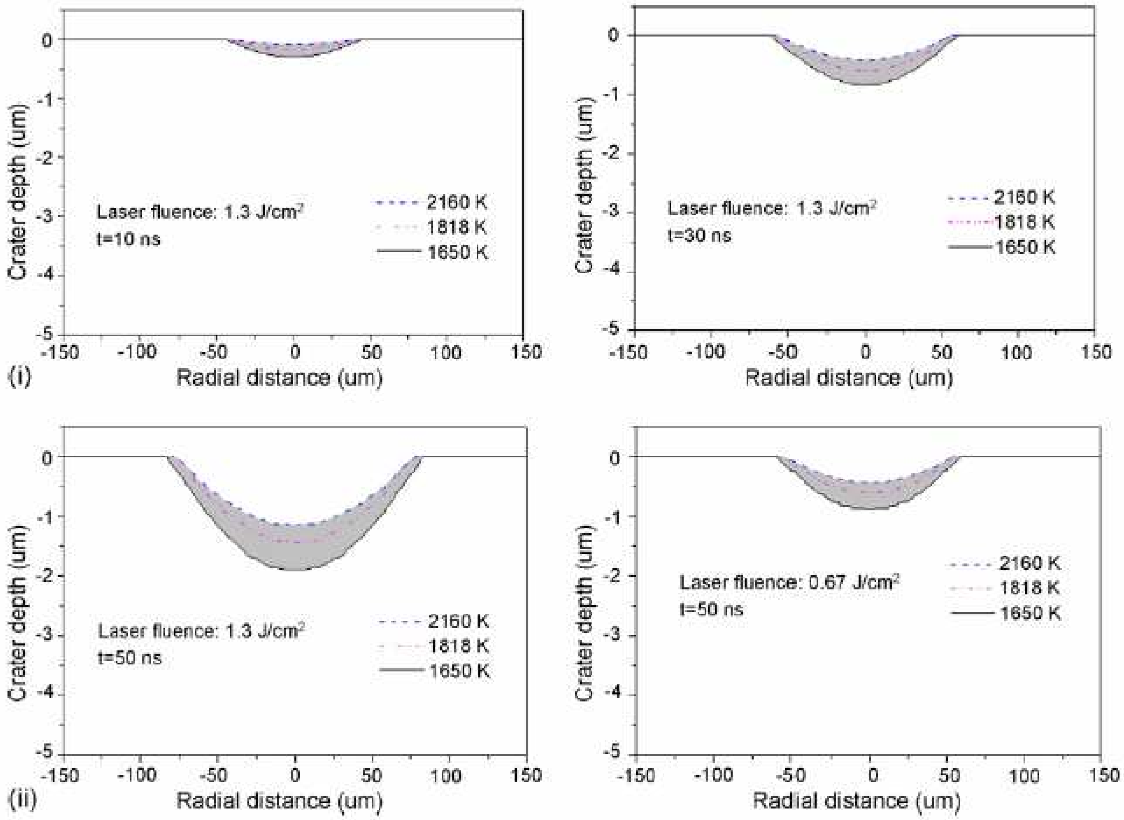

Figure 3.7 Simulated time history of temperature distribution in the encrustation produced by the pulse at 1.3 J/cm^2 and the temperature distribution produced by the pulse at 0.67 J/cm^2 at the end of pulse duration 50ns (beam radius: 50 μm, encrustation thickness: 120 μm, 5% hematite).

The simulated distribution of Fe, FeO and Fe_2O_3 at 50ns with the fluence of 0.67 J/cm^2 and 1.3 J/cm^2 is shown in **Figure 3.8**. Iron is generated in both cases. The higher the fluence is, the more metallic iron is produced. The evident reason is that the high temperature induced by the high fluence favors the reduction of iron oxides. It should be pointed out that very little hematite is reduced by graphite and the majority of the hematite is ablated by the laser pulse.

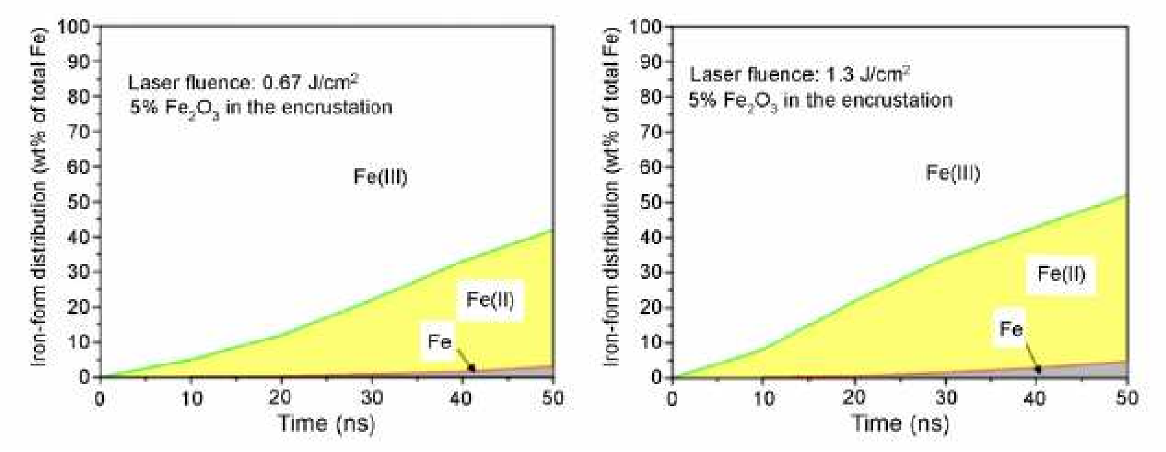

Figure 3.8 Simulated iron-form distribution at the end of pulse duration 50ns with two different fluence levels (a) 0.67 J/cm^2 (b) 1.3 J/cm^2 (beam radius: 50 μm, encrustation thickness: 120 μm, 5% hematite).

Figure 3.9 describes the temperature history at the bottom center of the crater generated by 3 pulses at 1.3 J/cm^2 and 6 pulses at 0.67 J/cm^2. In the case of 0.67 J/cm^2, iron oxides can be heated above 1000 K by three pulses, respectively. The longer reaction time of the solid iron oxides reduced by the graphite at the high temperature may result in the production of more iron. On the contrary, only one pulse is needed to heat the material above 1000 K in the case of 1.3 J/cm^2. Also, heat accumulation between two successive pulses is enhanced with the pulse number. After 3 pulses at 1.3 J/cm^2, the temperature is 1225 K; after 6 pulses at 0.67 J/cm^2, the temperature is 1300 K.

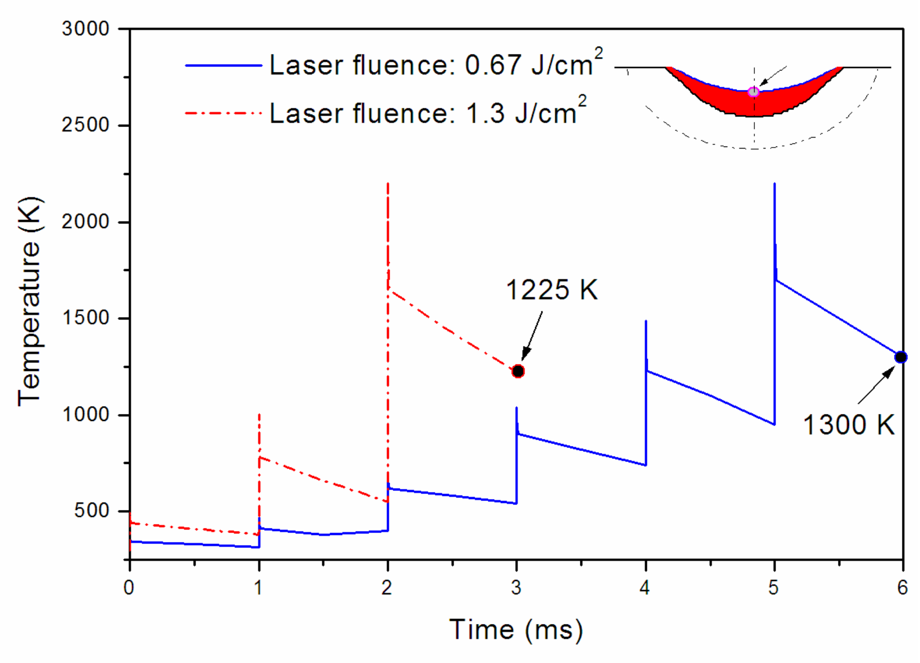

Figure 3.9 Simulated time history of temperature at the center of the final crater bottom irradiated by two different fluence levels (beam radius: 50 µm, encrustation thickness: 120 µm, 5% hematite).

3.6.2.2.2 The reduced metallic iron during laser irradiation

During the laser irradiation, the plasma formed impedes the air from interacting with the surface. The dissociation of the ablated hematite in the plasma will produce atomic oxygen [31]. However, oxygen has no solubility in liquid iron, preventing the production of iron oxide at this step [32]. Yet, Pereira et al. [33] experimentally found the appearance of a Fe_2O_3 layer at the iron surface after the irradiation of the XeCl laser. This means that the formation of Fe_2O_3 is due to the chemical reaction between iron and oxygen during the cooling stage. The chemically active iron reacts easily with the oxygen, especially at high temperatures. Since the formation enthalpy of iron oxide is small, iron oxides are produced very near the surface. The iron oxide forms a multilayer scale consisting of FeO, Fe_3O_4 and Fe_2O_3 from the iron bulk to the outermost [34]. Increases in the time that the iron is subjected to high temperatures can lead to increases in the production of iron species in a higher oxidation state, i.e., more Fe_2O_3 is formed.

The majority of iron produced by the current pulse may be taken away by the ablation flux during the next pulse, and the rest of the iron may interact with subsequent pulses. The following investigation focuses on the iron irradiated by the last pulse required by the complete removal of the encrustation, namely the 7th pulse at 0.67 J/cm^2 and the 4th pulse at 1.3 J/cm^2. It is assumed an independent iron particle is irradiated by a single pulse. The 2-D ablation model is employed to simulate its temperature distribution [35]. The absorptivity of iron at 355 nm is 0.6 [25]. Considering the heat accumulation, the initial temperature of iron is set as 1225 K and 1300 K, as shown in **Figure 3.9**, with the fluence of 1.3 J/cm^2 and 0.67 J/cm^2, respectively.

In the case of 1.3 J/cm^2, the temperature in a crater with a depth of 0.22 µm is simulated to be equal or higher than the vaporization point of iron 3134 K, which means the iron can be ablated. Though the actual thickness of the iron left on the marble is difficult to measure, it is certainly relatively minute. Thus, it can be assumed that all of the iron has been ablated. In the case of 0.67 J/cm^2, no iron is simultaneously heated up to 3134 K. The temperature above the melting point of iron (1811 K) is in the crater with the depth of 0.4 µm. Thus, the iron is assumed to be just melted.

The simulated temperature history of the points corresponding to the beam center at the different depths in the case of 0.67 J/cm^2 is shown in **Figure 3.10**. It is apparent that the peak temperature is generated at the end of the pulse. The iron could be oxidized during its cooling period of approximately 1s. Due to the high temperature in the very shallow iron, the iron oxides are in the form of Fe_2O_3. This newly formed Fe_2O_3 may stay at the porous structure of the marble surface because the molten iron may penetrate it during laser irradiation. As extra pulses are incident on the marble, the marble surface temperature is raised very slightly due to its low absorptivity. At this time, the hematite is heated mainly through heat conduction from the marble. Thus, the temperature of hematite may be much lower than its vaporization temperature.

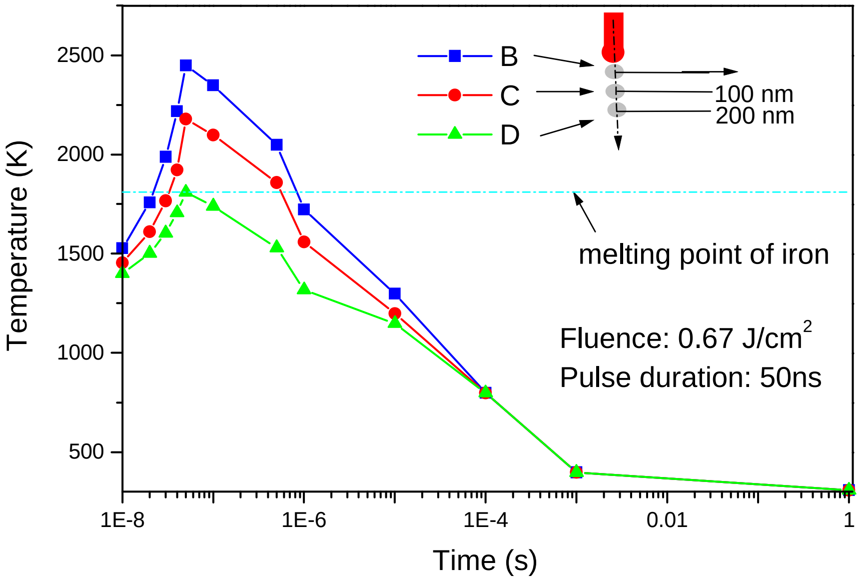

Figure 3.10 Simulated temperature history of the points on the iron corresponding to the beam center under the fluence of 0.67 J/cm^2 (beam radius: 50 μm, encrustation thickness: 120 μm, 5% hematite).

3.6.3 Effect of graphite

Without graphite, the encrustation consists of 5% hematite and 95% gypsum. The encrustation is irradiated by 8 pulses at 0.67 J/cm^2 and 5 pulses at 1.3 J/cm^2, respectively. The color of original and cleaned marble surfaces as well as the encrustation are measured and listed in **Table 3.2**, respectively.

Table 3.2 Color measurements

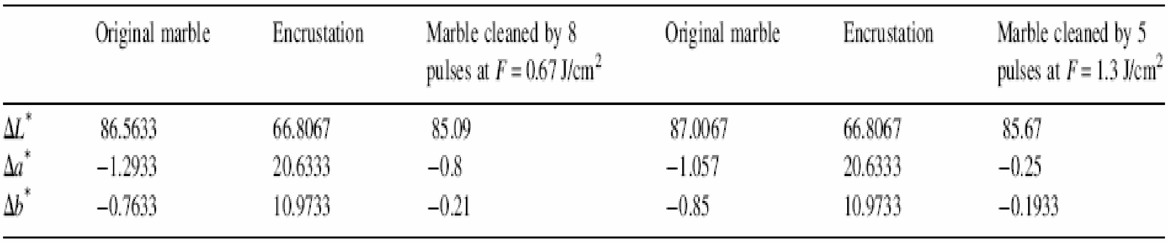

	Original marble	Encrustation	Marble cleaned by 8 pulses at $F = 0.67$ J/cm^2	Original marble	Encrustation	Marble cleaned by 5 pulses at $F = 1.3$ J/cm^2
ΔL^*	86.5633	66.8067	85.09	87.0067	66.8067	85.67
Δa^*	−1.2933	20.6333	−0.8	−1.057	20.6333	−0.25
Δb^*	−0.7633	10.9733	−0.21	−0.85	10.9733	−0.1933

ΔL^*: Lightness; Δa^*: Red-Green; Δb^*: Blue-Yellow

In the case of two fluence levels, the lightness of cleaned surface is very close to its corresponding original value. Meanwhile, two lightness differences between the cleaned and the original surface are almost equal. This probably means the encrustation is completely removed in both cases. Both of Δa^* and Δb^* values are also close to the original ones, and the signs are identical. So, it can be concluded that there is no color variation on the marble surface cleaned at 0.67 J/cm^2 and 1.3 J/cm^2. The Raman spectra measured on these two cleaned surfaces are shown in **Figure 3.11**.

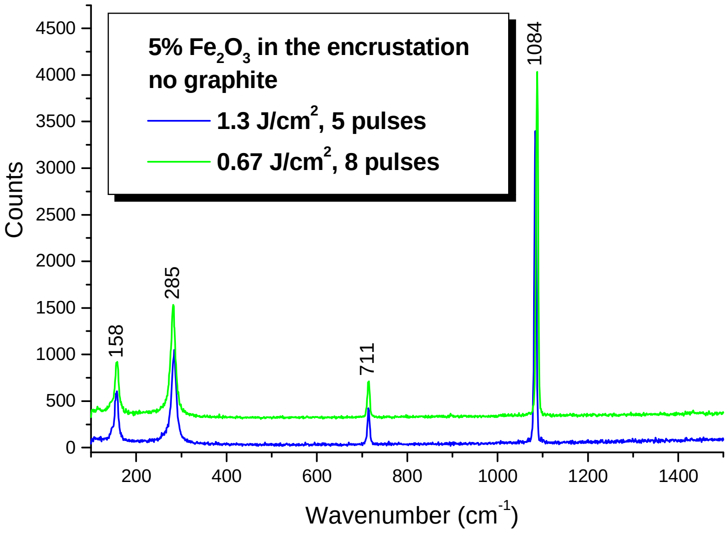

Figure 3.11 Raman spectrum of marble surface after the removal of the encrustation

without the graphite with different laser fluence levels (Raman shifts are exited by the 514 nm CW laser at a power of 20 mW, the upper green line has an upward shift of 300 for the clarity).

Both of the Raman spectra are characterized with the bands of $CaCO_3$ (158, 285, 711 and 1084 cm^{-1}). No Fe_2O_3 bands at 224 and 405 cm^{-1} appear. This indicates no Fe_2O_3 exists on two cleaned marble surfaces. Without the graphite, the hematite in the encrustation is just heated, and then ablated. This group of experiments indirectly verifies that hematite is reduced by the graphite to produce iron during laser irradiation.

3.6.4 Effect of volume weight of hematite

Marble samples are covered with the encrustation containing 10% hematite, 20% graphite, and 70% gypsum. These samples are also irradiated by 8 pulses at 0.67 J/cm^2 and 5 pulses at 1.3 J/cm^2, respectively. **Table 3.3** lists the color measurements of original and cleaned marble surfaces as well as the encrustation, respectively.

Table 3.3 Color measurements

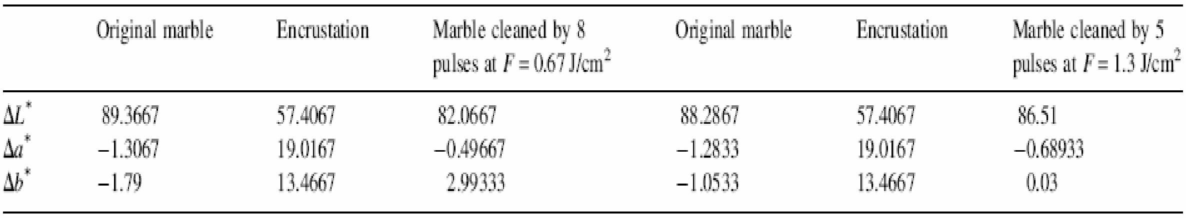

	Original marble	Encrustation	Marble cleaned by 8 pulses at $F = 0.67$ J/cm^2	Original marble	Encrustation	Marble cleaned by 5 pulses at $F = 1.3$ J/cm^2
ΔL^*	89.3667	57.4067	82.0667	88.2867	57.4067	86.51
Δa^*	−1.3067	19.0167	−0.49667	−1.2833	19.0167	−0.68933
Δb^*	−1.79	13.4667	2.99333	−1.0533	13.4667	0.03

ΔL^*: Lightness; Δa^*: Red-Green; Δb^*: Blue-Yellow

The color variation of the surfaces cleaned at 0.67 J/cm^2 and 1.3 J/cm^2 is similar to the corresponding color measurements shown in section 3.6.2.1. The only difference is the value of Δb^* after the irradiation of the pulse at 0.67 J/cm^2. It further shifts towards the positive direction, which means the yellowing of the cleaned surface is aggravated.

Figure 3.12 shows the Raman spectra collected from these two cleaned surfaces. Both samples have the $CaCO_3$ bands of 158, 285, 711 and 1084 cm^{-1}. Only the sample irradiated at 0.67 J/cm^2 shows the Fe_2O_3 bands of 224 and 405 cm^{-1}, which indicates the presence of Fe_2O_3 on the marble surface irradiated at 0.67 J/cm^2.

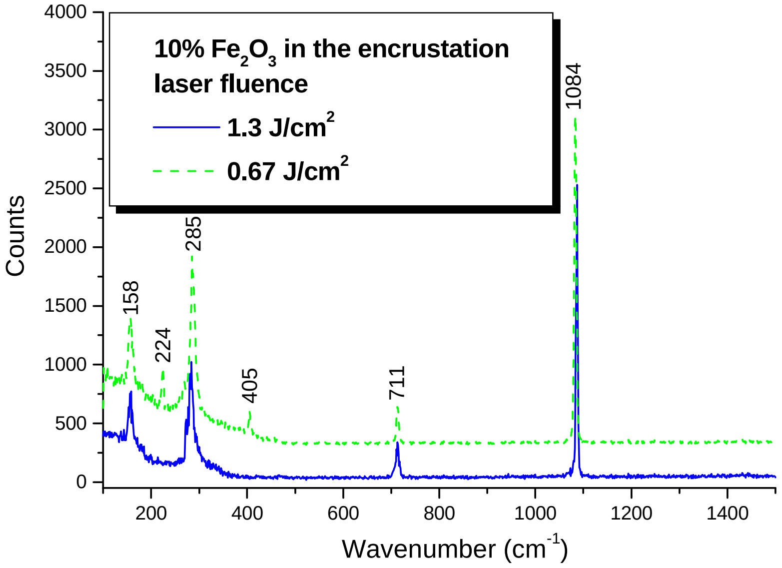

Figure 3.12 Raman spectrum of marble surface after the removal of the encrustation with 10% hematite with different laser fluence levels (Raman shifts are excited by the 514 nm cw laser at a power of 20 mW, the green dotted line has an upward shift of 300 for the clarity, beam radius: 50 μm, encrustation thickness: 120 μm, 10% hematite).

The increased yellowing shift is probably due to the high volume weight of hematite in the encrustation. Lee, et al. [22] found that the reduction rate of hematite by graphite rises with the weight of hematite owing to the augmentation of the interface area between hematite and graphite. Therefore, increased iron production results in an increase in the formation of iron oxides. Such experimental results indicate the occurrence of the thermochemical reaction to some extent.

3.6.5 Analysis of severely yellowing of marble at 1064 nm

In order to explain the severe yellowing of marble cleaned at 1064 nm with the proposed mechanism, the experimental parameters applied in Ref.14 are adopted in the following analysis. The artificial encrustation contains 20% graphite, 20% hematite, and 60% gypsum. The encrustation is removed by 10 or 20 pulses at 0.5 J/cm^2. The pulse duration is 7 ns, and the repetition rate is 2 Hz. In the simulation, the beam size is assumed to be 100 µm in diameter, and the encrustation thickness is 120 µm. The properties of the encrustation are recalculated based on the new ratio of the ingredients.

Figure 3.13 shows the simulated temperature distribution in the encrustation generated with a fluence of 0.5 J/cm^2 at 7 ns. The ablation temperature of this encrustation is assumed to be 2250 K. Clearly, the temperature in part of the encrustation is in the range from 1818 K (melting point of Fe_2O_3) to 1650 K (melting point of FeO). The smelting reduction of hematite by graphite may take place to form the iron in this area.

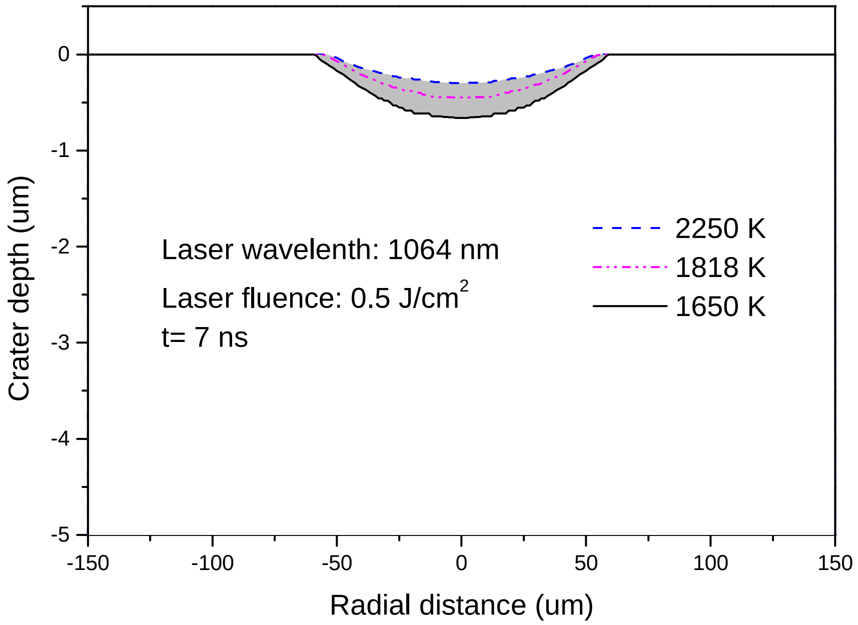

Figure 3.13 Simulated temperature distribution in the encrustation produced by a 1064 nm laser pulse with the fluence of 0.5 J/cm^2 at the end of pulse duration 7 ns (beam radius: 50 μm, encrustation thickness: 120 μm).

Whether iron can be ablated by the last applied pulse in the experiment is related to the final presence of iron on the surface. Therefore, an independent iron particle is assumed to be irradiated by the 10th pulse and the 20th pulse at 0.5 J/cm^2, respectively. The absorptivity of iron at 1064 nm is around 0.31 [25]. Similarly, the initial temperature of iron is numerically calculated to be 700 K and 1150 K in the case of the 10th pulse and the 20th pulse, respectively. The simulated temperature history of the point corresponding to the beam center at the iron surface is shown in **Figure 3.14**. In both cases, the peak temperature is lower than the vaporization temperature of iron 3134 K, which means iron can not be ablated, just melted. After the pulse is over, the iron requires almost one second to cool. Then, the oxygen can react with the high temperature iron to form iron oxides. Hence, the marble surface becomes yellowed. The severe yellowing at 1064 nm may result from the generation of more iron oxide. The marble absorptivity at 1064 nm is only 0.25 [3]. However, the marble absorptivity at 355 nm is slightly higher. The marble-absorbed heat may be helpful in increasing the temperature of the iron to its vaporization point, and hence reducing the amount of the remaining iron and then iron oxide in the case of 355 nm.

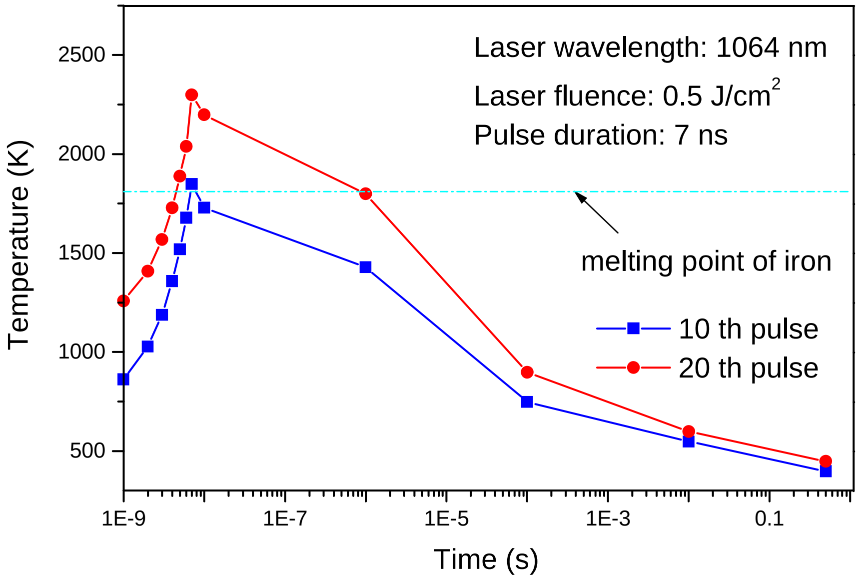

Figure 3.14 Simulated temperature history of the point on the iron corresponding to the beam center by the laser pulses at the wavelength of 1064nm (fluence: 0.5 J/cm^2, beam radius: 50 µm, encrustation thickness: 120 µm).

3.7 Conclusions

The fluence levels affect the surface color of marble after the removal of the encrustation by 355nm laser pulses. During laser irradiation, some hematite may be reduced by the graphite to produce iron. The iron may be ablated with the high fluence, and left on the marble surface with the low fluence. The iron oxides from the oxidation of the remaining iron may be responsible for the light discoloration of the marble surface cleaned with the low fluence. The laser-induced temperature field is calculated with a two-dimensional laser ablative cleaning model including the reaction heat to analyze the kinetics of the thermochemical reactions. With the low fluence, the removal of the encrustation without the graphite does not cause any discoloration to the marble, which indirectly verifies the occurrence of the reduction reaction of hematite. The higher the volume weight of hematite in the encrustation, the more yellow the marble surface becomes, which implies an increase in the volume weight of hematite increases the reduction rate of hematite. The severe discoloration of marble cleaned at 1064nm may be due to the inability to ablate the iron produced in the reduction of hematite.

Chapter 4

Mechanism and Prediction of Laser Wet Cleaning of Marble Encrustation

4.1 Introduction

Artifacts and buildings, made of natural stones such as marble, are inevitably and gradually covered by a thin layer of black encrustation. The black encrustation must be removed as it facilitates the degradation of the stone and also decreases the aesthetic value of the stone dramatically. At present, chemical cleaning and mechanical cleaning are widely used to remove the encrustation. Due to the possible environmental pollution and the strong dependence on the operator's techniques, the dominant status of chemical and mechanical cleaning is challenged by laser cleaning. Irradiated by the laser pulse, the encrustation can be ablated, but the stone remains intact after the removal of encrustation due to the large differences in their respective reflectivities. This characteristic, called "self-limiting", is very helpful in implementing safe and accurate stone cleaning.

Since John Asmus in 1971 first proposed to apply a pulsed laser in cleaning encrustations from marble, the effectiveness of Nd:YAG laser in the restoration of various stoneworks has been implemented by the massive investigations [1]. However, there are some disadvantages. Pulsed lasers have not succeeded in removing very thick encrustations. Cleaning efficiency is relatively low due to low ablation rates. The laser pulse induced elevated temperatures can lead to undesirable thermal side effects, such as red-shift and vitrification, on the cleaned surface [2]. In addition, the stone surface displays severe yellowing after the cleaning with a laser at 1064 nm [3], and even the 355 nm laser pulse at low fluence leads to the yellowing of the stone [4].

Many efforts have been made to investigate the particular contamination removed from microelectronic parts with pulsed lasers. As the dimension of microelectronic parts is constantly shrinking, their tolerance to particle size also decreases. Laser steam cleaning has shown great potential in cleaning submicron-sized particles as the generated cleaning force is much larger than in dry cleaning. Kim, *et al.,* in 2004 investigated the physical mechanism of laser steam cleaning. It was proven that the cleaning force comes from bubble nucleation in the superheated liquid [5]. Lu, *et al.* in 1998 proposed a model to calculate the cleaning force generated during the inertial-controlled bubble growth [6].

In this work, laser cleaning carried out right after a thin layer of suitable liquid is sprayed onto the encrustation is referred to as laser wet cleaning. A black encrustation approximately 500 µm thick was removed from limestone by a Q-switched Nd:YAG laser at 1064 nm with the assistance of distilled water. In the case of a thin encrustation approximately 50 µm thick on limestone, the cleaning rate with water was higher than that without water [7]. The application of water prevented the laser cleaned pliocene sandstone from any thermal side effect. It was speculated that the water significantly cooled down the irradiated volume because its specific heat is five times higher than sandstone [2]. The measured reflectivity of wet encrustation on sandstone was lower than that of dry encrustation. This may contribute to the increase in cleaning rate with water [8].

Cooper, *et al.* in 1995 also found that cleaning efficiency was enhanced in laser wet cleaning of limestone in terms of the removed encrustation area due to water penetration into the porous encrustation. During laser irradiation, the water in the pore would be explosively vaporized by the heat transferred from the encrustation, and generate large transitive forces exerting on particles within the encrustation. These forces were sufficient to loosen the encrustation, which was very beneficial to laser cleaning [9]. However, the working mechanism of water in laser cleaning is still not very clear, and no theoretical analysis has been performed.

In this work the mechanism of laser wet cleaning is proposed. Coupled heat and (moisture) mass transport within the laser irradiated porous encrustation is used to model laser wet cleaning. The corresponding governing equations are numerically solved with finite element methods to calculate the distribution of temperature, pressure and water volumetric fraction in the encrustation. The effects of distilled water, ethanol and acetone on the cleaning efficiency of the encrustation from marble are compared experimentally and numerically. There is some agreement between experimental and numerical values of the cleaning efficiency. Also, the color of marble surfaces cleaned by laser wet cleaning is analyzed.

4.2 Mechanism of Laser Wet Cleaning

In laser wet cleaning, the thin layer of liquid is sprayed onto the porous encrustation just prior to laser irradiation. Liquid penetrates and fills in the minute pores of the encrustation. When laser irradiation starts, both the encrustation and liquid are heated. Once the temperature reaches the boiling point of liquid, it is vaporized immediately. Since liquid is vaporized at a rate much higher than its migration rate, vapor pressure is built up in the pore. If the pressure is larger than the reduced tensile strength of the encrustation at high temperature, the encrustation may be stripped away locally. The stripping in turn will accelerate the heat transfer in the encrustation and result in the new establishment of the pore pressure at the deeper level. Meanwhile, the ablation still plays a role in the removal of encrustation.

4.2.1 Mathematic Modeling

During laser wet cleaning, laser pulses induce the evaporation of liquid and the subsequent built-up pressure in the pore. Driven by the pressure gradient, the liquid and the vapor are convected among the encrustation pores, which affect the heat transfer in the encrustation. Gypsum ($CaSO_4 \cdot 2H_2O$), the major encrustation ingredient, contains 21% chemically bound water by weight. Chemically bound water is released into the pore at 373 K and 573 K, respectively [10]. The absorbed laser heat is partly transferred into the encrustation by the liquid, vapor and encrustation together, partly absorbed by the evaporation of liquid, and partly consumed by the gypsum dehydration. Accordingly, coupled heat transfer and mass transport determines the temperature and pressure distribution within the encrustation.

Coupled heat and mass transport in the porous encrustation is based on the averaging of the quantities over a representative elementary volume (REV) [11]. The volumetric fraction of each phase composing a REV with volume V is defined as

$$\varepsilon_i = \frac{V_i}{V}, i = s, l, g \qquad \textbf{(4.1)}$$

where the subscripts s, l, and g indicate solid, liquid, and gas, V_i is the phase i volume. The sum of the volumetric fractions of three phases is equal to 1. It is assumed that the porous encrustation is full of liquid before the irradiation. The encrustation porosity ε is calculated as $\varepsilon = \varepsilon_l + \varepsilon_g$ and $\varepsilon_s = 1 - \varepsilon$.

The following assumptions are applied: a) The liquid is incompressible, ρ_l = constant. b) Compared to the gas, the mobility of the liquid is negligible [12]. c) No dry air stays in the pore. d) The vapor phase is only liquid vapor and the vapor is an ideal gas. e) The encrustation is homogeneous and isotropic. f) Local thermodynamic equilibrium is achieved. g) Except dehydration of the gypsum, no other thermochemical reactions occur.

The mass conservation equation of gas is

$$\frac{\partial}{\partial t}(\rho_g \varepsilon_g) = -\nabla \cdot (\rho_g V_g) + \Gamma \tag{4.2}$$

where V_g is the gas velocity determined with Darcy's law as follows,

$$V = -\nabla \cdot (\frac{K}{\nu} P) \tag{4.3}$$

where K and v is the permeability and dynamic viscosity of the vapor, and P is the pore pressure. Vapor density ρ_g is calculated with the Dalton equation, $\rho_g = {MP}/{RT}$, where R is universal gas constant, M is molar weight of vapor, and T is temperature. Γ is the evaporation rate of liquid.

Based on the enthalpy balance, the heat conduction and convection in the encrustation is governed by

$$\rho C_p \frac{\partial T}{\partial t} + \rho_g \varepsilon_g C_{pg} V \nabla T = \nabla \cdot (k \nabla T) \tag{4.4}$$

where t is time, and ρC_p is the effective heat capacity for the porous encrustation, calculated as $\rho C_p = (1-\varepsilon)\rho_s (C_{ps} + E\Delta h_d) + \varepsilon_l \rho_l (C_{pl} + F\Delta h) + \varepsilon_g \rho_g (C_{pg} + F\Delta h)$, where ρ_i and C_{pi} are density and specific heat of the corresponding phases, respectively [13]. Δh_d and Δh are the reaction heat of gypsum dehydration and the latent heat of the liquid vaporization, respectively. E and F are the derivative of solid and liquid phase volumetric fraction variation with temperature, respectively. The effective thermal conductivity for the porous encrustation k is defined as $k = (1-\varepsilon)k_s + \varepsilon_l k_l + \varepsilon_g k_g$ [14].

Only if the evaporation rate of liquid Γ is known, temperature, pore pressure and liquid volumetric fraction can be solved from equation **(4.2)** and **(4.4)**. In most coupled heat and mass transport models, a set of sorption isotherms is adopted to describe the dependence of water evaporation on temperature and pressure [12, 15, 16]. The accurate sorption isotherms are rather difficult to measure. Therefore, the evaporation rate of liquid is assumed to be related to the ratio of the vapor pressure to the saturated pressure at the corresponding temperature in some models [17, 18]. However, such a definition makes the accuracy of evaporation rate heavily reliant on the estimated evaporation rate constant. In this work, considering the laser pulse to be strongly instantaneous, the vapor volumetric faction is defined as

$$\varepsilon_g = \varepsilon U(T - T_{trans}, \Delta T) \tag{4.5}$$

where U is a step function whose value is zero at $T \le T_{trans} - \Delta T$, is equal to 1 at $T \ge T_{trans} + \Delta T$, and is uniformly distributed in the range from T-T_{trans} to T+T_{trans} [19]. Therefore, one obtains $\varepsilon_l = \varepsilon - \varepsilon_g$ and $F = {U(T - T_{trans}, \Delta T)}/{dT}$.

The encrustation porosity ε varies with the dehydration of gypsum, as

$$\varepsilon = \varepsilon_0 + \frac{\rho_{water}\delta_{sw}}{\rho_s} \tag{4.6}$$

where ε_0 is initial porosity, the effective density of water ρ_{water} is 21% of water density, δ_{sw} is the released water fraction, defined as $\delta_{sw} = \xi U(T - T_{trans}, \Delta T)$, where U is also a step function, coefficient ζ is equal to 0.75 and 0.25 at T_{trans} of 373 K and 573 K, respectively. The encrustation density ρ_s is equal to $\rho_s = \rho_{s0} - \rho_{water}\delta_{sw}$, where ρ_{s0} is the initial encrustation density.

The initial conditions are assumed to be $T = 300K$, $P = 101325Pa = 1atm$, $\varepsilon_l = \varepsilon$, and $\varepsilon_g = 0$. On the laser-irradiated surface, the boundary condition is specified as $-K\nabla T \cdot \vec{n} = I + h(T - T_\infty)$, $P = 101325Pa = 1atm$, $\varepsilon_l = 0$ and $\varepsilon_g = \varepsilon$, where $\vec{n}$ is the outward unit vector of the surface, the heat transfer coefficient h is $h = h_c + \sigma e(T + T_\infty)(T^2 + T_\infty^2)$, h_c is the convective heat transfer coefficient, σ is the Stefan-Boltzmann constant and e is the emissivity, T_∞ is the environment temperature of 300 K. I is the absorbed laser fluence, calculated as $I = \alpha I_0 \exp(-{r^2}/{b^2})$, where α is the surface absorptivity, I_0 is the incident fluence, b is the beam radius, r is the distance of the irradiated point to the beam center located at the symmetrical axis. On the non-laser-irradiated surface, the boundary conditions are applied, T = 300 K, $P = 101325Pa = 1atm$, $\varepsilon_l = 0$ and $\varepsilon_g = \varepsilon$.

4.2.2 Numerical Analysis

The coupled PDE equations **(4.2)** and **(4.4)** with boundary and initial conditions are solved through finite element methods. FEMLAB 3.2 software is used. A two-dimensional axial symmetrical model with the dimension of 200µm×120µm is established. The mapped mesh with two-directional bias is created in the model, shown in **Figure 4.1**. The application modes of transient conduction and convection, as well as Darcy’s law in chemical engineering module are adopted.

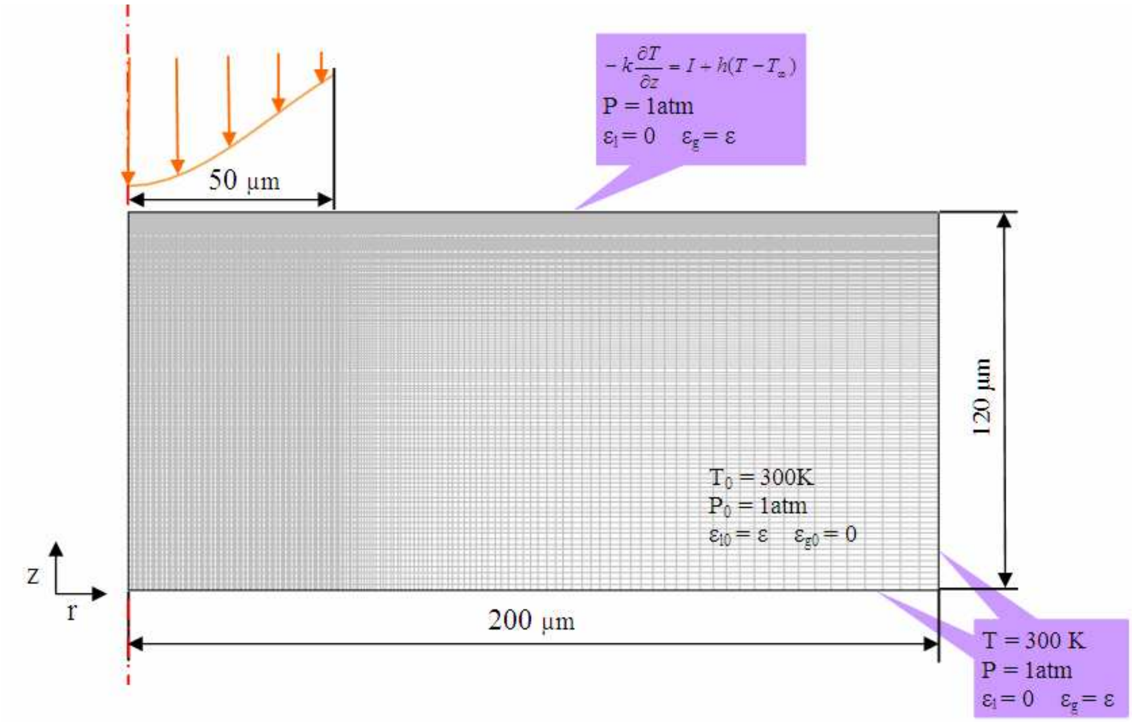

Figure 4.1 Schematic of the established model for laser wet cleaning.

In the model, a smoothed Heavyside function with a continuous second derivative, flc2hs, is chosen as the step function U. In the case of vaporized liquid (vapor), T_{trans} are set as 423 K, 401 K and 379 K for water, ethanol and acetone, respectively, and ΔT is 50 K. It is assumed that the water vaporizes starting from 373 K and all of water is vaporized at 473 K well below the critical point of water, 647K, because laser heating is extremely strong and fast. Similarly, the evaporation of ethanol and acetone is assumed to take place within the range from 351 K to 451 K and from 329 K to 429 K, respectively. Concerning gypsum dehydration, T_{trans} is set as 398 K and 598 K for two dehydration reactions, respectively, and, ΔT is 25 K.

Due to the constraint of the software, the laser-ablated part cannot be removed from the calculation domain. To decrease its effect on the calculation results, the thermal conductivity in the ablated element is assumed to be 5000 $Wm^{-1}K^{-1}$ once this element temperature is larger than the evaporation point.

All thermodynamic data of liquids comes from Ref. 19. The specific heat and dynamic viscosity of ethanol and acetone vapor are calculated by the method of Joback and the method of Chung, respectively [19]. In Ref. 20, the permeability of unfractured metamorphic rock ranges from 10^{-18} to 10^{-20}. Marble belongs to metamorphic rock. However, the marble encrustation is mainly constituted by softer and water-soluble gypsum, so the porosity of encrustation becomes larger. The permeability of the encrustation is assumed to decrease to 1×10^{-12}.

4.3 Experimental Conditions and Material Characterizations

The studied sample is Italian white Carrara marble with a honed surface. The sample is a cubic 15mm long, 15mm wide and 9mm thick. With the concern of numerical calculation accuracy, the marble is covered with the artificial encrustation, a compound of 5% hematite (Fe_2O_3) powder, 20% graphite powder and 75% gypsum (vol. %). The average encrustation thickness is approximately 120 microns. The formation method of the encrustation is introduced in details in Ref. 4.

Laser wet cleaning is performed with a Q-switched Nd:YAG laser at 355 nm in open air. The pulse duration is 50 ns. Other technical specifications for the laser are given in Ref. 4. All cleaning experiments were conducted with a laser beam with the diameter of 100 μm. A thin layer of liquid is sprayed onto the encrustation every 2 seconds to assure the encrustation is wet. The compressed air is always blowing onto the focusing lens during cleaning. Thus, the focusing lens is protected from the attachment of ablated particles, and the wet encrustation cannot be blown dry.

The SEM image of the encrustation presented in **Figure4.2** reveals the artificial encrustation is a porous structure. Porosity measurement is based on Archimedes' principle. The mixture including the same ingredients as the artificial encrustation is brushed onto the bottom of a 60 mm dish layer by layer, until reaching the thickness of 2.5 mm. This dish with the sample is weighed with a digital balance. Distilled water is then poured onto the sample surface very slowly to make sure the water fills in all the fine pores in the sample. The dish with the sample full of water is weighed again. Since the density of water is close to 1 kg/m^3, the ratio of the weight difference to the known sample volume is equal to the porosity of the sample.

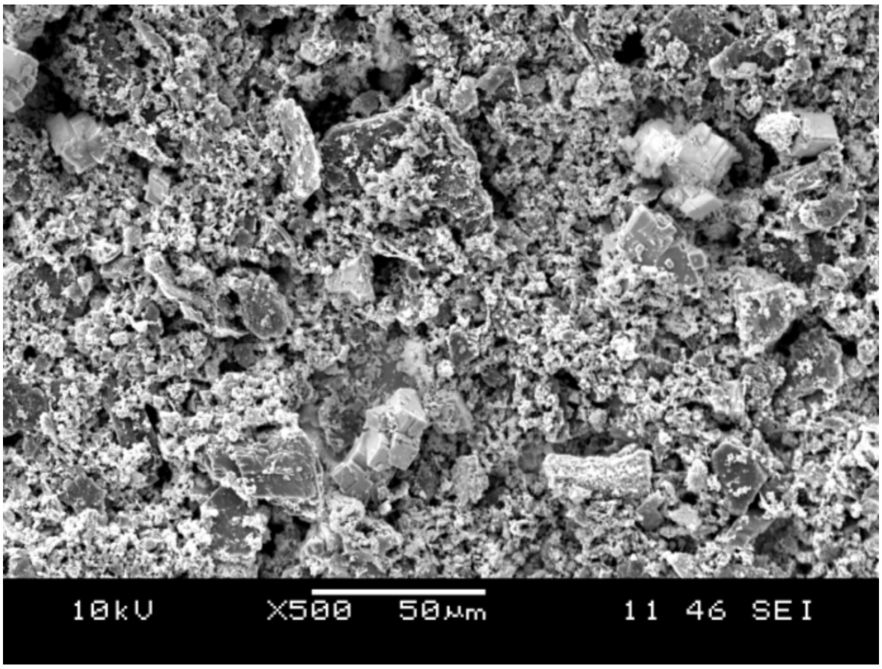

Figure 4.2 SEM image of the artificial encrustation on marble.

A chromameter (Minolta CR-300) and surface enhanced Raman spectroscopy are employed to measure the surface color and constituents. Their detailed introductions are in Ref. 4. SEM is used to take the image for the encrustation coated with silver.

4.4 Results and Discussions

4.4.1 Effect of distilled water on the cleaning efficiency

4.4.1.1Experiments

In the present work, the cleaning efficiency is denoted as the weight of the encrustation removed by one single pulse. To increase the weight variation of the cleaned sample between pre- and post-laser cleaning, a thin layer of encrustation in two circular areas with the diameter of 5 mm is removed. The laser pulses irradiate the encrustation along the circular orbits from the outside to the inside. The pulses have an overlapping rate of 50% to reduce the effect of the Gaussian beam. At the specified beam center locations, only one single pulse is deposited onto the encrustation. After two circular areas are irradiated once, the samples are weighed and compared with the initial weights. The sample weight difference divided by the number of deposited pulses, namely 16002, is equal to the ablated encrustation weight by one single pulse. In laser wet cleaning, the cleaned samples are not weighed after being dried.

Considering the ablation thresholds of encrustation and marble at 355 nm, 0.45 J/cm^2 and 2.5 J/cm^2, respectively [4], laser fluences of 0.49, 0.67, 0.95, 1.3, and 1.45 J/cm^2 are applied to ablate the encrustation without or with distilled water. The corresponding ablated encrustation weights by one single pulse are compared in **Figure 4.3**.

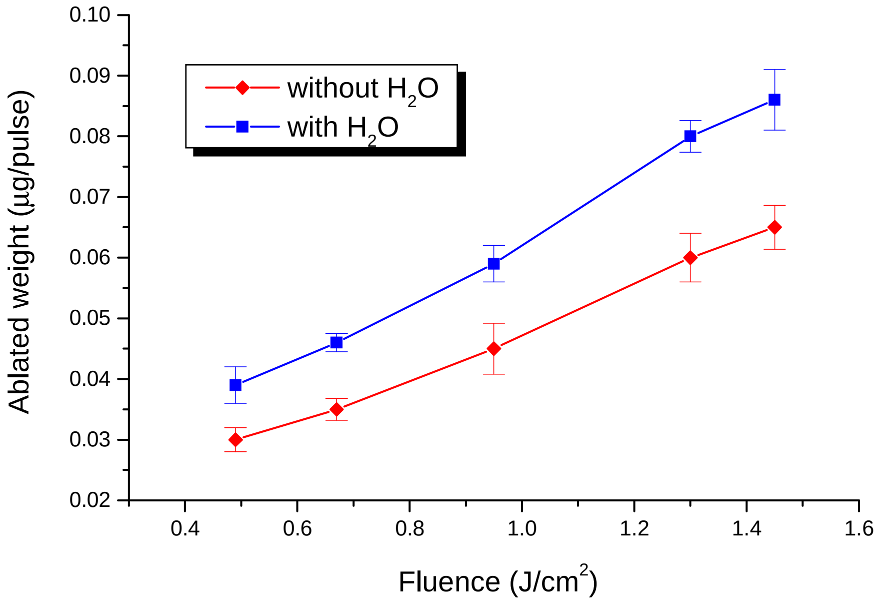

Figure 4.3 Comparison of the ablated encrustation weight by one single pulse at different fluence levels without and with distilled water.

Obviously, the use of water enhances the cleaning efficiency at every fluence level. White paper is put around the work stage during experiments to collect the encrustation debris. Some debris shown in **Figure 4.4** ranges approximately from 100 to 200 µm. This rather large debris is most likely produced by the encrustation stripping due to the vapor pressure.

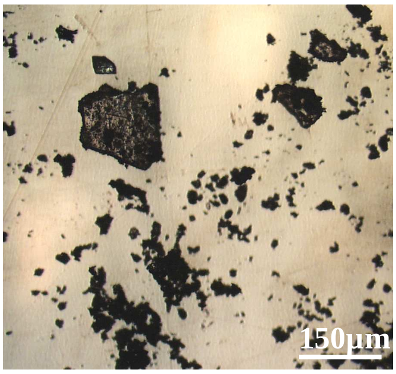

Figure 4.4 Images of debris collected during laser wet cleaning experiment.

In addition, **Figure 4.3** indicates the increase in cleaning efficiency with the distilled water as the fluence level increases. The possible reason is that the high fluence leads to high temperature and much stronger pressure. Moreover, the water in the deeper pores can be heated by the high fluence, so the vapor pressure may be established there as well.

4.4.1.2 Simulated distribution of temperature, pressure and water volumetric fraction within the irradiated encrustation

Assume that one single pulse at different fluence irradiates the encrustation. On average, the measured porosity of the encrustation is approximately 0.475. **Figure 4.5** shows the surface contours of temperature, water volumetric fraction and pressure at 50 ns produced by the pulse at 0.67 J/cm^2 in the partial irradiated encrustation (10 µm × 98 µm). In the temperature contour, the red arrows denote the total heat flux. Two isotherm lines correspond to 2160 K and 373 K, respectively. The isotherm line of 2160 K is at the very shallow location, which means very little of the encrustation is thermally ablated. The isotherm line of 373 K indicates the water in the pores about 2.5 µm below the irradiated surface starts to vaporize. The distribution of water volumetric fraction agrees with the temperature contour. At temperatures below 373 K, water fills in the pore, and the water volumetric fraction equals to the porosity of 0.475. At temperature above 373 k, all of water is vaporized in the majority of the area. The evaporation only exists in the very small area.

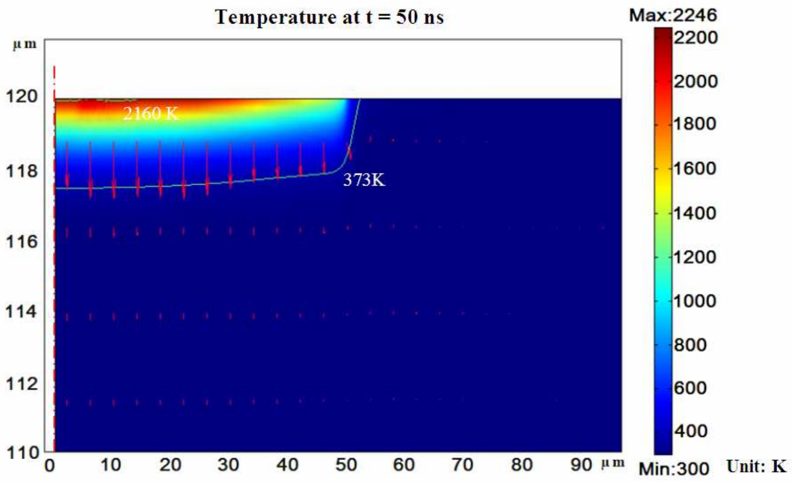
Temperature at t = 50 ns
μm
120
118
116
114
112
110
0
10
20
30
40
50
60
70
80
90 μm
2160 K
373K
Max:2246
2200
2000
1800
1600
1400
1200
1000
800
600
400
Min:300
Unit: K

(a)

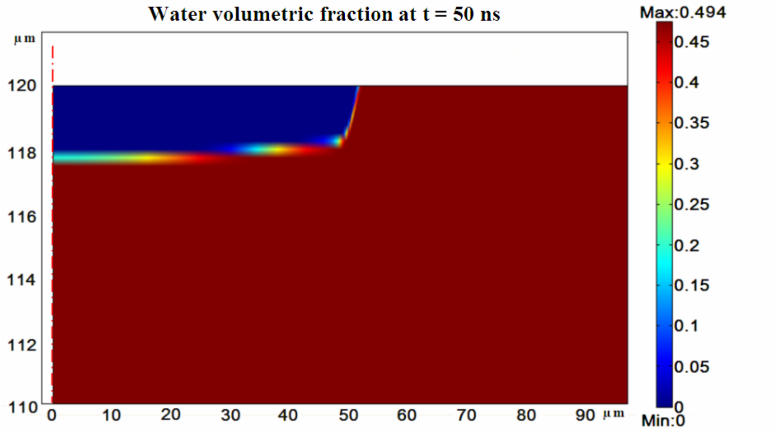
Water volumetric fraction at t = 50 ns
μm
120
118
116
114
112
110
0
10
20
30
40
50
60
70
80
90 μm
Max:0.494
0.45
0.4
0.35
0.3
0.25
0.2
0.15
0.1
0.05
0
Min:0

(b)

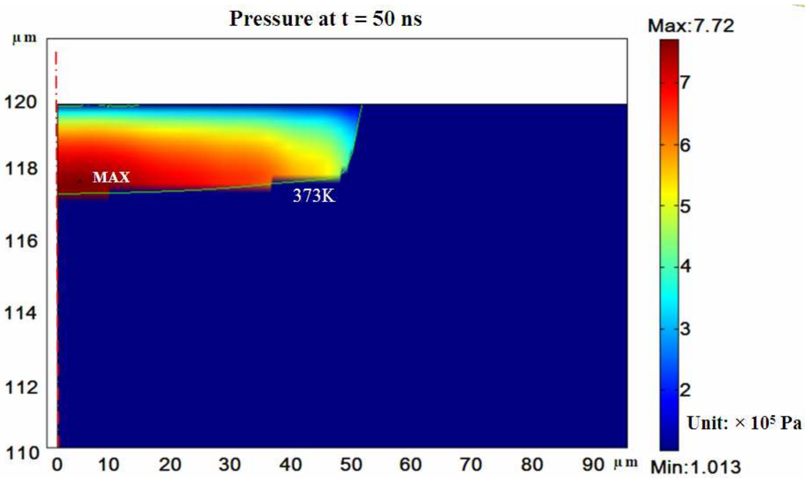
Pressure at t = 50 ns
μm
120
118
116
114
112
110
0
10
20
30
40
50
60
70
80
90 μm
MAX
373K
Max:7.72
7
6
5
4
3
2
Unit: × 10⁵ Pa
Min:1.013

(c)

Figure 4.5 Surface contours of (a) temperature with total heat flux, (b) water volumetric fraction and (c) pressure at 50 ns produced by the pulse at 0.67 J/cm^2 in the partial encrustation (10 µm × 98 µm).

The pressure contour shows the pressure is built up in the area at temperature above 373 k, encircled by the isotherm line of 373 K. In the area without water vaporization, the pressure is still equal to one atmosphere. The maximal pressure is marked. Obviously, its location is very near the start line of water vaporization. The pressure gradually decreases from the deep to the shallow area, which drives the water vapor to flow towards the encrustation surface and escape into the air. In addition, the maximal pressure approaches over 7.7 atm. Since the encrustation is artificially made, its tensile strength is assumed to be very low, approximately 3-4 atmosphere. Accordingly, the maximal pressure may be large enough to spall the encrustation off.

The time history of temperature, pressure and water volumetric fraction at the point with the maximal pressure at 50 ns is shown in **Figure 4.6**. In the first 20 seconds, the absorbed laser heat is not transferred to this point, and has a negligible effect on its temperature. This point is heated within the following 30 seconds of the pulse duration. However, after 50 ns, its temperature continues to rise due to the heat transferred from the top area with high temperature. Below 373 K, the water volumetric fraction is equal to the porosity. Once the temperature reaches 373 K, the water volumetric fraction increases slightly due to the compromise of the vaporized water and the released water from the gypsum dehydration. Then, after the completion of the gypsum dehydration, the variation of water volumetric fraction only reflects the extent of water vaporization. At 473 K, all of the water is vaporized.

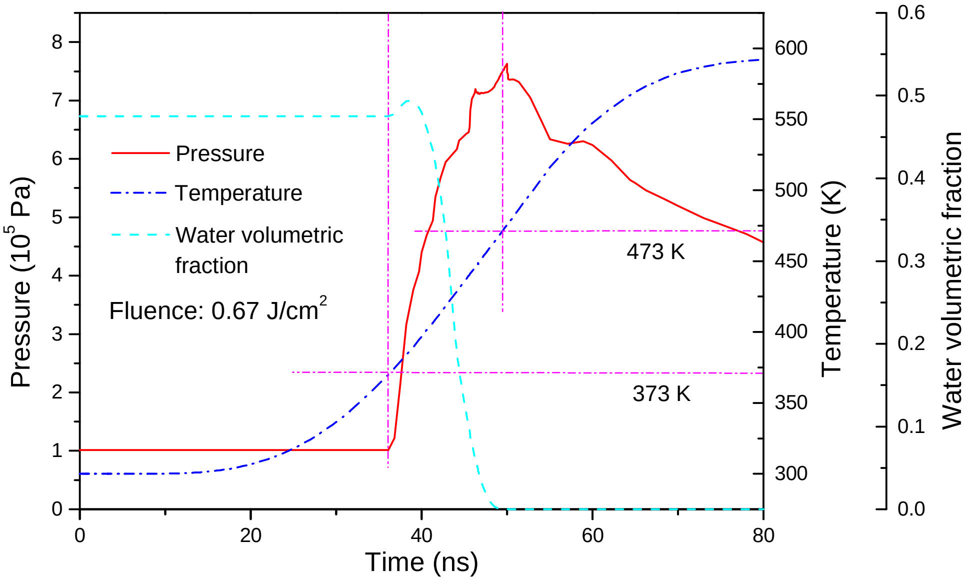

Figure 4.6 Simulated time history of temperature, pressure and water volumetric fraction at the point with the maximal pressure at 50 ns in the encrustation irradiated at 0.67 J/cm^2.

The pressure starts to build-up at 373 K. The peak value of pressure is located at the interface between the dry and wet encrustation with the temperature of 475 K. In addition, the pressure increases with the temperature during laser irradiation. The temperature still increases after the laser irradiation, yet the pressure decreases. In the former case, the increase in pressure is attributed to the vaporization of more and more water. In the latter case, the limited pressure increase resulting from the slow heating cannot compensate the pressure decrease caused by the strong gas movement upwards to the surface.

Figure 4.7 shows the time history of temperature and pressure at two points along the symmetrical axis with the depth of 0.1 and 1 μm, respectively. In **Figure 4.7(a)**, the point at the depth of 0.1 μm (z =119.9 μm) is heated up to 2160 K at approximately 35 ns.

After 35 ns, its temperature fluctuates around 2160 K, which means this point is within the area that is thermally ablated. Concerning the point at the depth of 1 µm (z =119 µm), its temperature increase starts at about 7 ns and continues until 50 ns. After the end of pulse irradiation at 50 ns, its temperature continues to increase due to the heat transferred from the adjacent area of higher temperature, and then decreases. The model described in Ref.4 is adopted to calculate the temperature produced at the same fluence as 0.67 J/cm^2 without the assistance of water. The corresponding temperature history at these two points is also shown in **Figure 4.7(a)**. It is observed that the temperature produced without water is higher than that produced with water, demonstrating water with a high specific heat, cools the encrustation.

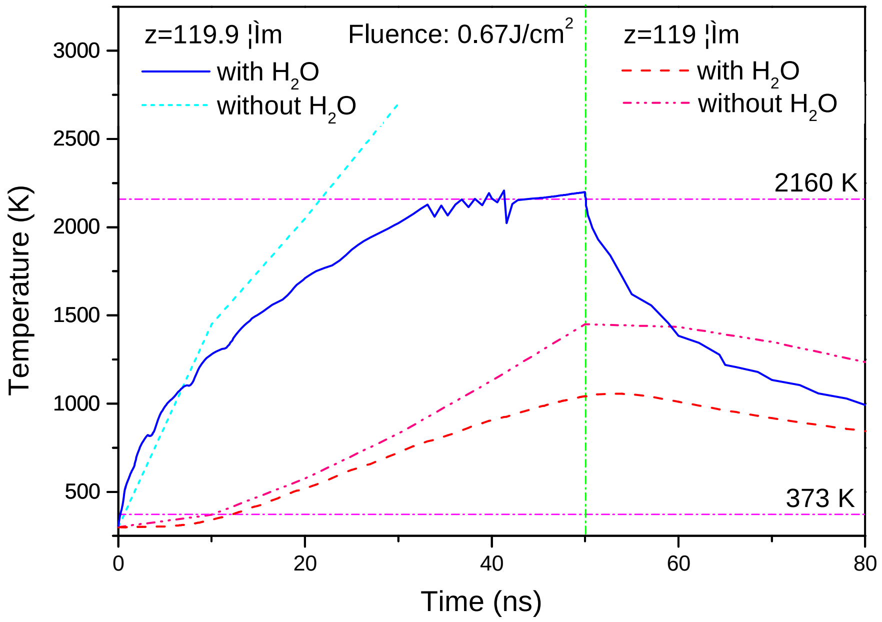

(a)

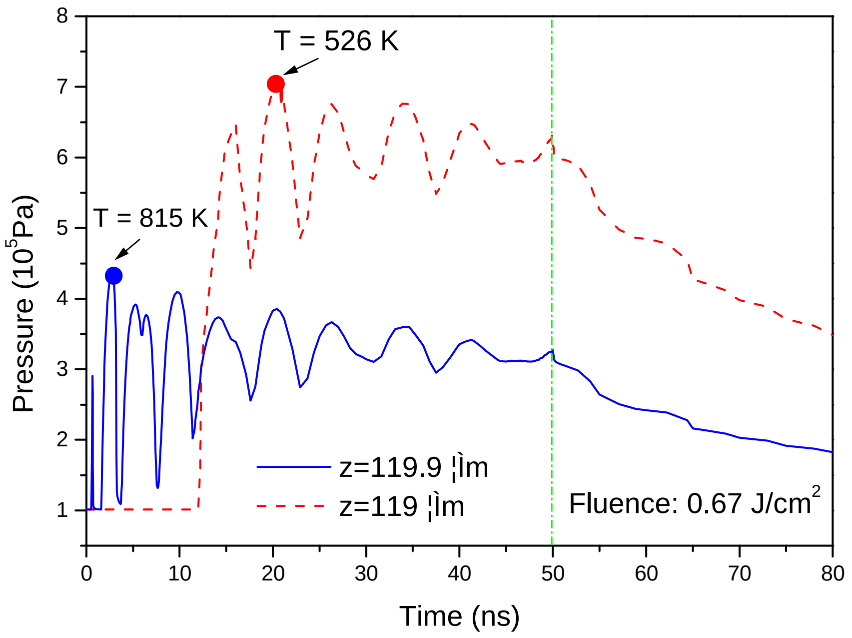

(b)

Figure 4.7 Simulated time history of (a) temperature and (b) pressure of two points at the symmetrical axis produced by the pulse at 0.67 J/cm^2.

In **Figure 4.7(b)**, both pressures at the two points are established at 373 K. The peak pressures of the points at 119 µm and 119.9 µm appear at 526 K and 815 K, respectively. Below 526 K and 815 K, the pressure increases continuously. Above 526 K and 815 K, the pressure gradually decreases.

The history of the velocities at the depth and radial direction of the point at z = 119 µm is presented in **Figure 4.8**. The radial velocity is much smaller than the velocity in the depth direction. It can be reasoned that the convection of water vapor along the depth direction is much more intense due to the enormous pressure gradient along this direction. As vaporization starts, the negative vapor velocity in the depth direction represents the vapor moves downward due to its pressure lower than the pressure of the upper nodes. Then, until 526 K or 815 K, the positive velocity means the vapor moves upward from the liquid surface and is accumulated in the pore. After that, the vapor starts to move out of the pore and towards the irradiated surface, which is verified by the positive velocity and the decreasing pressure.

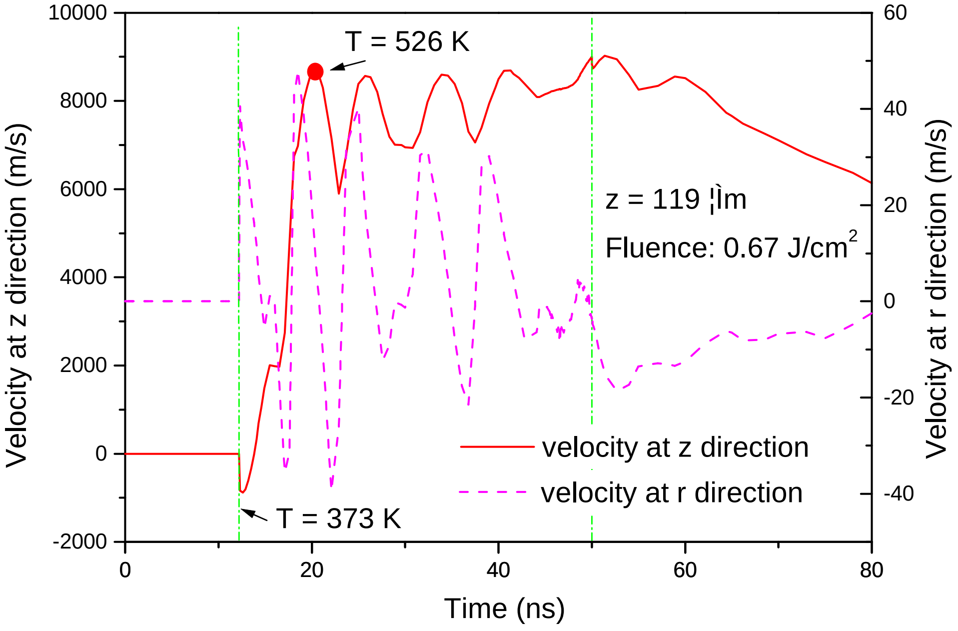

Figure 4.8 Simulated time history of vapor velocity of the point at the symmetrical axis (z = 119 μm) produced by the pulse at 0.67 J/cm^2.

The vapor, which escaped from the deeper pores, enhances the local pressure. On the other hand, the exiting of vapor further reduces the local pressure. Accordingly, the local pressure fluctuates and also leads to fluctuation of the velocity. However, the velocity fluctuates around a constant value. This is because the fluctuating pressure decreases but the pressure gradient remains constant. There is a noticeable fluctuation occurring as the pressure increases, shown in **Figure 4.7(b)**. However, the velocity does not follow this pattern. A possible explanation is that the lower pressure is built-up during the initial water evaporation at a deeper level, and as a result the partial vapor flowing downward causes the pressure to fluctuate.

It can be seen in **Figure 4.7(b)** that the pressure at 119 µm is always higher than that at 119.9 µm. The vapor at the shallow depth escapes easily, and thus the pressure is hard to be built-up. The opposite is true for the deeper points.

4.4.1.3 Calculation of the ablated encrustation weight by one single pulse

The pressure profiles along the symmetrical axis produced at fluences of 0.49, 0.67, 0.95, 1.3, and 1.45 J/cm^2 at 50 ns are shown in **Figure 4.9**. The pressure field extends with fluence. The higher the fluence is applied, the larger the heat-affected zone is generated. Therefore, more water reaches the boiling point, and then the pressure is built-up in a larger region. The induced maximal pressure increases with fluence as well. At high fluence, the water is vaporized much more quickly due to the high heating rate. Thus, the intensified amassment of the vapor promotes an increase in pressure.

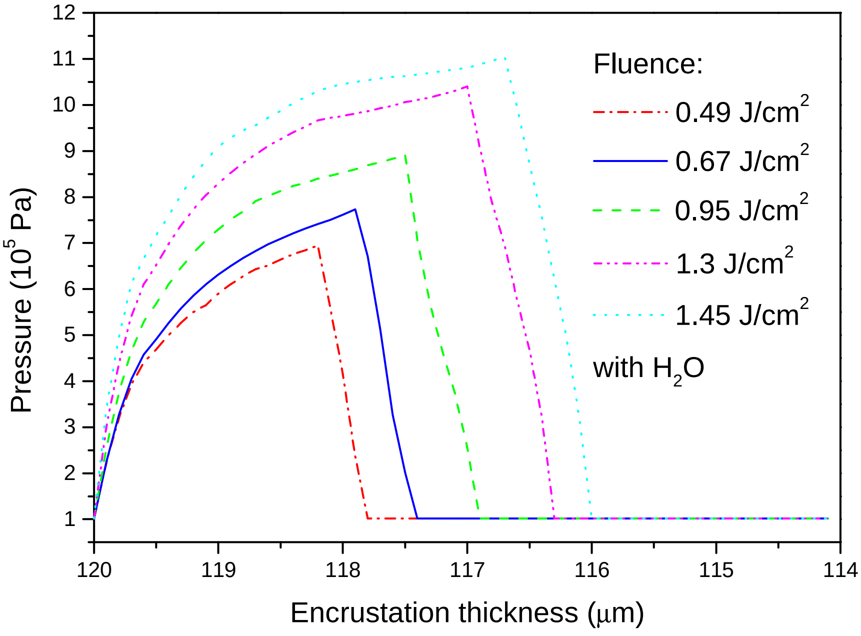

Figure 4.9 Comparison of the pressure profiles along the symmetrical axis at 50 ns produced by the different fluences.

The pressure contours produced at 0.67 J/cm^2 at 10, 30 and 80 ns are shown in **Figure 4.10**. It can be seen that the maximal pressure at 10, 30, 50 and 80 ns are about 6.5, 7.1, 7.7 and 4.9 atm, respectively. The maximal pressure appears at 50 ns during laser wet cleaning. The increase in pressure with heating time results from vapor formed at deeper level being trapped and not being allowed to escape through pores. At 80 ns, the heat transferred from the above hot area still can vaporize the water, yet the generated pressure is relatively low due to the slow heating rate.

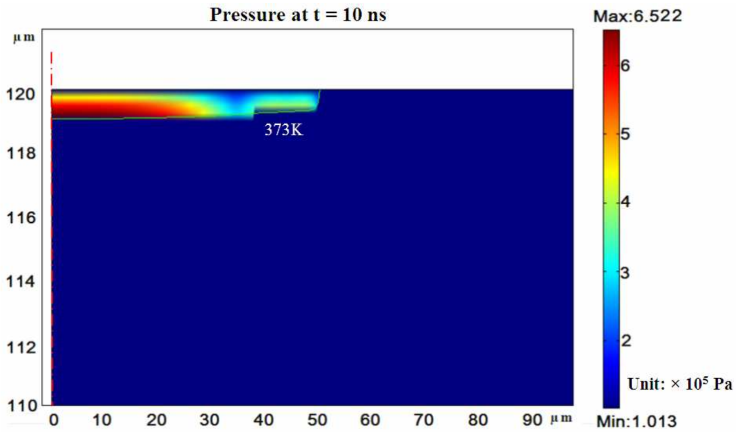
Pressure at t = 10 ns
Max:6.522
μm
120
118
116
114
112
110
0
10
20
30
40
50
60
70
80
90 μm
373K
6
5
4
3
2
Unit: × 10⁵ Pa
Min:1.013

(a)

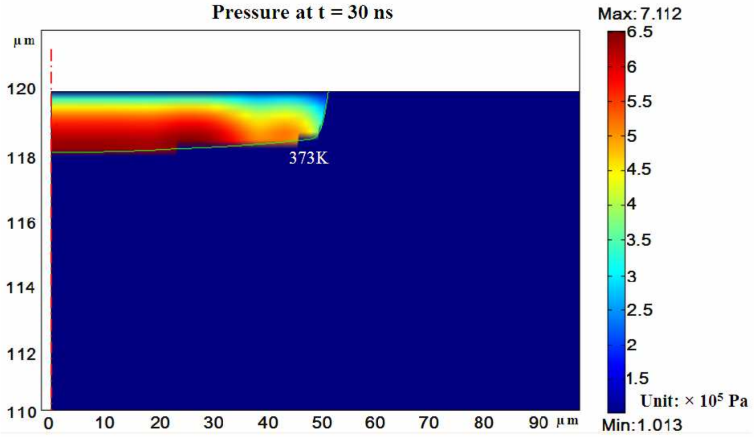
Pressure at t = 30 ns
Max: 7.112
μm
120
118
116
114
112
110
0
10
20
30
40
50
60
70
80
90 μm
373K
6.5
6
5.5
5
4.5
4
3.5
3
2.5
2
1.5
Unit: × 10⁵ Pa
Min:1.013

(b)

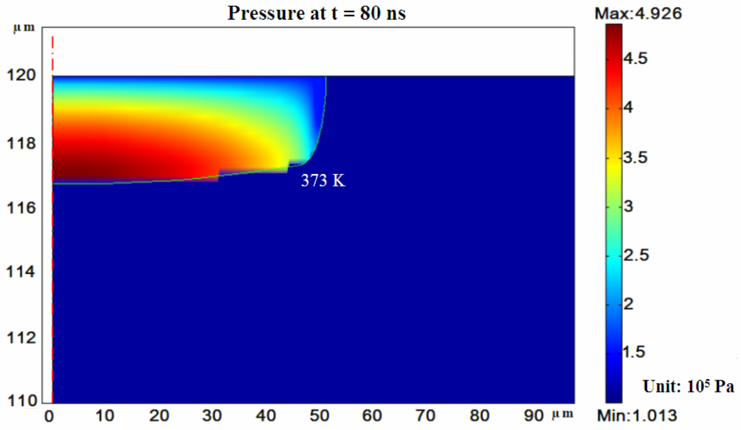
Pressure at t = 80 ns
Max:4.926
μm
120
118
116
114
112
110
0
10
20
30
40
50
60
70
80
90 μm
373 K
4.5
4
3.5
3
2.5
2
1.5
Unit: 10⁵ Pa
Min:1.013

(c)

Figure 4.10 Surface contours of pressure at (a) 10 ns (b) 30 ns (c) 80 ns produced by the pulse at 0.67 J/cm^2 in the partial encrustation (10 µm × 98 µm).

Suppose that once the maximal pressure at 50 ns exceeds the tensile strength, the whole encrustation with the diameter of 100 µm above the point with maximal pressure is completely removed. Accordingly, the ablated encrustation weight per pulse can be predicted. The experimental and simulated ablated encrustation weights by one single pulse are compared in **Figure 4.11**. The simulated values have the same trend as the experimental values. Also, the former is rather close to the latter. Therefore, the proposed model is validated by the experiments to some extent.

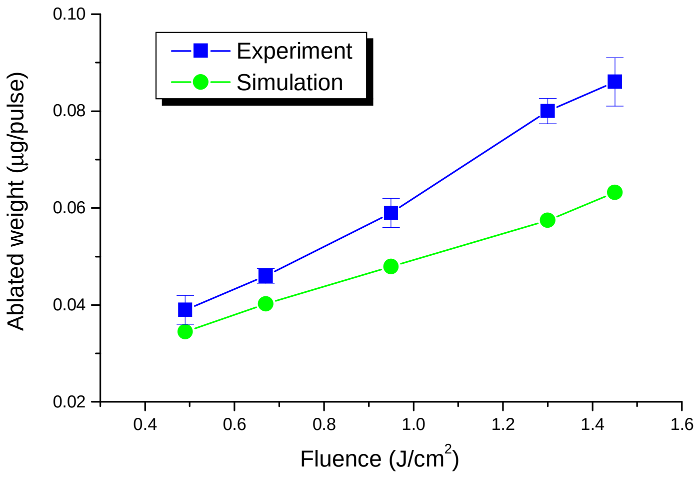

Figure 4.11 Comparison of the experimental and simulated ablated encrustation weight by one single pulse at different fluence levels with distilled water.

The discrepancy between the simulated and experimental ablated weights is due to the shortcoming of the present model. In reality, a thin layer of encrustation may be stripped away at 10 ns due to the high pressure. Then, the laser beam irradiates the newly exposed surface and establishes the pressure again. However, the present model cannot exclude the removed part from the calculation domain. The discrepancy is aggravated with the fluence, which further reflects the inappropriate treatment of the pressure-removed part because the enhanced pressure by the fluence plays a more important role. Future research will improve the model in this aspect.

4.4.2 Effect of other liquids on the cleaning efficiency

Liquids with thermodynamic properties different from that of water have a different effect on the laser cleaning process. Ethanol and acetone are applied to assist the laser ablative cleaning. Both have very similar thermodynamic properties except that the boiling point and vaporization heat of ethanol are higher than that of acetone. However, their boiling point, specific heat, thermal conductivity and vaporization heat are lower than that of water.

To rather accurately determine the cleaning efficiency, the experimental strategy described in section 3.6.1 in chapter 3 is followed. Laser cleaning with ethanol or acetone is performed at fluences of 0.49, 0.67, 0.95, 1.3, and 1.45 J/cm^2, respectively. The ablated encrustation weight by one single pulse with distilled water, ethanol and acetone are compared in **Figure 4.12**. At the same fluence, the ablated weight with acetone is the largest, that with distilled water is the smallest, and that with ethanol is in the middle. Though the ablated weight is enhanced with the fluence in all three cases, the increase in the ablated weight with acetone, ethanol and water are in the order of decreasing value.

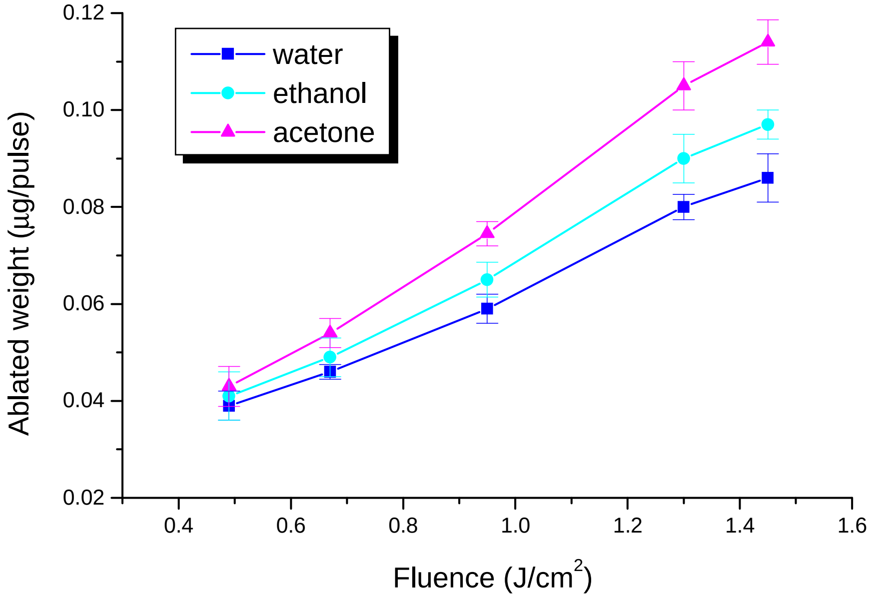

Figure 4.12 Comparison of the ablated encrustation weight by one single pulse at different fluence levels with different liquids.

The likely reasons for the enhanced cleaning efficiency of acetone are now explained. The simulated pressure profiles along the symmetrical axis produced at 0.67 J/cm^2 with distilled water, ethanol or acetone at 50 ns are compared in **Figure 4.13**. Obviously, the vapor pressure is built-up in the deepest and widest area in the case of acetone. Its low thermodynamic properties lead to heat being transferred further and faster. Thus, acetone is vaporized in many more pores. In addition, the peak value of the pressure induced by acetone is largest partially due to the higher heating rate.

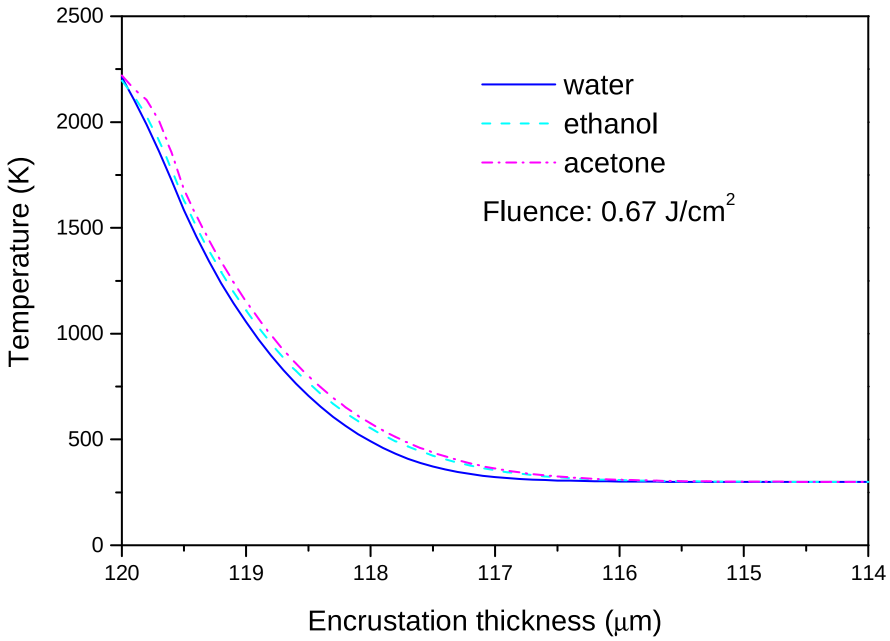

2500
2000
1500
1000
500
0
Temperature (K)
120
119
118
117
116
115
114
Encrustation thickness (μm)
water
ethanol
acetone
Fluence: 0.67 J/cm^2

(a)

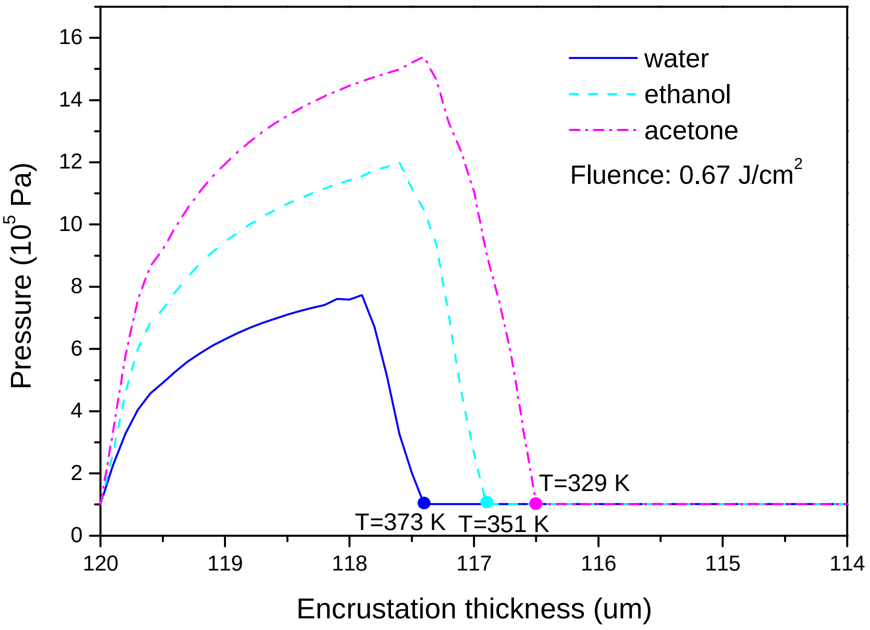

(b)

Figure 4.13 Comparison of (a) temperature and (b) pressure profiles along the symmetrical axis at 50 ns with the pulse at 0.67 J/cm^2 with different liquids.

4.4.3 Effect of liquids on the color of cleaned surface

To measure the surface color of cleaned marble, a circular encrustation with a diameter of 9 mm is removed to fit the 8 mm measurement spot of the chromameter. The method for removing the circular encrustation described in section 3.6.2.1 in chapter 3. Zhang, et al., in 2007 found that the marble surface became slightly yellowed after cleaning with the 355 nm pulse at 0.67 J/cm^2 [4]. For the comparative analysis, a fluence of 0.67 J/cm^2 is applied to clean marble with liquids. The encrustation is completely removed by 8 pulses without liquids, 6 pulses with distilled water, 5 pulses with ethanol and 5 pulses with acetone, respectively. This also reflects the improvement in the cleaning efficiency of wet cleaning.

The color measurements of the original and cleaned marble surface as well as the encrustation are listed in **Table 4.1**. All color data is the average of 5 independent measurements.

Table 4.1 Color measurements

	Original marble	Encrustation	Marble cleaned by 8 pulses at 0.67 J/cm^2	Original marble	Encrustation	Marble cleaned by 6 pulses at 0.67 J/cm^2 with water
ΔL^*	90.8433	59.3900	84.2767	84.9433	59.3900	82.8167
Δa^*	-1.0333	11.2167	-0.2033	-1.1427	11.2167	-0.0282
Δb^*	-0.9400	13.9633	1.8933	-0.7917	13.9633	-0.0690
	Original marble	Encrustation	Marble cleaned by 5 pulses at 0.67 J/cm^2 with ethanol	Original marble	Encrustation	Marble cleaned by 5 pulses at 0.67 J/cm^2 with acetone
ΔL^*	85.1453	56.2100	83.1182	87.0710	56.2100	84.0112
Δa^*	-0.9895	10.5608	-0.0531	-1.1621	10.5608	-0.0451
Δb^*	-1.0920	8.9632	-0.0484	-1.1217	8.9632	-0.0715

ΔL^*: Lightness; Δa^*: Red-Green; Δb^*: Blue-Yellow

Figure 4.14 shows the lightness (ΔL^*) and blue-yellow (Δb^*) coordinates in the 1971 CIE $L^*a^*b^*$ color space. Concerning the encrustation, the lower lightness denotes the black appearance of the encrustation due to the graphite. The positive Δa^* and Δb^* reflects the encrustation color is inclined to the redness and yellowness due to the dark-brown hematite in the encrustation.

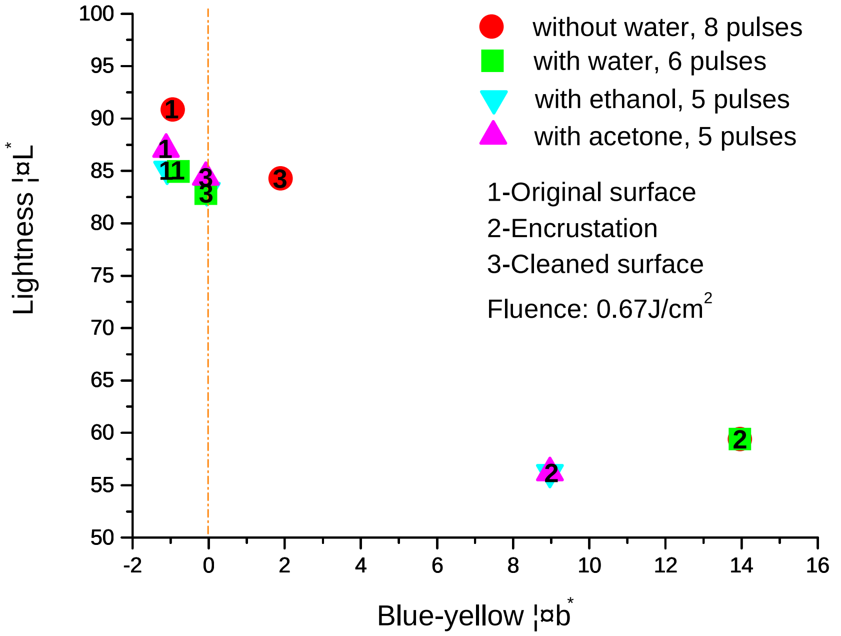

Figure 4.14 The variation of two color coordinates of marble surface cleaned at 0.67J/cm^2 without or with different liquids.

Four cleaned marble surfaces are very close to the original ones in the lightness, which implies the removal of the encrustation. The lightness difference between a marble surface cleaned with liquids and the original surfaces is less than that between surface cleaned without liquids and its original surface. This means the encrustation may be completely removed in the former case. Without liquids, Δa^* of the cleaned surface is close to the original value and has the same sign. Yet, Δb^* of the cleaned surface is positive, which indicates the surface becomes slightly yellowed. With liquids, both Δa^* and Δb^* of the cleaned surfaces are close to the original values and have the same sign. It can be concluded that there is no discoloration on the surfaces cleaned at low fluence with liquids.

The Raman spectra obtained on four cleaned surfaces at 514 nm are presented in **Figure 4.15**. All sample preparation and the set-up of the Raman instrument are same as that in the chapter 3. The spectrum of the surface cleaned without liquids consists of bands of $CaCO_3$ at 158, 285, 711, 1084 cm^{-1} [21] and bands of Fe_2O_3 at 224 and 405 cm^{-1} [22]. Yet, the spectra of the surface cleaned with liquids only have the bands of $CaCO_3$. The $CaCO_3$ bands in four spectra indicate the marble surfaces are exposed after the removal of the encrustation. The Fe_2O_3 bands reflect Fe_2O_3 still resides on the surface cleaned without liquids, and is responsible for the slightly yellowed surface.

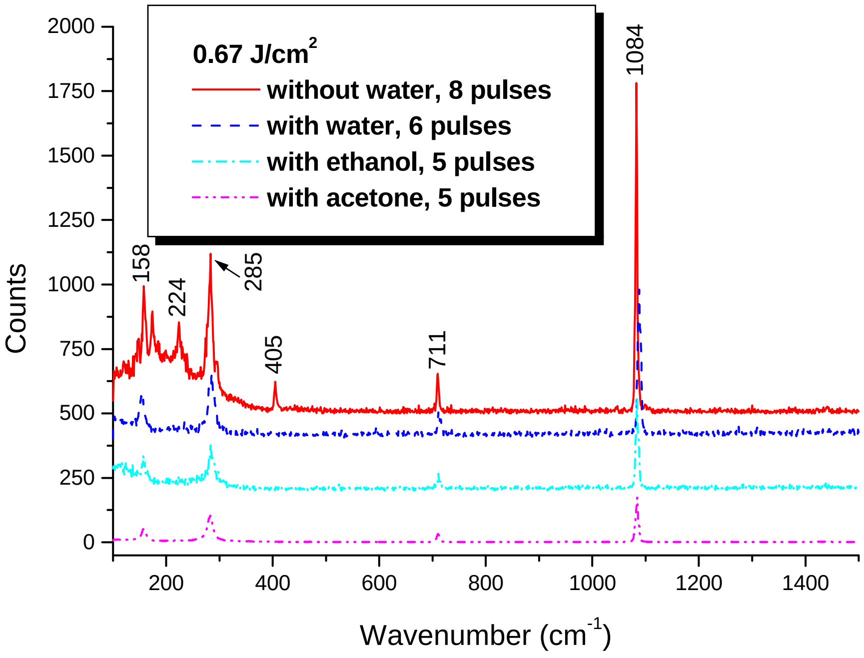

Figure 4.15 Raman spectra collected from marble surface cleaned at 0.67J/cm^2 without or with different liquids (Raman shifts are activated by the 514 nm cw laser at a power of 20 mW, the red, blue and cyan lines have an upward shift of 500, 400 and 200 for the clarity, respectively).

In laser wet cleaning, since liquids consume the laser heat absorbed by the encrustation to raise the temperature and vaporize, the entire temperature field is decreased in the irradiated encrustation. This inhibits the reduction of hematite by the graphite. In addition, the majority of the encrustation is stripped away by the vapor pressure. The maximal vapor pressure takes place at the interface between the dry and wet encrustation, which is much lower than the ablation front in the encrustation. The stripping of the encrustation by the vapor pressure starts very near the interface. Even if some hematite is reduced to iron, the iron can be taken away by the stripped encrustation. Thus, there is no the possibility for the iron is left on the marble surface and then is oxidized by air after the laser irradiation.

4.5 Conclusions

The enhanced cleaning efficiency of laser wet cleaning, in the case of the stone encrustation, is due to the generation of vapor pressure. The liquid in the encrustation pores is vaporized, and the accumulated vapor induces a build-up of pressure. Once the pore pressure exceeds the tensile strength of the encrustation, the encrustation is stripped away. The established model describing coupled heat transfer and mass transport in the porous structure can simulate the distribution of temperature, vapor pressure and liquid volumetric fraction in the encrustation produced by the laser irradiation. The model-predicted ablated encrustation weight by one single pulse agrees with the experimental values to some extent. The difference in the cleaning efficiency between laser wet and dry cleaning increases with the incident fluence. The use of liquids with low boiling points and specific heats in laser wet cleaning is more beneficial to boost the cleaning efficiency. With the assistance of liquids, no discoloration occurs on the surface cleaned by the 355 nm pulse with the low fluence. The iron from the reduction of hematite by graphite is taken away by the pressure-induced removal of the encrustation.

References

Chapter 1

1. Huynh, W. U.; Peng, X. G.; Alivisatos, A. P. *Adv. Mater.* **1999**, *11*, 923–927.

2. Hikmet, R. A. M.; Talapin, D. V.; Weller, H. *J. Appl. Phys.* **2003**, *93*, 3509–3514.

3. Han, M. Y.; Gao, X. H.; Su, J. Z.; Nie, S. *Nat. Biotechnol.* **2001**, *19*, 631–635.

4. Sandros, M. G.; Shete, V.; Benson, D. E. *Analyst* **2006**, *131*, 229–235.

5. Peng, X. G.; Schlamp, M. C.; Kadavanich, A. V.; Alivisatos, A. P. *J. Am. Chem. Soc.* **1997**, *119*, 7019–7029.

6. Hines, M. A.; Guyot-Sionnest, P. *J. Phys. Chem.* **1996**, *100*, 468–471.

7. Huynh, W. U.; Dittmer, J. J.; Alivisatos, A. P. *Science* **2002**, *295*, 2425–2427.

8. Ivanov, S. A.; Nanda, J.; Piryatinski, A.; Achermann, M.; Balet, L. P.; Bezel, I. V.; Anikeeva, P. O.; Tretiak, S.; Klimov, V. I. *J. Phys.Chem. B* **2004**, *108*, 10625–10630.

9. Zegrya, G. G.; Andreev, A. D. *Appl. Phys. Lett.* **1995**, *67*, 2681–2683.

10. Ivanov, S. A.; Piryatinski, A.; Nanda, J.; Tretiak, S.; Zavadil, K. R.; Wallace, W. O.; Werder, D.; Klimov, V. I. *J. Am. Chem. Soc.* **2007**, *129*, 11708–11719.

11. Oron, D.; Kazes, M.; Banin, U. *Phys. Rev. B* **2007**, *75*, 035330.

12. Klimov, V. I.; Schwarz, C. J.; McBranch, D. W.; Leatherdale, C. A.; Bawendi, M. G. *Phys. Rev. B* **1999**, *60*, R2177–R2180.

13. Klimov, V. I.; Mikhailovsky, A. A.; Xu, S.; Malko, A.; Hollingsworth, J. A.; Leatherdale, C. A.; Eisler, H. J.; Bawendi, M. G. *Science* **2000**, *287*, 1011–1013.

14. Chen, C. Y.; Cheng, C. T.; Lai, C. W.; Hu, Y. H.; Chou, P. T.; Chou, Y. H.; Chiu, H. T. *Small* **2005**, *1*, 1215–1220.

15. Cheng, C. T.; Chen, C. Y.; Lai, C. W.; Liu, W. H.; Pu, S. C.; Chou, P. T.; Chou, Y. H.; Chiu, H. T. *J. Mater. Chem.* **2005**, *15*, 3409–3414.

16. Xie, R. G.; Zhong, X. H.; Basche, T. *Adv. Mater.* **2005**, *17*, 2741–2744.

17. Kim, S.; Fisher, B.; Eisler, H. J.; Bawendi, M. G. *J. Am. Chem.Soc.* **2003**, *125*, 11466–11467.

18. Klimov, V. I.; Ivanov, S. A.; Nanda, J.; Achermann, M.; Bezel, I.; McGuire, J. A.; Piryatinski, A. *Nature* **2007**, *447*, 441–446.

19. Balet, L. P.; Ivanov, S. A.; Piryatinski, A.; Achermann, M.; Klimov, V. I. *Nano Lett.* **2004**, *4*, 1485–1488.

20. Shim, M.; Guyot-Sionnest, P. *J. Am. Chem. Soc.* **2001**, *123*, 11651–11654.

21. Ouyang, J. Y.; Ratcliffe, C. I.; Kingston, D.; Wilkinson, B.; Kuijper, J.; Wu, X. H.; Ripmeester, J. A.; Yu, K. *J. Phys. Chem. C* **2008**, *112*, 4908–4919.

22. Weinhardt, L.; Heske, C.; Umbach, E.; Niesen, T. P.; Visbeck, S.; Karg, F. *Appl. Phys. Lett.* **2004**, *84*, 3175–3177.

23. Son, D. H.; Hughes, S. M.; Yin, Y. D.; Alivisatos, A. P. *Science* **2004**, *306*, 1009–1012.

24. Wong, E. M.; Searson, P. C. *Appl. Phys. Lett.* **1999**, *74*, 2939–2941.

25. Rorison, J. M. *Phys. Rev. B* **1993**, *48*, 4643–4649.

26. Felix, C. L.; Bewley, W. W.; Vurgaftman, I.; Meyer, J. R.; Zhang, D.; Lin, C. H.; Yang, R. Q.; Pei, S. S. *IEEE Photon Technol. Lett.* **1997**, *9*, 1433–1435.

27. Sajinovic, D.; Saponjic, Z. V.; Cvjeticanin, N.; Marinovic-Cincovic, M.; Nedeljkovic, J. M. *Chem. Phys. Lett.***2000**, *329*, 168–172.

Chapter 2

1. Harborne, J. B. *The Flavonoides: Advances in Research since 1986*; Chapman and Hall: London, **1994**.

2. Harborne, J. B.; Mabry, T. J.; Mabry, H. *The Flavonoids*; Chapman and Hall: London, **1975**.

3. Harborne, J. B.; Mabry, T. J. *The Flavonoids: Advances in Research*; Chapman and Hall: London, **1982**.

4. McClure, J. W. In *Plant Flavonoids in biology and Medicine: Biochemical, Pharmacological and Structure-Activity Relationships*; Cody, V.; Middleton, E.; Harborne, J. B., Eds.; Alan R. Liss: New York, **1986**; pp 77-85.

5. Geissman, T. A. *The Chemistry of Flavonoid Compounds*; The Macmillan Company: New York, **1962**

6. Smith, D. A.; Banks, S. W. In *Plant Flavonoids in Biology and Medicine: Biochemical, Pharmacological and Structure-Activity Relationships*; Cody, V.; Middleton, E.; Harborne, J. B., Eds.; Alan R. Liss: New York, **1986**; pp 1, 13-24.

7. Gabor, M. *The Pharmacology of Benzopyrone Derivatives and Related Compounds*; Akademiai Kiado: Budapest, **1986**.

8. Dean, F. M. *Naturally Occurring Oxygen Ring Compounds*; Butterworts: London, **1963**; p 280.

9. Mabry, T. J.; Markham, F. K.; Thomas, M. B. *The Systematic Identification of Flavonoids*; Springer: Berlin, **1970**.

10. Sengupta, P. K.; Kasha, M. *Chem. Phys. Lett.* **1979**, *68*, 382.

11. Itoh, M.; Fujiwara, Y.; Sumitani, M.; Yoshihara, K. *J. Phys. Chem.***1986**, *90*, 5672.

12. Brewer, W. E.; Studer, S. L.; Standiford, M.; Chou, P. T. *J. Phys. Chem.* **1989**, *93*, 6088.

13. Dzugan, T. P.; Schmidt, J.; Aartsma, T. J. *Chem. Phys. Lett.* **1986**, *127(4)*, 336.

14. Looker, J. H.; Hanneman, W. W. *J. Org. Chem.* **1962**, *27*, 381.

15. Jose, C. I.; Phadke, P. S.; Rao, A. V. R. *Spectrochem. Acta* **1974**, *30A*, 1199.

16. Shaw, L.; Simpson, T. H. *J. Chem. Soc.* **1955**, 655.

17. Hergert, H. L.; Kurth, E. F. *J. Amer. Chem. Soc.* **1953**, *75*, 1622.

18. Looker, J. H.; Hanneman, W. W.; Kagal, S. A.; Dappen, J. I.; Edman, J. R. *J. Hetero-Cyclic Chem.* **1966**, *3*, 55.

19. Looker, J. H.; Kagal, S. A.; Dappen, J. I.; Edman, J. R. *J. Hetero-Cyclic Chem.* **1966**, *3*, 61.

20. Petroski, J. M.; DeSaValente, C.; Kelson, E. P.; Collins, S. *J. Phys. Chem. A* **2002**, *106*, 11714-11718.

21. *SERS as sensing method for bio-molecules on MBE-grown quantum dots*; Livingstone, R. L. G.; Quagliano, L. G.; Perez-Paz, N.; Munoz, M.; Tamargo, M. C.; Jean-Mary, F.; Lombardi, J. R. *Proc. SPIE: Nanosensing:Materials and Devices II*; Saif Islam, M., Dutta, A. K. Eds.; 6008-0.A, **2005**.

22. Review Papers, *14th International Forensic Science Symposium*; Daeid, N. N., Ed.; Interpol-Lyon, 19-22. October **2004**.

23. Rodger, C.; Dent, G.; Watkinson, J.; Smith, W. E. *Appl. Spectrosc.***2000**, *54 (11)*, 1567-1576.

24. Chen, K.; Leona, M.; Vo-Dinh, K. C.; Yan, F; Wabuyele, M. B.; Vo-Dinh, T. Application of surface-enhanced Raman scattering (SERS) for the identification of anthraquinone dyes used in works of art. *J. Raman Spectrosc*. **2006**, *37*, 520-527.

25. Wang, M.; Spataru, Tudor; Lombardi, J. R.; Birke, R. L. *J. Phys. Chem. C* **2007**, *111*, 3044-3052.

26. Birke, R. L.; Lu, T.; Lombardi, J. R. In *Techniques for characterization of Electrodes and Electrochemical Processes*; Varma, R., Selam, J. R., Eds.; John Wiley & Sons, Inc.: New York, **1991**; Chapter 5.

27. Lee, P. C.; Meisel, D. *J. Phys. Chem.* **1982**, *86*, 3391-3395.

28. Frisch, M. J.; Trucks, G. W.; Schlegel, H. B.; Scuseria, G. E.; Robb, M. A.; Cheeseman, J. R.; Montgomery, J. A., Jr.; Vreven, T.; Kudin, K. N.; Burant, J. C.; Millam, J. M.; Iyengar, S. S.; Tomasi, J.; Barone, V.; Mennucci, B.; Cossi, M.; Scalmani, G.; Rega, N.; Petersson, G. A.; Nakatsuji, H.; Hada, M.; Ehara, M.; Toyota, K.; Fukuda, R.; Hasegawa, J.; Ishida, M.; Nakajima, T.; Honda, Y.; Kitao, O.; Nakai, H.; Klene, M.; Li, X.; Knox, J. E.; Hratchian, H. P.; Cross, J. B.; Bakken, V.; Adamo, C.; Jaramillo, J.; Gomperts, R.; Stratmann, R. E.; Yazyev, O.; Austin, A. J.; Cammi, R.; Pomelli, C.; Ochterski, J. W.; Ayala, P. Y.; Morokuma, K.; Voth, G. A.; Salvador, P.; Dannenberg, J. J.; Zakrzewski, V. G.; Dapprich, S.; Daniels, A. D.; Strain, M. C.; Farkas, O.; Malick, D. K.; Rabuck, A. D.; Raghavachari, K.; Foresman, J. B.; Ortiz, J. V.; Cui, Q.; Baboul, A. G.; Clifford, S.; Cioslowski, J.; Stefanov, B. B.; Liu, G.; Liashenko, A.; Piskorz, P.; Komaromi, I.; Martin, R. L.; Fox, D. J.; Keith, T.; Al-Laham, M. A.; Peng, C. Y.; Nanayakkara, A.; Challacombe, M.; Gill, P. M. W.;

Johnson, B.; Chen, W.; Wong, M. W.; Gonzalez, C.; Pople, J. A. *Gaussian 03*, revision C.02; Gaussian, Inc.: Wallingford, CT, **2004**.

29. Apra, E.; Windus, T. L.; Straatsma, T. P.; Bylaska, E. J.; de Jong, W.; Hirata, S.; Valiev, M.; Hackler, M.; Pollack, L.; Kowalski, K.; Harrison, R.; Dupuis, M.; Smith, D. M. A; Nieplocha, J.; Tipparaju, V.; Krishnan, M.; Auer, A. A.; Brown, E.; Cisneros, G.; Fann, G.; Fruchtl, H.; Garza, J.; Hirao, K.; Kendall, R.; Nichols, J.; Tsemekhman, K.; Wolinski, K.; Anchell, J.; Bernholdt, D.; Borowski, P.; Clark, T.; Clerc, D.; Dachsel, H.; Deegan, M.; Dyall, K.; Elwood, D.; Glendening, E.; Gutowski, M.; Hess, A.; Jaffe, J.; Johnson, B.; Ju, J.; Kobayashi, R.; Kutteh, R.; Lin, Z.; Littlefield, R.; Long, X.; Meng, B.; Nakajima, T.; Niu, S.; Rosing, M.; Sandrone, G.; Stave, M.; Taylor, H.; Thomas, G.; van Lenthe, J.; Wong, A.; Zhang, Z. *NWChem, A Computational Chemistry Package for Parallel Computers*, version 4.7; Pacific Northwest National Laboratory: Richland, WA, **2005**.
30. Zhao, L.; Jensen, L.; Schatz, G. C. *J. Am. Chem. Soc.* **2006**, *128*, 2911-2919.
31. *Introduction to Modern Vibrational Spectroscopy*; Diem, M.; Wiley and Sons: New York, **1993**. Lin-Vien, D.; Colthup, N. B.; Fateley, W. G.; Grasselli, J. G. *The Handbook of Infrared and Raman Characteristic Frequencies of Organic Molecules*; Academic Press, Inc.: New York, **1991**.
32. Jurasekova, Z.; Garcia-Ramos, J. V.; Domingo, C.; Sanchez-Cortez *J. Raman Spectrosc.* **2006**, DOI:10.1002/jrs.1643.

Chapter 3

1. Skoulikidis, T.; Charalambous, D. *Br. Corro. J.* **1981,** *16,* 49.
2. Griffin, P.S.; Indictor, N.; Koestler, R.J. *Int. Biodeterior.* **1991,** *28,* 187.
3. Cooper, M. *Laser Cleaning in Conservation: An Introduction*, Butterworth-Heinemann, **1998**.
4. Tam, A.C.; Leung, W.P.; Zapka, W.; Ziemlih, W. *J. Appl. Phys.* **1992,** *71 (7),* 3515.
5. Zhang, J.; Wang, Y.W.; Cheng, P.; Yao, Y.L. *J. Appl. Phys.* **2006,** *99 (6),* 064902
6. Asmus, J.F.; Munk, W.; Murphy, C. *Proc. Soc. Photo-Optical Instrum.* **1974,** *41,* 19.
7. Laboure, M.; Bromblet, P.; Orial, G.; Wiedemann, G.; Simon-Boisson, C. *J. Cult. Herit.* **2000,** *1,* s21.
8. Siano, S.; Margheri, F.; Pini, R.; Mazzinghi, P.; Salimbeni, R. *Appl. Opt.* **1997,** *36 (27),* 7073.
9. Siano, S.; Fabiani, F.; Pini, R.; Salimbeni, R.; Giamello, M.; Sabatini, G. *J. Cult. Herit.* **2000,** *1,* s47.
10. Maravelaki, P.; Zafiropulos, V.; Kilikoglou, V.; Kalaitzaki, M.; Fotakis, C. *Spectrochim. ACTA Part B* **1997,** *52,* 41.
11. Rodriguez-Navarro, C.; Rodriguez-Navarro, A.; Elert, K.; Sebastian, E. *J. Appl. Phy.* **2004**, *95(7),* 3350.
12. Maravelaki-Kalaitzaki, P.; Zafiropulos, V.; Fotakis, C. *Appl. Surf. Sci.* **1999,** *148,* 92.
13. Marakis, G.; Pouli, P.; Zafiropulos, V.; Maravelaki-Kalaitzaki, P. *J. Cult. Herit.* **2003,** *4,* 83s.
14. Klein, S.; Fekrsanati, F.; Hildenhagen, J.; Dickmann, K.; Uphoff, H.; Marakis, Y.; Zafiropulos, V. *Appl. Surf. Sci.* **2001,** *171,* 242.

15. Potgieter-Vermaak, S.; Godoi, R.; Grieken, R.; Potgieter, J.; Oujja, M.; Castillejo, M. *Spectrochim. ACTA Part A* **2005,** *61,* 2460.
16. Zafiropulos, V.; Balas, C.; Manousaki, A.; Marakis, Y.; Maravelaki-Kalaitzaki, P.; Melesanaki, K. ; Pouli, P.; Stratoudaki, T.; Klein, S. ; Hildenhagen, J.; Dickmann, K.; Luk'Yanchuk, B.; Mujat, C.; Dogariu, A. *J. Cult. Herit.* **2003,** *4,* 249s.
17. Mehaffey, J.R.; Cuerrier, P.; Carisse, G. *Fire and Materials* **1994,** *18,* 297.
18. Fuertes, A.; Fernandez, M. *Trans IchemE* **1995,** *73(Part A),* 854.
19. Lipinski, W.; Steinfeld, A. *Int. J. Heat Mass Trans.* **2004,** *47,* 1907.
20. Jagtap, S.B.; Pande, A.R.; Gokarn, A.N. *J. Chem. Eng. Japan* **1991,** *25(1),* 6.
21. Sato, A.; Aragane, G.; Kamihara, K.; Yoshimatsu, S. *Tetsu-to-Hagane* **1987,** *73,* 812.
22. Lee, J.; Min, D.; Kim, S. *Metallurg. Mater. Trans. B* **1997,** *28B,* 1019.
23. Fatu, D. *J. Therm. Anal. Calor.* **2001,** *65,* 213.
24. Sugawara, K.; Morimoto, K.; Sugawara, T. *AIChE J.* **1999,** *45(3),* 574.
25. Lide, D.R. *CRC Handbook of Chemistry and Physics,* CRC Press, Boca Raton, FL, **2004**.
26. Berns, R. *Billmeyer and Saltzman's Principles of Color Technology,* John Wiley & Sons Inc., New York, **2000**.
27. Birke, R.L.; Lu, T.H.; Lombardi, J.R. in: R. Varma and J.R. Selman (Ed.), *Techniques for Characterization of Electrodes and Electrochemical Processes,* John Wiley & Sons, N.Y., **1991**, p211.
28. Prencipe, M.; Pascale, F.; Zicovich-Wilson, C.; Saunders, V.; Orlando, R.; Dovesi, R. *Phys. Chem. Minerals* **2004,** *31,* 559.
29. Faria, D.; Silva, S.; Oliveira, M. *J. of Raman Spectroscopy* **1997,** *28,* 873.

30. Barro′n, V.; Torrent, J. *J. Soil Sci.* **1986,** *37,* 499.
31. Pereira, A.; Delaporte, P.; Sentis, M.; Cros, A.; Marine, W.; Basillais, A.; Thomann, A.; Leborgne, C.; Semmar, N.; Andreazza, P.; Sauvage, T. *Thin Solid Films* **2004,** *453-454,* 16.
32. Schaaf, P.; Han, M.; Lieb, K.; Carpene, E. *Appl. Phys. Lett.* **2002,** *80(6),* 1091.
33. Pereira, A.; Cros, A.; Delaporte, P.; Marine, W.; Sentis, M. *Appl. Surf. Sci.* **2002,** *197-198,* 845.
34. Khanna, A.S. *Introduction to High Temperature Oxidation and Corrosion*, ASM International, Materials Park, **2002**.
35. Zhang, W.W.; Yao, Y.L.; Chen, K. *Int. J. Adv. Manuf. Technol.* **2001,** *18,* 323.

Chapter 4

1. Asmus, J. F.; Munk, W.; and Murphy C., “Studies on the Interaction of Laser Radiation with Art Artifacts,” *Proceedings of the Society of Photo-Optical Instrumentation Engineers*, **1974**, *v 4*, 19-27.
2. Siano, S.; Fabiani, F.; Pini, R.; Salimbeni, R.; Giamello, M.; and Sabatini, G. “Determination of Damage Thresholds to Prevent Side Effects in Laser Cleaning of Pliocene Sandstone of Siena,” *J. Cult. Heritage*, **2000a**, *1*, s47-s53.
3. Klein, S.; Fekrsanati, F.; Hildenhagen, J; Dickmann, K.; Uphoff, H.; Marakis, Y.; and Zafiropulos, V., “Discoloration of Marble during Laser Cleaning by Nd:YAG Laser Wavelengths,” *Appl. Surf. Sci.,* **2001**, *171,* 242-251.

4. Zhang, J.; Birnbaum, A. J.; Yao, Y. L.; Xu, F.; and Lombardi, J. R., “Effect of Fluence on the Discoloration of Marble Cleaned with UV Lasers,” *Appl. Surf. Sci.,* **2007**, *253(6),* 3083-3092.
5. Kim, D.; and Lee, J., “On the Physical Mechanism of Liquid-assisted Laser Cleaning,” *J. Appl. Phys.*, **2004**, *93, n1*, 762-764.
6. Lu, Y. F.; Song, W. D.; Zhang, Y.; and Low, T. S., “Theoretical Model and Experimental Study for Dry and Steam Laser Cleaning,” *Proc. of SPIE,* **1998**, *3550,* 7-18.
7. Laboure, M.; Bromblet, P.; Orial, G.; Wiedemann, G.; Simon-Boisson, C., “Assessment of Laser Cleaning Rate On Limestones and Sandstones,” *J. Cult. Heritage,* **2000**, *1,* s21-s27.
8. Siano, S.; Fabiani, F.; Caruso, D.; Pini, R.; and Salimbeni, R., “Laser Cleaning of Stones: Assessment of Operative Parameters, Damage Thresholds and Associated Optical Diagnostics,” *Proc. of SPIE*, **2000b**, *4070*, 27-35.
9. Cooper, M.; Emmony, D.; and Larson, J., “Characterization of Laser Cleaning of Limestone,” *Optics & Laser Tech.,* **1995**, *27,* 69-73.
10. Thomas, G.; “Thermal Properties of Gypsum Plasterboard at High Temperature,” *Fire and Materials*, **2002**, *26*, 37-45.
11. Whitaker, S.; “Simultaneous Heat, Mass and Momentum Transfer in Porous Media: A Theory of Drying,” *Advances in Heat Transfer,* **1977**, *13,* 119-200.
12. Ahmed, G.; and Hurst, J., “Coupled Heat and Mass Transport Phenomena in Siliceous Aggregate Concrete Slabs Subjected to Fire,” *Fire and Materials*, **1997**, *21*, 161-168.

13. Civan, F.; and Sliepcevich, C. M., “Limitation in the Apparent Heat Capacity Formulation for Heat Transfer with Phase Changes,” *Proc. Okla. Acad. Sci.*, **1987**, *67*, 83-88.
14. Wei, C. K., Davis, H. T., Davis, E. A., and Gordon, J., “Heat and Mass Transfer in Water-Laden Sandstone: Convective Heating,” *AIChE Journal*, **1985**, *31, No. 8*, 1338-1348.
15. Bazant, Z. P.; ASCE, F.; and Zi, G., “Decontamination of Radionuclides from Concrete by Microwave Heating. I: Theory,” *J. of Eng. Mechanics*, **2003**, 777-784.
16. Ang, C. N.; Wang, Y. C., “The Effect of Water Movement on Specific Heat of Gypsum Plasterboard in Heat Transfer Analysis under Natural Fire Exposure,” *Construction and Building Materials*, **2004**, *18*, 505-515.
17. Li, L. Y.; Purkiss, J. A.; Tenchev, R. T., “An Engineering Model for Coupled Heat and Mass Transfer Analysis in Heated Concrete,” *J. Mech. Engi. Sci.*, **2002**, *26*, 213-224.
18. Edmondson, P. T.; Grammatika, M.; Fryer, P. J.; Handy, B., “Modelling of Heat Transfer, Mass Transfer and Flavor Development in Chocolate Crumb,” *7th World Congress of Chemical Engineering*, **2005**, *83(2)*, 89-98.
19. Reid, R.; Prausnitz, J. M.; Poling, B. E., *The Properties of Gases & Liquids*, McGraw-Hill Book Company, New York, **1987**.
20. Hearst, J. R.; Nelson, P. H., *Well Logging for Physical Properties*, McGraw-Hill, New York, **1985**.
21. Prencipe, M.; Pascale, F.; Zicovich-Wilson, C.; Saunders, V.; Orlando, R.; Dovesi, R., “The Vibrational Spectrum of Calcite (CaCO3): an ab Initio Quantum-mechanical

Calculation," *Phys. Chem. Minerals*, **2004**, *31*, 559–564.

22. Faria, D.; Silva, S.; Oliveira, M., "Raman Microspectroscopy of Some Iron Oxides and Oxyhydroxides," *J. of Raman Spectroscopy,* **1997**, *28,* 873-878.